TIP-ENHANCED RAMAN SPECTROSCOPY *in* GRAPHENE

Cassiano Rabelo

December, 2019

Doctoral thesis submitted to the
Graduate Program in Electrical Engineering

of the

Federal University of Minas Gerais
in partial fulfillment of the requirements
for the degree of Doctor in Electrical Engineering.

Advisor:
Prof. Dr. Ado Jorio de Vasconcelos

Co-advisor:
Prof. Dr. Luiz Gustavo O. L. Cançado

"What I want to talk about is the problem of manipulating and controlling things on a small scale"

— Richard Feynman

Abstract

This work addresses fundamental aspects regarding the use of micro and nano optical spectroscopy for the characterization of materials, specially graphene, with potential implications to other two-dimensional nanostructures. It can be said that the difference between micro and nano characterization stems from a limitation intrinsic to optical imaging and spectroscopy systems, for which light cannot be focused in a region smaller than approximately half of its wavelength, where diffraction becomes a limiting factor to spatial resolution.

In order to adapt optical spectroscopy to nanoscience, we use a characterization technique where through the use of an optical nanoantenna, chemical and structural characterization and material manipulation can be achieved at nanoscale. Known as Tip-enhanced Raman spectroscopy (TERS), this technique combines confocal Raman spectroscopy, a diffraction limited technique, with a scanning probe microscope (SPM). In this joint configuration, where an optical nanoantenna is coupled to an inverted microscope, the system is capable of acquiring images and spectral information from nanostructures smaller then the diffraction limit of visible light.

Under development at UFMG's Laboratory of Nanospectroscopy — LabNS — since 2007, this equipment has undergone substantial improvement during this work in order to increase its precision, repeatability, stability and usability, having been successfully used for microscopic and nanoscopic characterization of several distinct graphene materials, which include mechanically exfoliated graphene patterned by helium ion microscopy, graphene flakes smaller than 500 nanometers, CVD graphene and graphene membranes, all with a level of detail unprecedented in the literature.

We begin by showing that TERS can reveal localized distribution of defects, strain and doping in the two-dimensional structure, generated by helium ion microscopy, which cannot be seen with regular confocal Raman microscopy. The Raman based protocols for defect, strain and doping characterizations are well-established in the literature, but here we demonstrate such characterization with $\approx 20\,\text{nm}$ spatial resolution.

Second, we demonstrate that, for a given defective graphene structure, Raman spectroscopy data acquired in the nanoscale, below the

diffraction limit, is different from data acquired by confocal Raman spectroscopy, for the same given sample. We explain such differences based on spatial interference effects, which happens within the phonon coherence length, as introduced in the literature. We show that such interference phenomena impact analysis protocols that are well-established and commonly applied as data characterization tools in the microscopic and macroscopic regimes, when moving into the nanoscopic regime. We therefore propose a parametrization based on the electromagnetic theory and on experimental data that, when applied to data acquired through TERS, provides a correction factor that can be used to adjust the obtained data, being of special interest to material sciences and for industry related endeavors.

All the previous results were obtained using atomic force microscopy (AFM) as the nanoantenna positioning tool. In this work we also show TERS based on scanning tunneling microscopy (STM) which, different from AFM, can also visualize electronic disturbances related to defects in the graphene lattice.

Finally, we demonstrate that the TERS system can be used not only to enhanced the spectral spatial resolution, but also as a nanomanipulation tool. We used the AFM tip to apply strain on a suspended graphene membrane and demonstrate tip-induced strain on graphene, graphene-substrate slip and graphene rupture.

Resumo

Este trabalho aborda aspectos fundamentais do uso da micro e da nanoespectroscopia óptica para a caracterização de materiais, em especial grafenos, com implicações potenciais em outras estruturas bidimensionais nanométricas. A diferença entre a micro e a nanocaracterização advém da limitação intrínseca à óptica convencional, consequentemente à espectroscopia óptica, de que a luz não pode ser localizada em uma região menor do que metade do seu comprimento de onda (da ordem do micrômetro), onde a difração torna-se um fator limitante à resolução espacial.

Para adaptar a espectroscopia óptica à nanociência, utilizamos um equipamento de caracterização química e estrutural que permite a manipulação da matéria em escala nanométrica, através da utilização de uma nanoantenna óptica. Conhecida como TERS, do inglês *Tip-enhanced Raman spectroscopy*, esta técnica combina a espectroscopia Raman, uma técnica limitada pela difração, com técnicas de microscopia de varredura por sonda (SPM — *Scanning probe microscopy*).

Em desenvolvimento no Laboratório de Nanoespectroscopia — LabNS da UFMG — desde 2007, este equipamento passou por melhorias substanciais durante este trabalho a fim de aumentar sua precisão, repetibilidade, estabilidade e usabilidade, tendo sido utilizado com sucesso na caracterização microscópica e nanoscópica de diversos tipos de estruturas de grafeno, incluindo grafeno exfoliado mecanicamente e nanoestruturado por feixe de hélio, flocos de grafeno com dimensões inferiores a 500 nanômetros, membranas de grafeno e grafeno CVD, todos com um nível de detalhe sem precedentes na literatura.

Começamos demonstrando que, em dada estrutura de grafeno bidimensional submetida a um processo de desbaste em um microscopio de feixe de ions de He, o TERS foi capaz de revelar, com precisão, a distribuição localizada de defeitos, deformações e dopagem, o que não é alcançado através da microscopia Raman confocal convencional. Os protocolos baseados em espectroscopia Raman para caracterização de defeitos, deformações e dopagem são bem estabelecidos na literatura na escala micrométrica, mas aqui demonstramos essa caracterização com resolução espacial de $\approx 20\,\text{nm}$.

Em seguida, demonstramos que, para uma dada estrutura de grafeno contendo abundante quantidade de defeitos, os dados obtidos através da espectroscopia Raman em escala nanométrica, abaixo do limite de difração, são diferentes, para uma mesma amostra, dos dados adquiridos por espectroscopia Raman confocal convencional. Explicamos essas diferenças com base em fenômenos de interferência que ocorrem dentro dos limites do comprimento de coerência dos fônons, conforme consta na literatura. Mostramos que esses fenômenos de interferência impactam, ao transitarmos para o regime nanoscópico, protocolos de análise já bem estabelecidos e comumente aplicados como ferramentas de caracterização nos regimes microscópico e macroscópico. Portanto, propomos uma parametrização baseada na teoria eletromagnética e em dados experimentais que, quando aplicada aos dados adquiridos através do TERS, fornece um fator de correção que pode ser utilizado para ajustar os dados obtidos, sendo relevante para a nanociência de materiais e, em especial, para a indústria.

Todos os resultados anteriores foram obtidos através da utilização da microscopia de força atômica (AFM) como ferramenta de posicionamento de nanoantenas. Neste trabalho, apresentamos também resultados de TERS com base em microscopia de varredura por tunelamento (STM), que, diferente da técnica de AFM, é capaz de visualizar distúrbios da estrutura eletrônica relacionados a defeitos na rede cristalina do grafeno.

Por fim, demonstramos que o sistema TERS não tem como única função uma melhoria da resolução espacial espectral, mas podendo ser utilizado também como ferramenta de nanomanipulação. Através da utilização da ponta de AFM, aplicamos, de maneira controlada, tensão em uma membrana de grafeno, demonstrando efeitos da tensão induzida pela ponta, além de efeitos de deslizamento do grafeno sobre o substrato e sua eventual ruptura.

Agradecimentos

Agradeço a minha família por todo amor e suporte. A minha amada esposa Helena, cuja trajetória, há mais de 20 anos, se mistura com a minha; aos meus filhos, Pedro e Mariana, que com sua deliciosa presença diária deram-me a oportunidade de saber o que é amor incondicional.

Agradeço a minha mãe Regina, meu farol sempre presente! Provedora de um carinho imensurável e presença constante na reta final.

Agradeço ao meu orientador Ado, por todo ensinamento, pela paciência, pela confiança depositada em meu trabalho e principalmente pela amizade. É uma honra fazer parte de seu time.

Agradeço ao Gusta, meu co-orientador e quem me recebeu de portas abertas no Laboratório de Nanoespectroscopia da UFMG, conduzindo-me com maestria pelo universo da nano-óptica. Sempre disposto a ensinar e a ajudar. Obrigado pelo carinho.

Agradeço ao Daniel, Xubaka e Mário por todo auxílio em minha jornada, pelas diversas aulas particulares que me deram, pelas boas risadas e pela amizade.

Agradeço ao Hudson, fiel companheiro nas mais diversas batalhas, dotado de imensa inteligência e de um senso de humor ímpar! Obrigado por toda ajuda e constante presença.

Agradeço ao Thiago L. Vasconcelos pela imensa receptividade em todas as visitas que fiz ao Inmetro, pela paciência em ensinar, além das inúmeras e frutíferas discussões sobre TERS. Cientista talentoso, de imensa seriedade e dedicação.

Agradeço ao João Elias, com quem tenho o prazer de trabalhar já há vários anos. Um oráculo na solução de problemas.

Agradeço à Márcia pela eficiência e competência sempre que necessária. Obrigado por toda ajuda, sempre muito importante.

Agradeço ao Prof. Achete, que através de todo seu apoio institucional e confiança em meu trabalho possibilitou o início de minha jornada na ciência.

Agradeço ao Rafael Alencar, com quem tive o prazer de trabalhar e de dar boas risadas.

Contents

List of Figures

1

Introduction

*"Nothing in life is to be feared,
it is only to be understood.
Now is the time to understand more,
so that we may fear less"*

— Marie Curie

In 1959, American physicist Richard Feynman made an iconic presentation [1] during the opening of the American Society of Physics Annual Meeting. Entitled *"There's plenty of room at the bottom"*, his lecture went unnoticed until the early 1990s, when it was rediscovered as the field of nanotechnology was starting to bloom. Considered nowadays to be ahead of its time, in his presentation Feynman hypothesizes not only the possibility of direct manipulation of atoms, but also that working matter on this scale would open the door to scientific advancements never imagined before. Despite some controversy regarding the lecture's actual impact in the origins of nanotechnology as a field of science, Feynman's speech is regarded as a milestone in the history of nanotechnology. It is not without a reason that nanotechnology rose from pure speculative science fiction to being considered a strategic research field by many governments worldwide [3]. It is on the nanometer scale that most life-critical biological processes occur, and it is on this scale that so-called quantum effects are predominant and as a consequence various material properties can be directly related to their size [4].

(a)

(b)

A historical example of the unintentional application of nanotechnology, which remained a mystery for centuries, can be seen in the Lycurgus Cup (Figure 1.1), a chalice from the fourth century BC that under the effect of a front illumination has a greenish appearance, however when back illuminated its color shifts to a vivid blood red. The mystery was only unraveled in 1990s when researchers discovered the existence of silver and gold nanoparticles, exhibiting odd optical properties due to its reduced size, with a diameter of $\approx 50\,\text{nm}$, impregnated in the glass [5].

FIGURE 1.1: (a) Lycurgus cup when illuminated from the front and (b) when illuminated from the back (apdapted from [2])

From its empirical utilization along the centuries to its rise in the last few decades, it is a fact that nanotechnology is ubiquitously present in a diverse number of areas and that its progress has been

fast. It took only 20 years from Feynman's lecture to the invention of the scanning tunneling microscope (STM) by IBM, the first device capable of manipulating and seeing a single atom, and another 20 years for the isolation of graphene, the first of an entire class of two-dimensional materials and seen as a strong candidate to complement or even substitute silicon as the basis of the electronics industry, amongst a myriad of other applications.

Market studies suggest that the global nanotechnology market will reach more than 170 billion USD in the next 5 years, with a compound annual growth rate (CAGR) of more than 15 % [6]. The race for the development of new materials is obviously followed by the need to understand and characterize those materials. The overall market demand for analytical instruments is forecast to increase more than 3.7 %(CAGR), reaching more than 30 billion USD through 2020 [7]. Currently, there is a diverse number of techniques capable of providing characterization at the nanometer scale, such as transmission and scanning electron microscopy [8] and those in the scanning probe microscopy family [9]. Although most of them are able to provide chemical or structural information from a sample, they usually require prior knowledge from the sample, special preparation techniques, precise control of ambient conditions and equipments generally only accessible to research groups with considerable budget. On the other hand, such information is readily and easily accessible through optical spectroscopy techniques.

Optical spectroscopy has been used as an important characterization technique since the XVII century [10], hundreds of years before Feynman's lecture and the nanotechnology boom. Optical spectroscopy requires little to no sample preparation and can be performed in ambient conditions with no impact on the samples' intrinsic properties, therefore it is considered vital for industrial applications and diagnostics, with relevant work being done in biotechnology [11, 12], biofuel [13, 14], soil science [15, 16], metrology [17–21] among other fields far beyond basic science. Of special interest is Raman spectroscopy, an optical spectroscopy technique based on the inelastic scattering of light [22] (see Section 2.1.2) and capable of providing not only chemical and structural information from a sample, but also to quantify important material properties such as defect characteristics, strain and doping.

However, as with any other optical technique, Raman spectroscopy is physically limited by diffraction in a phenomenon known as the diffraction limit [23], which states that propagating light cannot be

localized in a region smaller than approximately $\frac{1}{2}$ of its wavelength λ. Considering that the *ISO/TS 80004-2:2015* standard [24] defines "*nanoscale*" as the "*length range approximately from* 1 *to* 100 nm" and given that visible light has a wavelength of ≈ 500 nm, it is clear that optical systems are limited in their usefulness in nanoscience. To our knowledge, the idea on how to overcome this limitation first appeared in 1928 in the work of E. H. Synge [25]. Synge proposed that a sample should be illuminated from light coming from a source smaller than $\lambda/2$ and, therefore, surpassing the diffraction limit, a technique that would later be named near-field scanning optical microscopy (NSOM). Although the first NSOM system was only demonstrated in the 1980s [26], these systems evolved at a fast pace and in 2000 reached a milestone in the so-called tip-enhanced Raman spectroscopy (TERS) [27]. Using an optical nanoantenna [28], TERS combines confocal Raman spectroscopy with scanning probe microscopy (SPM) in a system capable of obtaining images and spectral information from nanostructures below the diffraction limit and reaching the so-called nanoscale. As a technique with a growing number of users [29], TERS has been applied, successfully, to a myriad of materials, from purely carbon based materials [30, 31], to semiconductors [32] and biological samples [33, 34].

The work presented in this thesis goes beyond the mere attempt to reach the *nano-realm*. Our experiments and analysis show that, when applied to nanocarbons, the proven characterization accuracy of Raman spectroscopy can be inaccurate or even inconsistent when comparing micro- and nano-Raman spectroscopy on the same sample. We show that the results differ not only in the typification of structural defects encountered on a sample but also in the estimated amount of the defects when comparing both techniques. As will be show, this difference is a consequence of interference and field confinement phenomena imposed by optical nanospectroscopy [35, 36], being of special interest from a metrological standpoint, specially for materials sciences and industry related endeavors.

In order to accomplish the results presented in this thesis, efforts have been made in two fronts: (i) the assembly of a TERS system with focus on precision, repeatability, stability and usability (see Section 3.1) and (ii) the development of reproducible and highly efficient nanoantennas (see Section 3.4).

The TERS system built was based on a system originally conceived and developed by Dr. Lukas Novotny and Dr. Achim Hartschuh [30],

[1]The Laboratory of nano-spectroscopy – LabNS – is located in the Physics department of the Federal University of Minas Gerais, Brazil.

nowadays at ETH Zurich and LMU Munich, respectively. Their original design was replicated, with permission, at the Laboratory of nano-spectroscopy[1], being throughly described by Dr. Paulo Araujo in his thesis [37] and serving as the basis for an optimized the system built and described here (see Section 3.1). The nanoantennas, as detailed in Section 3.4, are the result of a joint research project between UFMG and Inmetro, including the PhD thesis of Dr. Thiago L. Vasconcelos [38–42]

The text in this thesis is structured as follows:

Chapter 2 introduces the overview of important theoretical concepts necessary for understanding TERS and the TERS system developed, implemented and utilized for the experiments presented in this work, followed by an overview of graphene, the reference material used in our studies, with a focus on its characteristics with respect to Raman spectroscopy.

Given this theoretical foundation, Chapter 3 presents the technical aspects and developments necessary to perform the experiments and to analyze the obtained data. Details from our TERS setup are provided, as well as information regarding the sample preparation process. Also discussed is our highly-efficient nanoantennas, fundamental to the accomplishment of this work. This technical part is closed with an overview of the software developments done in-house to assist data analysis and image generation from the large amount of data acquired.

In Chapter 4, the experimental achievements from our micro- and nano-spectroscopy and nano-manipulation work are presented and discussed. Among many novel experimental results we show that interference related effects can impact optical measurements performed in the nanoscale and that this must be taken into account if existing Raman spectroscopy characterization protocols are to be used to analyze data acquired in the near-field.

Finally, Chapter 5 summarizes the work presented in this thesis.

Technical Appendices provide further technical details complementary to the information found in the main text that might be useful if the reader wants to go deeper in the intricacies of our experimental setup.

2

Theoretical Background

This chapter is divided in three sections: the first, Section 2.1, is dedicated to tip-enhanced Raman spectroscopy (TERS) and provides an overview of the developments that culminated with the invention of the technique; its origins and its building blocks: optical microscopy, Raman spectroscopy and scanning probe microscopy. Section 2.2 is devoted to graphene, the two-dimensional material foundational to this work, with an emphasis on the properties that make it the ideal reference material for TERS. Finally, Section 2.3 discusses why TERS in two-dimensional systems is specially interesting and important.

2.1 Tip-enhanced Raman Spectroscopy

2.1.1 Optical Microscopy & the Spatial Resolution

Optical microscopy can be defined as a technique invented to allow the visualization of structures that, due to their small size, cannot be resolved by the human eye [43]. Until around 400 years ago, the world of scientific observation was limited by the resolution of the naked eye [44], where every being, structure, distant star that could not be resolved by bare eyesight, remained unknown to mankind. The end of the 16th century marks the moment where scientists started to use lenses to magnify objects [45]. Although historians have not been able to give credit to a single individual for the invention of the microscope, the work of the Dutch scientist Antonie Philips van Leeuwenhoek has been recognized as fundamental for the development of the microscope and to the birth of the microbiology field as whole, with his optical devices being used and praise upon by important scientists such as Robert Hooke [46].

Since then, microscopes kept evolving at a rapid pace; single lens design was replaced by combined lens assemblies, which minimized aberrations and were the basis of multiple lenses microscopes [46]. At

first, most of the development was purely empirical, by trial and error, and there were a large number of microscope models available, which helped spread the invention across Europe in the 17th century [44]. Even with the evolution and improvements in the design and in the fabrication processes of lenses and microscopes, there was a clear problem that defied opticians and scientists alike, which consisted of the fact that, after a certain point, no matter how much you magnify something, the result is always a blurred unresolved image which was termed "empty magnification" [44].

$$\Delta X = \frac{0.61\lambda}{n\sin(\theta)}$$
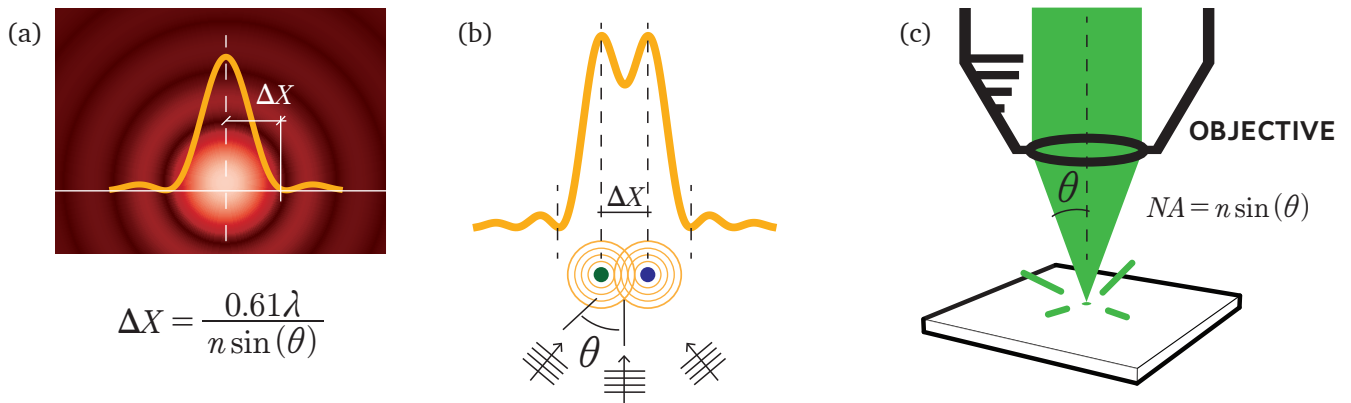
FIGURE 2.1: (a) two-dimensional representation of an emitter exhibiting a Gaussian beam pattern overlaid with its intensity distribution where ΔX is the Airy disk radius. (b) Schematic representation of the Rayleigh diffraction limit with two emitters placed at a distance of ΔX, therefore unable to be resolved individually (adapted from [47]). (c) Schematic representation of an infinity corrected microscope objective showing its half-angle θ.

The reason behind such blurriness only became understood in 1873, through the work of the German optical scientist Ernst Abbe [48]. Abbe showed that the maximum achievable spatial resolution of a microscopy system is, due to the diffraction phenomena, limited by the wavelength λ of the light used to illuminate the sample. Light waves, when focused in a region smaller than approximately $\frac{1}{2}$ of its wavelength, interferes with itself [48] in what became known as the Abbe diffraction limit or Abbe resolution limit. In 1879 Baron Rayleigh improved upon the work done by Abbe and defined what is now known as the Rayleigh criterion [49], which is given by

$$\Delta X = 0.61 \frac{\lambda}{n\sin(\theta)} , \tag{2.1}$$

where ΔX, shown in Figure 2.1(a,b) and known as the *Airy disk* radius (named after George Biddell Airy), is considered the minimum resolvable distance between two distinguishable features of a sample as a function of the light's wavelength λ, the index of refraction (IOR) of the medium, n, and the half-angle of the focal cone of light, θ, (Figure 2.1(b,c)).

Considering an object dimensionally $\ll \lambda$, its optical image, which is limited by diffraction, looks like a blurred, structureless shape, dimensionally equivalent to the Airy disk diameter. This is called

the Point Spread Function (PSF) of the system. The PSF is the impulse response of an optical system and thus contains the required information to determine its resolving power [50].

For practical applications, it is unusual to calculate the Airy disk diameter using the half-angle of the focal cone of light. Instead, a number most commonly provided by the vendors of microscope objectives is the numerical aperture (NA). The NA is a dimensionless number given by

$$\text{NA} = n \sin(\theta). \qquad (2.2)$$

Considering Eq. (2.1), we can conclude that the higher the NA, the smaller the minimum resolvable distance and consequently a better spatial resolution. Based on Eq. (2.2), knowing that the n of air is n $= 1$ and that $\sin(\theta) \leq 1$, the maximum achievable NA in air is NA $= 1$. If we consider an excitation wavelength $\lambda = 632.8\,\text{nm}$[1] and a microscope objective working in air, the minimum resolvable distance is $\Delta X \approx 386\,\text{nm}$. In order to increase the spatial resolution one can change the n of the medium. There are special microscope objectives, named *high NA objectives*, that are designed to be immersed into media with higher n than air (e. g. distilled water has n ≈ 1.33 [51], microscopy oil has n $= 1.518$). An oil immersion objective whose NA $= 1.4$, provides a minimum resolvable distance of $\Delta X \approx 276\,\text{nm}$, almost 30 % increase in spatial resolution when compared to an objective design to be used in air. Considering that visible light has a wavelength roughly between 400 to 800 nm, it is now clear why ordinary optical systems are not able to distinguish information in the nanometer scale, which greatly limits their usefulness in the nanosciences.

Technically, there is still a limitation related to the fact that the illumination from a single point in space is ideal. In real instruments, the detector receives light from different points as if they came from the same location. In 1957, American scientist Marvin Minsky filed a patent [52] for a microscopy apparatus that became know as the confocal microscope. Its usefulness comes from the fact that light originated from different points and depths along a sample will travel and hit the detector simultaneously with light originating from the region of interest, obfuscating its signal. In order to reduce the amount of light coming from these out-of-focus regions, a confocal microscope uses a concept known as point illumination, in which a sample is illuminated on a point-by-point basis, therefore limiting the emission of light from other parts of the sample. To further enhance the contrast, a pinhole element is placed in the detection path, in an optically conjugated plane, therefore blocking the light coming from

[1] From a Helium-Neon laser

FIGURE 2.2: Representation of the confocal principle where three different sample positions are depicted. The position of interest, represented by the solid blue circle, is the only feature that will get through the pinhole and into the detector, while the other features will get blocked by the pinhole. (adapted from [50]).
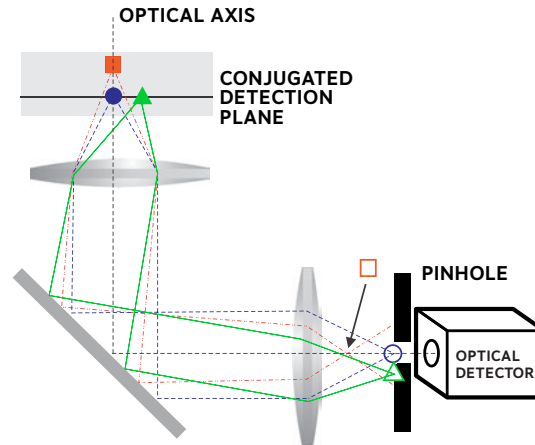
other regions from reaching the detector (Figure 2.2). One obvious, but significant limitation of this method, is the fact that some kind of scanning must occur in order to acquire the image of an entire object or region and, although there is an actual increase in lateral resolution when compared to a non-confocal microscopy system [50], confocal microscopy is still diffraction limited, nonetheless the idea of confocality and point-by-point optical scanning would prove to be invaluable.

Back in 1928, Edward Synge wrote a letter to Albert Einstein in which he proposed that, by shining light on a small particle whose diameter is $\ll \lambda$, the scattered field originated at the particle could be used as light source and, by scanning a sample with this particle, signal from an area equivalent to the particle diameter, therefore much smaller than the diffraction limit, could be acquired. At the time, Synge's idea, although considered theoretically correct, seemed to be of no use according to Einstein, but he recommended that Synge should pursue publication anyway [25, 28].

It took more than 50 years until Synge's idea completely came to fruition, mostly given the fact that, to realize such idea, the light source should be placed a few nanometers from the sample and this was technically unfeasible until the invention of the scanning probe microscope (see Section 2.1.3). The first half of the 1980s was specially productive for the development of SPM which directly impacted the optical field with the appearance of the scanning near-field optical microscopy (SNOM). The invention of the scanning tunneling microscope (STM) [53] at IBM in 1981 (see Section 2.1.3), gave rise to the SPM field and proved that the technology needed for precisely placing the light source at a nanometric distance from a sample surface and traversing it without crashing, was now a reality.

Through the use of piezoelectric actuators, it was now possible to approach an object so close to the surface of a sample as to acquire the evanescent optical near-field. Evanescent field is the name given to the electromagnetic waves that cannot propagate in free space, decaying exponentially as it leaves the vicinity of its source [54]. Knowing that an optical field is intrinsically composed of propagating and non-propagating components, it becomes possible to explain the lack of spatial resolution from a nanometric object, which is justified by the absence of the non-propagating, higher frequency spatial components in the detection plane [50, 55]. Therefore, in order to break the diffraction limit and to increase the spatial resolution in the optical regime, it is mandatory to acquire the information lost in the near-field, which means getting as close as possible, at a distance of only a few nanometers of the emitter [56–58].

Only three years after the invention of the STM, which provided the first images of individual atoms, Pohl *et al.* [59], also at IBM, were able to collect light through a sub-wavelength aperture that was precisely placed and controlled by piezoelectric actuators over a sample surface, obtaining the first optical image below the diffraction limit. By the end of the 1980s, the "*scanning near-field optical microscopy*" field was evolving at a fast pace [26, 60–63], and in 2000 it reached a milestone with the invention of Tip-enhanced Raman spectroscopy (TERS) [27, 64, 65], which will be explored in Section 2.1.4.

2.1.2 RAMAN SPECTROSCOPY

Raman spectroscopy [66] is an optical technique based on the inelastic scattering of light [22] and capable of providing information regarding the molecular vibrations of a material, allowing not only its chemical and structural identification, but also the quantification of several of its properties and how it responds to a diverse number of external effects, such as strain [67–71], doping [69, 72–74], functionalization [75–77], amount of defects and their characteristics [68, 78–83], among others.

The inelastic scattering of light was discovered in 1928 by Chandrasekhara Venkata Raman, an Indian physicist, while working on how light interacts with liquids and vapours [66]. Raman discovered that when light shines on matter, the light that gets scattered with the same frequency as the incident light "*is accompanied by a modified scattered radiation of degraded frequency.*" [66]. Such discovery earned him the 1930 Nobel prize in Physics and in his honor the phenomenon was named Raman scattering.
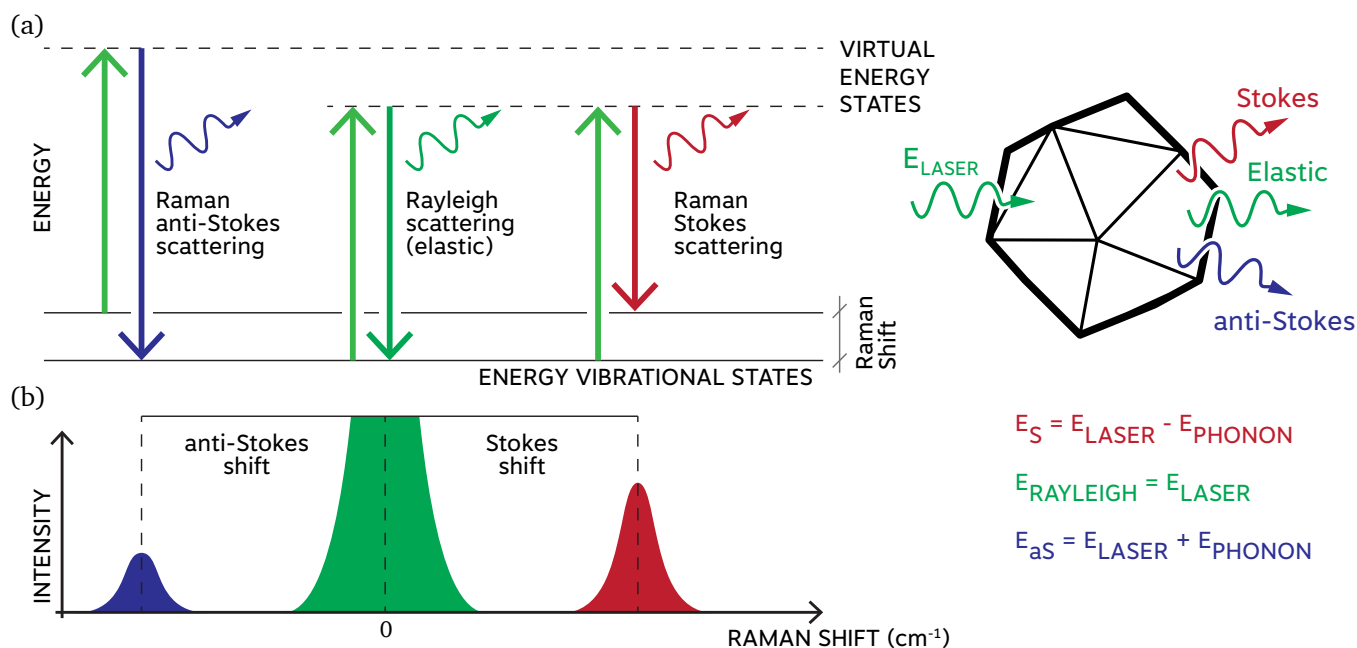
FIGURE 2.3: (a) Jablonski diagram [84] depicting the Rayleigh scattering as well as the Stokes and anti-Stokes Raman scattering processes in a material. The resulting scattering is given by the difference in energy between the initial and final states, which can be positive (Raman anti-Stokes process), negative (Raman Stokes process) or null (Rayleigh scattering). (b) Diagram representing the Raman shift versus the intensity of the emitted photons. The green peak represents the Rayleigh scattering, in which the wavelength of the emitted photons is the same as the incident photons. The red peak represents the Stokes Raman scattering with its longer wavelength. The smaller blue peak represents the less-likely to occur anti-Stokes Raman scattering, where the emitted photons have a shorter wavelength.

When a sample is illuminated by monochromatic light, such as a laser source, the incident light can be scattered elastically or inelastically [85]. In the elastic scattering, also known as Rayleigh scattering, the energy of the photons after its interaction with matter is preserved, whereas in the inelastic scattering, the energy of the scattered photons is different from the incoming energy, with the scattered photons showing an increase or a decrease in energy. When the energy of the scattered photon is larger than that of the income photon, the process is known as anti-Stokes scattering, whereas when the energy is smaller, the process is known as Stokes scattering. This is due to the interactions between the incident photons and the energy states that make up the material, usually the vibrational states. This frequency offset provides material-specific information and is called Raman shift. It is important to note that the inelastic scattering of light is orders of magnitude less intense than that of elastic scattering [86]. Roughly, for each 10^6 photons scattered elastically only one photon is subjected to inelastic scattering. The diagram in Figure 2.3(a), known as Jablonski diagram [84], depicts the energy vibrational states of a molecule as it interacts with light, and the possible interaction outcomes described above.

Raman scattering can be explained by the polarizability dependency on the molecular vibration [87]. Polarizability is a measure of how easy it is to distort the shape of a molecule's electron cloud by submitting it to an external electric field such as an electromagnetic wave. When an electric field is incident on a molecule, it forces the
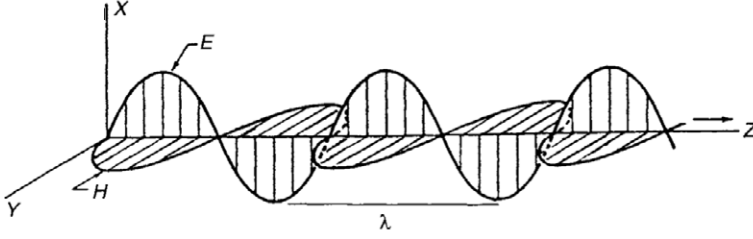
FIGURE 2.4: Linearly polarized electromagnetic radiation propagating in the z-axis. E is the electric field, H is the magnetic field and λ is the wavelength (from [88]).

nuclei and the electrons to move in opposite directions, generating an induced dipole moment. The intensity of this induced dipole moment is not only proportional to the intensity of the incident electric field, but also to the molecular polarizability. It is this change in polarizability during the vibrational motion of the molecule that is responsible for the Raman shift.

In classical physics, the Raman scattering effect can be explained as follows: a polarized electromagnetic wave from a monochromatic light source (i. e. laser), propagating in the z-direction, has two components; an electric field in the x-direction and a magnetic field in the y-direction, orthogonal to each other (Figure 2.4). Except when magnetic properties are under study, only the electric field component is relevant, therefore the magnetic field will not be considered here. The strength E of the electric field oscillating in the x-direction at a given time t is given by

$$E = E_0 \cos(\omega_0 t) \, , \tag{2.3}$$

where E_0 is the vibrational amplitude and ω_0 is the angular frequency of the laser, which is given by

$$\omega_0 = 2\pi \nu_0 \, , \tag{2.4}$$

being ν_0 the time frequency of the laser. When such electric field E interacts with a molecule, it induces an electric dipole moment p given by

$$p = \alpha E \, , \tag{2.5}$$

where α is the polarizability of the molecule (usually a tensor). Given that the molecule is vibrating with its own angular frequency ω_q, the nuclear displacements at time t are described by

$$q = q_0 \cos(\omega_q t) \, , \tag{2.6}$$

where q_0 is the amplitude vector of the vibration. For small distortions of the electron cloud, the polarizability α can be considered linearly proportional to the nuclear displacement q and is given by

$$\alpha = \alpha_0 + \left(\frac{\partial \alpha}{\partial q} \right)_0 q_0 + \cdots \, , \tag{2.7}$$
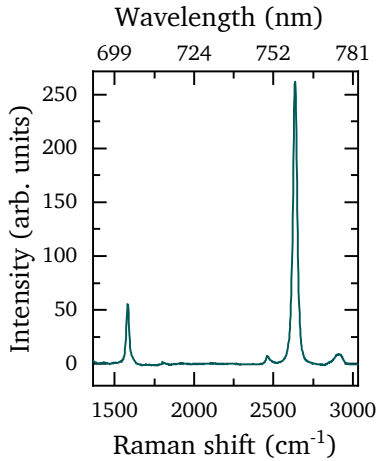
Wavelength (nm)

FIGURE 2.5: Graphene Raman spectrum. The inferior x-axis is plotted in Raman shift, while the superior x-axis is plotted in wavelength (nm). The y-axis plots the intensity in arbitrary units.

[2]The higher the local temperature of the material, the greater the probability of occurrence of the anti-Stokes phenomenon and, since it is known that the probability of occurrence of the Stokes phenomenon does not vary with temperature, the Stokes/anti-Stokes intensity ratio is a method for determining the local temperature of a material [89].

where α_0 is the polarizability at equilibrium and $(\partial\alpha/\partial q)_0$ is the rate of change of the polarizability α in respect to q, also at equilibrium position. The combination of (2.5), (2.6) and (2.7) results in the oscillating dipole moment P, given by

$$P = \underbrace{\alpha_0 E_0 \cos(\omega_0 t)}_{A}$$

$$+ \frac{E_0 q_0}{2}\left(\frac{\partial\alpha}{\partial q}\right)_0\left[\underbrace{\cos\left\{(\omega_0+\omega_q)t\right\}}_{B}+\underbrace{\cos\left\{(\omega_0-\omega_q)t\right\}}_{C}\right]. \quad (2.8)$$

The A, B and C terms correspond, respectively, to the Rayleigh scattering, Stokes and anti-Stokes Raman scattering, with the frequency of the scattered light given by ω_0, $\omega_0+\omega_q$ and $\omega_0-\omega_q$. It is important to note that in order to Raman scattering to occur, the molecule must be Raman-active or *polarizable*; based on Eq. (2.8), this means that the rate of change of the polarizability, given by $(\partial\alpha/\partial q)_0$, must be non-null.

Considering that the Raman scattering process is caused by the interaction of a photon with the atomic vibrations of the material, the concept of a delocalized *quasi-particle* known as phonon can be utilized. A phonon is an excitation that represents a quantum of vibration in the crystal lattice of a material. In the Stokes process, the lower energy scattered photon is a consequence of the creation of a phonon in the lattice, while in the anti-Stokes process the extra energy supplied to the scattered photon originates from a preexisting thermal phonon in the crystalline lattice of the material.[2] Due to the need of a preexisting phonon, the anti-Stokes process is less likely to occur, and consequently less intense than the Stokes process, as depicted by the smaller blue band in Figure 2.3(b).

A Raman spectrum is usually plotted in a two-dimensional graph where the frequency of the scattered light, the Raman shift, is recorded on the x-axis, while the intensity is recorded on the y-axis (Figure 2.5). The frequency must be presented in a physically relevant unit, such as the nanometer or wavenumber. Considering that Raman scattering is a process that revolves around the excitation wavelength, the data is usually reported in wavenumbers, $\tilde{\nu}$, in units of reciprocal centimeters, cm^{-1}, known as Raman shift. Raman shift can be interpreted independently of the excitation frequency and can be calculated as follows

$$\tilde{\nu} = \frac{10^7}{\lambda_0} - \frac{10^7}{\lambda_V}, \quad (2.9)$$

where λ_0 is the excitation wavelength and λ_V is the wavelength of the vibration mode, provided in nanometers. Based on Eq. (2.9), it is clear

that the Rayleigh wavenumber will have a zero value, whereas the Raman peaks will be shifted according to the associated normal mode energy, with the Stokes peaks being negative and the anti-Stokes peaks positive (Figure 2.3(b)). However, because the Stokes signal is much stronger, and therefore way more explored than the anti-Stokes signal, it is usually presented in the positive frequency shift range. In other words, by convention, both Stokes and anti-Stokes frequency shifts are multiplied by -1.

Figure 2.6 shows the Raman spectra from different sp^2 hybridized carbon based materials where, based on the analysis of these spectral signatures, one is able to extract relevant information from a sample, such as the effect of thermal treatment in a polycrystalline system (Figure 2.6(a)), quantification of defects in the crystalline lattice (Figure 2.6(b)), as well as counting the number of layers in a graphene sample (Figure 2.6(c)), to name a few.
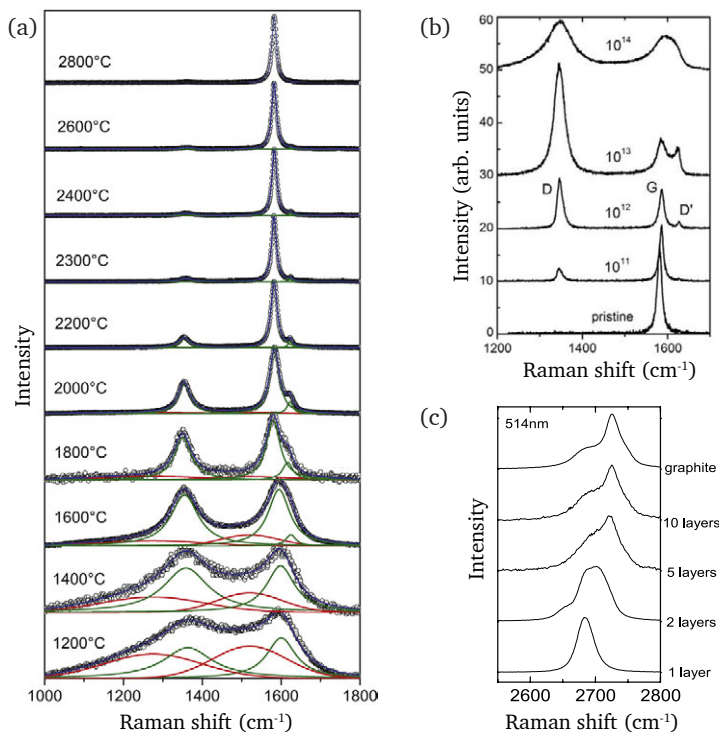
FIGURE 2.6: (a) Evolution of the Raman spectra of a graphene sample under thermal treatment (adapted from [90]). (b) Evolution of the Raman spectra of a graphene sample subjected to ion bombardment (adapted from [82]). (c) Raman spectroscopy based quantification of the number of layers in a graphene sample (adapted from [91]).

It should be clear by now the reasons that make Raman scattering such a powerful spectroscopic tool, where based on the analysis of scattered photons one can obtain a direct representation of the energies of the phonons, thus a representation of the energies of its vibrational modes, which can be seen as a fingerprint of the material under study. Relevant to this work, Raman spectroscopy has been especially important in the study, identification and quantification of defects in carbon nanostructures such as carbon nanotubes, nanographites and

graphenes [81, 92, 93], considered important prototype materials in the fields of nanoscience and nanotechnology [19].

At this point it is important to provide an overview of a typical micro-Raman system. Additional details regarding Raman spectroscopy of graphene, the reference material used in this thesis, will be explored in Section 2.2.

SCANNING CONFOCAL MICRO-RAMAN SETUP

As previously stated, compared to Rayleigh scattering and many other optical phenomena, such as photoluminescence, inelastic scattering is the least intense, therefore a Raman setup must be specially designed not only to provide appropriate filtering to remove the Rayleigh scattered signal from the much weaker Raman signal, but also to provide the necessary devices to quantify the amount of inelastically scattered light based on its energy.

In order to accomplish that, such a system must present the following major groups of elements: a monochromatic, narrow band, light source (e. g. laser), a focusing unit (e. g. microscope objective), a scanning stage and a frequency sensitive device (e. g. spectrometer with a photon detector attached, e. g. CCD). There is a myriad of ways of configuring a system for micro-Raman spectroscopy using the above-mentioned group of elements. Here we provide an overview of a possible configuration that has been successfully used by our research group, but it is important to note that any micro-Raman system will follow the same basic principles. Figure 2.7 shows the basis diagram of our scanning confocal micro-Raman spectroscopy setup.[3]

[3]As explained in Section 2.1.1, any confocal system capable of image generation, must provide a way to raster scan by moving either the sample or the excitation source.

A laser has its beam directed, through a series of optical elements, such as lenses and mirrors, to the back aperture of a microscope objective, through which the beam is focused on the sample of interest. Although it is possible to collect the scattered light from any direction, one efficient way of collecting is through a backscattering configuration, where the sample sits on a microscope and the same objective used for focusing is also used for collecting the scattered photons. Figure 2.7 shows an inverted microscope configuration, which has important advantages, such as to facilitate the use of oil-immersion high NA objectives, which, as explained in Section 2.1.1, provide not only a large solid collection angle θ (Figure 2.1(c)), but also an increased spatial resolution (as indicated by Eq. (2.1) and Eq. (2.2)). This inverted geometry also favors the coupling of the laser spot
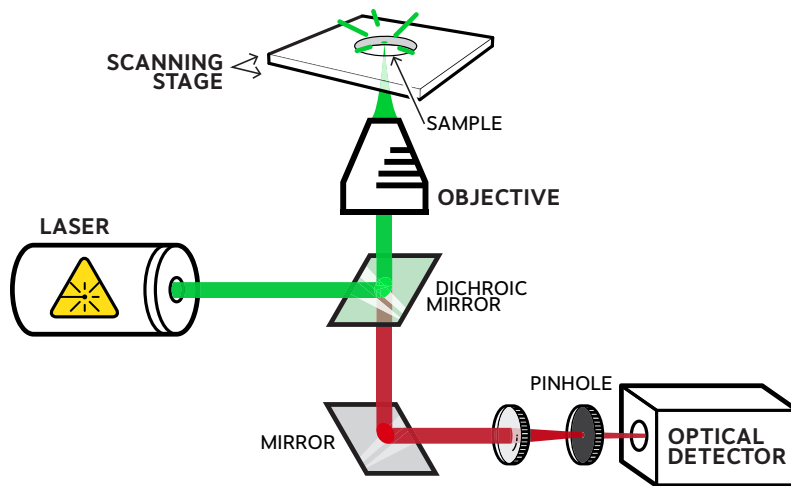
FIGURE 2.7: Schematic diagram of a scanning confocal micro-Raman system where the scanning is done by a moving the sample over a fixed laser spot.

with the scanning probe microscopy system as will be explained in Section 3.1.

At this point, after the collection of the scattered photons, it is necessary to optically separate the Raman scattered signal from the the Rayleigh scattered one, otherwise the Raman lines would not be experimentally observable. The frequency of the signal of interest is what guides the filter choice. For Stokes Raman, which presents a frequency lower than that of the excitation, a long-pass filter[4] is the obvious choice, the contrary is true for the anti-Stokes Raman, where the signal of interest has a higher frequency than that of the excitation, in which case a short-pass filter is used. In order to collect both the Stokes and anti-Stokes Raman simultaneously, a notch filter is necessary.

[4]Optical filters are usually specified based on the working wavelength. As an example, a 760 nm long-pass filter is designed to block all the wavelengths ≤ 760 nm, allowing only longer wavelengths to pass, while a 760/12 nm bandpass filter is designed to block all the wavelengths outside the 760 ± 12 nm window.

It is important to note that, depending on the intensity of the Rayleigh scattered signal, more than one filter in series might be needed. This is due to the fact that any optical filter has a limited degree of blocking, specified by the manufacture as its optical density (OD). The percentage of transmitted light T can be calculated by

$$T = 10^{-OD} \times 100\% , \qquad (2.10)$$

while the optical density as a function of T can be calculated by

$$OD = -\log \frac{T}{100\%} . \qquad (2.11)$$

Due to the special need of efficiently blocking the elastic scattered photons, there are filters designed specifically for Raman spectroscopy, which usually provide OD = 3 or higher.

After going through one or more optical filters, as described above, the Raman scattered light is then directed to a spectrometer, a funda-

[5]Spectrometers may have on (single), two (double), or three (triple) grattings in series for light dispersion.

[6]For more information about diffraction gratings, including instructional material, see e. g. [95, 96].

mental device in any optical spectroscopy setup. The spectrometer is an equipment designed to separate the incoming light into its constituent components, usually through a diffraction grating, and directing them to an optical detector, such as a charge-coupled device (CCD) array, where, depending on the characteristics of the spectrometer and its attached sensor (such as grating density and pixel size, respectively), high spectral resolution, below $1\,\mathrm{cm}^{-1}$, can be achieved. Figure 2.8(a) shows the schematic representation of a spectrometer based on the Czerny-Turner design, commonly used in most modern single-monochromator spectrometers,[5] to which a CCD detector is usually attached.

The incoming light initially goes through a slit and then it hits a parabolic mirror, which collimates and directs the light to a diffraction grating attached to a motorized element known as turret. The turret (Figure 2.8(b)) is usually comprised of three or four sides to which reflective diffraction gratings, with varying characteristics, are attached, providing the user freedom to choose a grating based on experimental needs.[6] The light deflected by the grating will travel at discrete angles, based on the wavelength and grating characteristics, in the direction of a parabolic mirror, which is responsible for focusing the spectrally resolved light on the detector.

Systems comprised of highly sensitive CCD detectors, usually work in the following manner: based on a user chosen acquisition period, the charge accumulated at each pixel of the CCD is read and the intensity of each column of pixels is plotted in a graph where the x-axis, in a calibrated system, corresponds to the wavelength of light that strucks that column position, which is based on the angle of the diffraction grating. The acquired and processed spectrum can then be displayed in wavelength (nm), Raman shift (cm^{-1}) or even pixels.
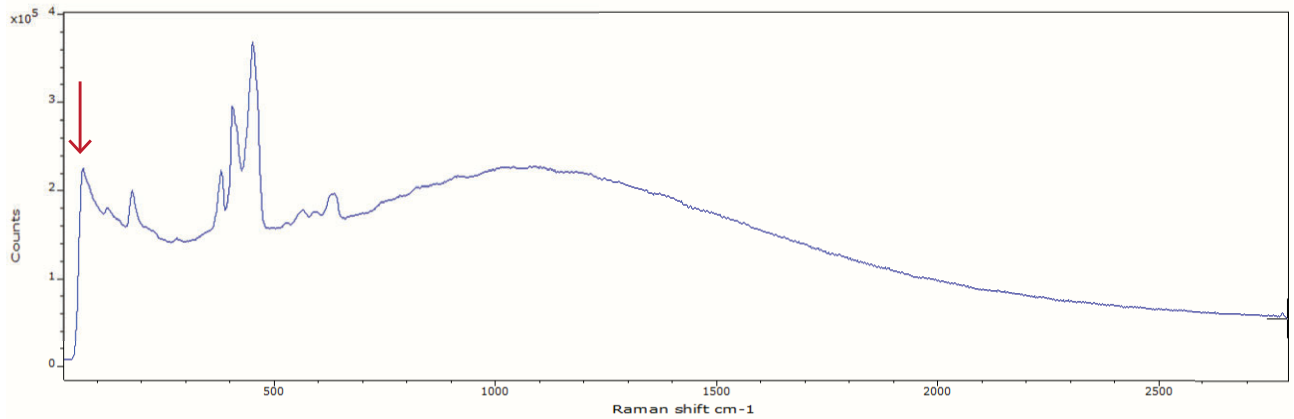
On the vertical axis, the intensity corresponding to each wavelength is plotted. Figure 2.9 shows the Raman spectrum of a MoS$_2$ sample (Molybdenum disulfide) obtained with such a system, after a 100 s accumulation time and without any post processing.

Highly sensitive detectors, such as the ones used for Raman spectroscopy, are usually peltier or nitrogen cooled to reduce thermally induced noise, which is necessary in order to detect such very low intensity signals. Due to this high sensitivity, most of these devices are still able to detect the Rayleigh scattered light even after going through a filter with high OD,[7] where depending on the laser power and spectral accumulation time, enough Rayleigh scattered light can get through and reach the detector, completely dominating the Raman signal of interest or, in more extreme cases, damaging the detector. In a spectrometer, this can usually be solved by rotating the turret, to which the diffraction grating is attached, in such an angle as to direct the undesired Rayleigh scattered wavelength out of the optical path that goes to the detector. The red arrow in Figure 2.9 shows the cut-off point of the long-pass filter used during acquisition, wavelenghts longer than that will not get blocked and hit the detector.

Another important class of photo-detection devices, specially for very sensitive detection needs, is the avalanche photodiode (APD), more specifically those used in devices known as single photon counting modules (SPCM). These are extremely fast and sensitive devices generally used for time-critical applications, such as time correlation [97]. The disadvantage of such devices is the fact that they exhibit only one detecting unit, thus in order to be used as a frequency selective imaging device, some external wavelength selection apparatus must be utilized, such as an optical bandpass filter, which allows only a range of frequencies to reach the photodetector.

[7]The long-pass dichroic beamsplitter used in our system is a Semrock 632.8 nm RazorEdge with an $OD = 3$ ($T = 0.10\%$). For most fluorescence microscopy applications such T is usually enough, but, based on our experience, an $OD \geq 6$ ($T \leq 0.0001\%$) is usually required for Raman spectroscopy when using a single monochromator spectrometer. Triple-monochromators can operate even without Rayleigh filtering.
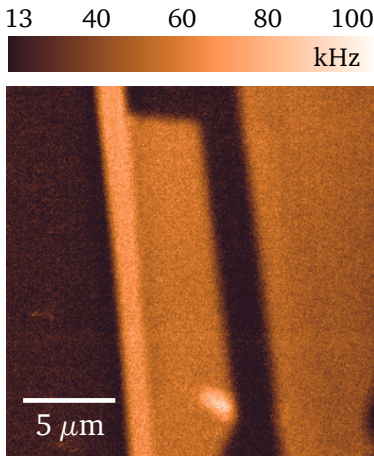
FIGURE 2.10: APD image of a graphene flake generated by raster scanning the sample. The APD was equipped with a 760 ± 12 nm bandpass filter. Given an excitation wavelength of 632.8 nm, such a filter is appropriate for imaging the graphene 2D band that originates from a second-order process, involving two-phonons (see Section 2.2). The color scale bar at the top indicates the APD detection count in frequency, where the brighter the pixel, the higher the photon count.

In our setup, the APD[8] is mostly used as an exploratory device, being equipped with an appropriate bandpass filter based on a previously chosen Raman band and the sample is raster scanned. Each pixel in the acquired image corresponds to the intensity of the selected Raman band at that sample location (Figure 2.10). The combination APD/spectrometer/CCD array was fundamental for the work presented in Chapter 4.

2.1.3   SCANNING PROBE MICROSCOPY — SPM

Scanning probe microscopy (SPM) is a branch of microscopy developed to analyze materials surface and their properties with high spatial resolution, through the use of an atomically sharp tip that traverses – raster scans – the surface of a sample while interacting with it [98]. SPM is capable of mapping the surface of solids, frequently achieving atomic resolution, in which individual atoms can be located in the crystalline lattice, thus being able to reveal not only perfect atomic distribution, but also the existence and location of defects, and to reach resolutions as high as 10 pm [99].

In SPMs, a sensor is responsible for monitoring the tip/sample interaction and feeding the acquired data to a feedback control system, which is in turn responsible for keeping the probe in the operating range designated by the user, being achieved through the use of actuators to which the probe is attached. There is a myriad of tip/sample interaction methods that can be employed and the nature of the chosen method determines the characteristics of the acquired data, which can then be processed and used for image synthesis, if desired. The resulting image can reflect numerous characteristics from the sample, such as: topography, mechanical, electrostatic, magnetic, among other properties [100].
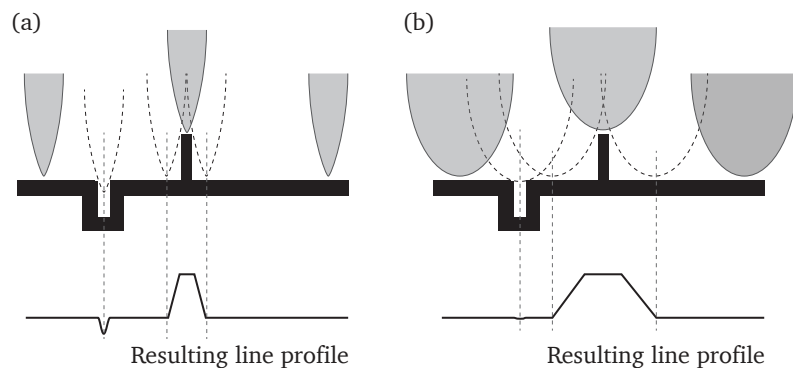
FIGURE 2.11: Illustration depicting the impact of a tip's apex dimension on the spatial resolution achieved. (a) A sharp tip traversing a sample and the obtained line profile. (b) The same as (a), but with a larger tip.

Analogous to what was briefly described in Section 2.1.1, the concept of a point spread function (PSF) can also be applied to SPM [101], but here the spatial resolution achieved is proportional to the dimen-

sions of tip's apex, which, in the end, has the same purpose of acting as a measure of resolving power (Figure 2.11). Due to the usual fragility of SPM tips, mechanical and electrical stability of an SPM system is paramount. In most tips, the slightest collision with the sample surface will most likely cause the tip's apex to deform, largely increasing its dimensions and consequently reducing the achievable resolution. In the case of TERS probes, in which surface plasmons resonance (see Section 3.4) plays a crucial hole, the smallest deformation of the tip's structure might render it unusable for near-field spectroscopy. High quality TERS probes usually have an apex of around 10 nm, while its composition actually depends on the excitation wavelength (more on the probes used in our TERS system in Section 3.4).

▶ GENERAL OVERVIEW

In order to obtain an actual image from a sample's surface, some kind of scanning must be performed, which usually happens in one of two ways: by keeping the sample fixed in place while traversing the tip over it, or by keeping the tip fixed in place while moving the sample beneath it. In both cases usually the tip is free to move in the z-direction. The former is most common in scanning tunneling microscopy (STM) while the later is more common in atomic force microscopy (AFM) systems (these two techniques will be described later in this text) and it is also the way it is usually done in most TERS systems, due to the fact that the nanoantenna must always be aligned to the laser focal point.
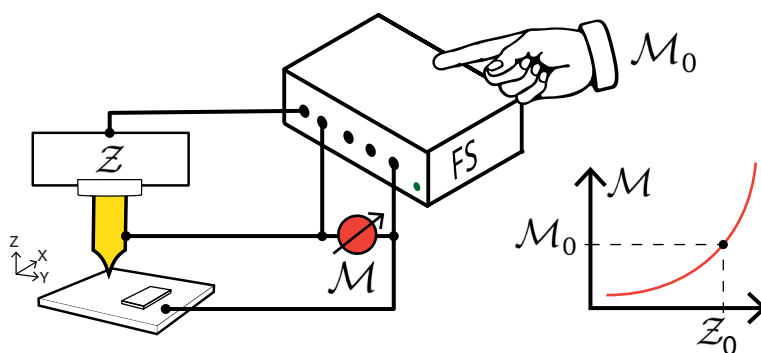
FIGURE 2.12: Schematic diagram of an SPM feedback system (adapted from [102])

When the probe is moving over the sample surface, a feedback system is responsible to control the probe/sample distance in order to keep the probe from crashing into the surface. This is done through a control loop, where the interaction magnitude $\mathcal{M}$ is read by a sensor and compared to a set point value $\mathcal{M}_0$ provided by the user (see schematic in Figure 2.12). The feedback system's objective is to keep

$\Delta \mathcal{M} = \mathcal{M}_0 - \mathcal{M}$ as close to zero as possible. Considering an user configured and fixed $\mathcal{M}_0$, this is only possible by imposing a change in $\mathcal{M}$, which is achieved by acting on the probe/sample distance $\mathcal{Z}$. The probe/sample distance $\mathcal{Z}$ and the interaction magnitude $\mathcal{M}$ are related through the equation $\mathcal{M}(\mathcal{Z}) = \mathcal{M}$, where a change in $\mathcal{Z}$ causes a change in $\mathcal{M}$. It is important to note that in order for this to work, there must be a unique depence of $\mathcal{M}(\mathcal{Z}) = \mathcal{M}$. From a construction standpoint, a change in $\mathcal{Z}$ is usually produced by acting on piezoelectric elements to which the probe is attached. Therefore, changes in $\mathcal{Z}$ lead to changes in $\mathcal{M}$.

Regarding image formation, where it is possible to abstract which element is moving, feature variations on the sample's surface induce changes in $\mathcal{M}$. It is the feedback system responsibility to act in order to restore $\Delta \mathcal{M}$ to zero, in real time. For every single point $P_{(x,y)}$ scanned on the sample, there is a correlated voltage value $V_{(x,y)}$ calculated by the feedback system and applied to the piezoelectric actuator, in order to keep $\Delta \mathcal{M} = 0$. The $V_{(x,y)}$ value for each point $P_{(x,y)}$ is then used to generate a pixel $\text{Im}_{(u,v)}$ in the resulting SPM image, where u and v are given in image coordinates, but can be related to actual distances on the sample due to previous system calibration.

Two widely established SPM techniques are the Scanning Tunneling Microscope (STM) and Atomic Force Microscopy (AFM). The TERS system developed and used in the work presented in this thesis (see Section 3.1 and Chapter 4) is capable of operating with either STM or AFM and what follows is an overview of both techniques.

SCANNING TUNNELING MICROSCOPE (STM)

The birth of the SPM field took place at IBM in 1981 with the invention of the STM by Swiss scientists Gerd Binnig and Heinrich Rohrer [53], awarded with the 1986 Physics Nobel prize. STMs revolve around the tunneling current, a quantum mechanical effect that occurs when a metal tip is approached at a very short distance, in the order of 1 nm, to a surface with a different electrical potential [99]. Due to this potential difference, electrons may tunnel through the dielectric medium that separates the sample from the tip, causing the emergence of an electric current named tunneling current. This effect is also responsible for the very high lateral resolution, in the atomic scale, achieved by STMs. In order to flow, the tunneling current must find the shortest distance from the tip's atomic structure to the atomic structure of the sample, which happens from the very last atom of
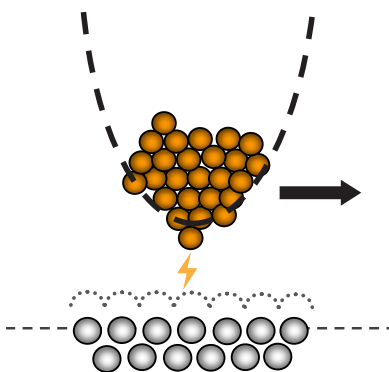
FIGURE 2.13: Depiction of an STM tip showing how it achieves atomic resolution (adapted from [102]).

the tip's apex to the sample surface, which provides great spatial resolution, thus it is important to note that the actually achieved resolution in a STM experiment cannot be solely based on a measure of the tip's apex diameter, although a very sharp tip has a higher chance of providing better resolution, due to the smaller amount of atoms at the tip's apex from which the tunneling current might jump (Figure 2.13).

Being based on a quantum phenomenon, the tunneling current is very small, usually ranging from hundreds of pA to tens of nA, and it is a function of basically three factors, namely, the tip/sample distance, the tip/sample potential difference and the density of electronic states of the tip/sample system. It is not uncommon to say that SPMs map the topography of a sample surface, although this is technically not correct in case of STM, where what is actually getting mapped is the density of electronic states, which can be different from the actual geometrical topographical features.

From a quantum physics perspective, STM is based on the finite probability that an electron with energy E might surpass a potential barrier $\phi > E$, something that would be forbidden in classical physics. The probability of such occurrence decreases exponentially with the width of the energy barrier. As an example, considering a gold tip over a gold film in vacuum, the tunneling current decays one order of magnitude for every 0.1 nm change in distance [99].

Since STM revolves around current detection, an important element of every STM system is the transimpedance amplifier, known as preamp in STM jargon. Such element is responsible for converting the small tunneling current into voltage and amplifying it to working levels (see Section 3.2). It is the voltage and not the current that is usually feed to the feedback system controller. The need of such a current path is actually a limiting factor of STMs, where the sample must be conductive and there must be a closed circuit through which the current can flow. The necessary potential difference needed between the tip and the sample is created by applying a bias voltage to either the tip or the sample, and usually ranges from 0.01 to 1 V.

STM is one of the most powerful techniques to explore crystalline domain related issues, since any change in the crystallyne lattice usually has noticeable effects on the electronic structure of the material and therefore can be identified by STM [103, 104], where atomic force microscopy (AFM) (see Section 2.1.3) is mostly inadequate. For such reason it was utilized for the work presented in Section 4.4
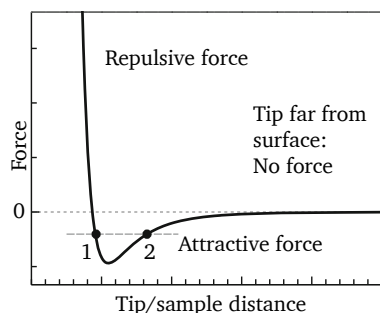
FIGURE 2.14: Plot depicting the qualitative behavior of van der Waals forces as a function of tip/sample distance (adapted from [98]).

ATOMIC FORCE MICROSCOPY

IBM's innovation in the scanning probe microscopy realm wasn't limited to the invention of the STM. In 1986, a group of researchers also working at IBM labs in Zurich, invented the Atomic Force Microscope (AFM) [105], a technique based on atomic level interaction forces that can be applied to a wider variety of samples and without the need of applying any kind of electrical potential between sample and tip. While STM is based on the tunneling current, where the sample must be conductive and there must be a path for the current to flow, the operation of an AFM is based on interaction forces that exist between the tip and sample, specially the van der Waals forces.

Van der Waals forces can be described as a distance based atomic interaction that is present between two or more non-bonded systems, presenting itself as either attractive or repulsive in nature. When molecules without a permanent dipole moment approach each other, an attractive force arises due to the formation of a fluctuating dipole moment, but if the distance becomes too small, to a point known as the van der Waals contact distance, the force becomes repulsive due to the overlap of the electron clouds (Figure 2.14).

As with STM, AFM systems rely on the utilization of a sharp tip that traverses the sample surface, although the detection method employed is obviously different. An AFM tip is usually assembled on what is called a force sensor, being silicon cantilevers the most common one. Another type of force sensor, less frequently used, is the quartz tunning fork, such as those used as oscillators inside wristwatches. The AFM-TERS system used in this thesis uses quartz tuning forks as its force based sensor for reasons that will be described.

▸ CANTILEVERS AS SPM SENSORS
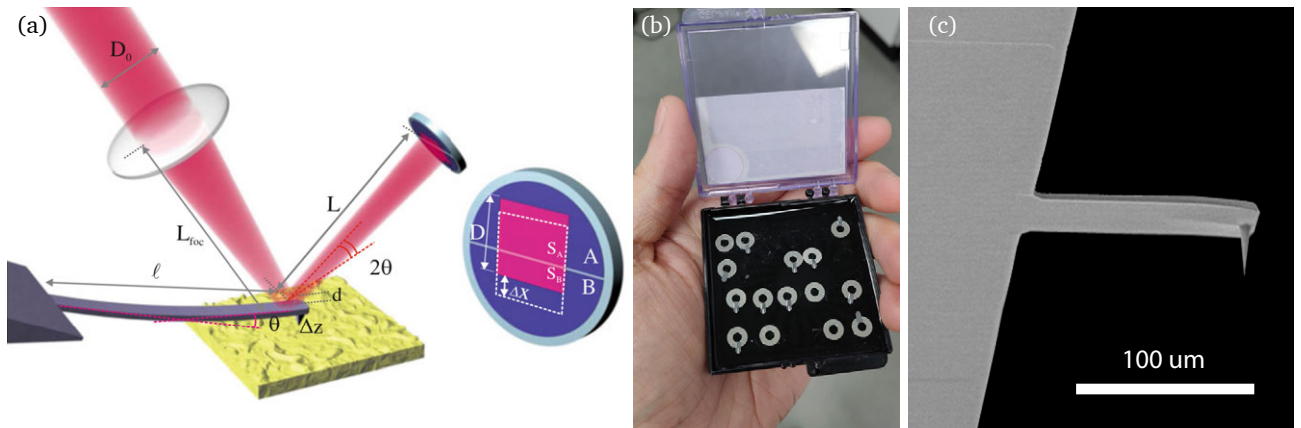
AFM cantilevers are usually made of silicon, through a lithographical process, in which the final product consist of a silicon beam with a sharp tip at one end whose apex usually measures units of a nm (Figure 2.15). As the cantilever scans the surface of a sample, due to its small beam thickness, usually between ≈ 3 to $5\,\mu$m, it gets deflected due to its interaction with the van der Waals forces. A laser beam that is incident on the back of the silicon beam gets reflected towards a position sensitive device (PSD). Slight shifts in position due to the cantilever's deflection are detected by the PSD and topographical data can be derived from the detected signal. The same detected signal is also used as a feedback signal by the system's controller (Figure 2.15(a)). According to Voigtländer [98] deflections ΔZ as small as $0.2\,$pm can be detected.

▸ TUNING FORKS AS SPM SENSORS

Quartz tuning forks (QTF), are mechanical oscillators that, due to the intrinsic piezoelectricity of quartz, transduce mechanical stress into electricity and vice-versa. Commercially available QTF are provided with metal plates that act as electrodes through which an applied electrical field is able to promote a mechanical oscillation of the quartz crystal. The contrary is also true: when submitted to an external oscillation, the QTF generates an electrical current that can be collected from the electrode's terminals. The frequency in which the QTF vibrates, deemed its resonant frequency, is defined based on the geometry and mass of the element, with a diverse number of frequencies readly available in commercial form, being $32\,768\,$kHz the most frequent one [98]. Such frequency is the one used in our AFM-TERS system.
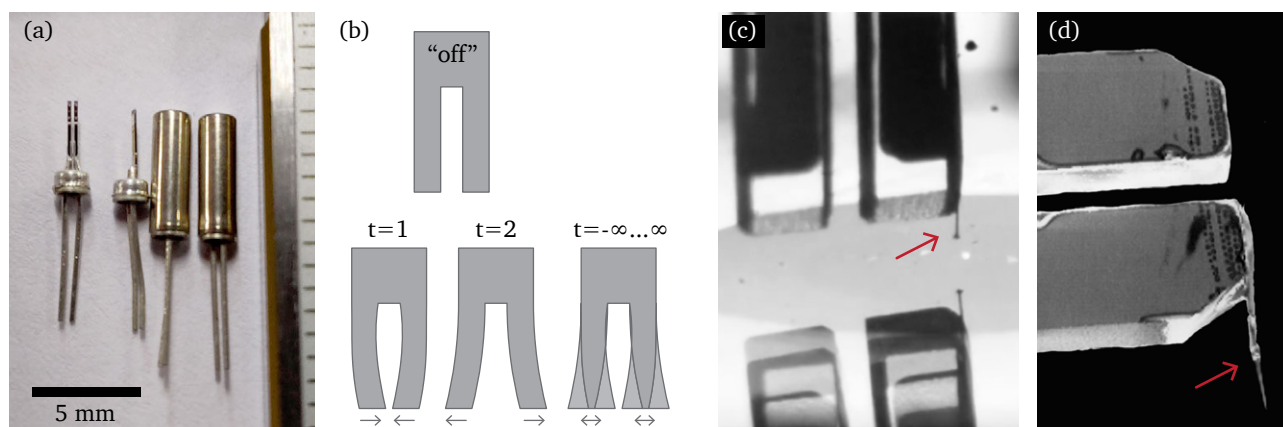
FIGURE 2.16: (a) QTF, originally commercialized for timing applications, with and without its encapsulation. (b) QTF vibrating in flexure mode. (c) QTF with a tip attached parallel to one of its prongs (red arrow). The QTF coming from below the image is a reflection of the actual QTF on the sample surface. (d) QTF with a tip attached orthogonally to on of its prongs (adapted from [107]).

There are a number of reasons for choosing quartz tuning forks as sensors. One of the advantages is the fact that the same quartz tuning fork found inside wristwatches can be used as AFM force sensors (Figure 2.16(a)), and due to their large availability, they are cheaper than commercially available silicon cantilevers. Commercially available AFM cantilevers are usually sold ready for usage, while when using a wristwatch tunning fork based solution, one must find a way to attach an actual tip to the sensor, which might be seen a disadvantage at first, but in the case of our research group, the TERS tips we use were idealized and are produced *in-house*, and assembling them to a quartz tuning fork is actually easier than trying to do that on silicon cantilever, mostly due to its smaller dimensions and larger price. Another advantage to quartz tunning fork based sensors is the fact that the signal detection does not depend on any external optical system, being entirely electronic, which greatly simplifies the setup and since, in our case, we have a spectroscopy system, the mere presence of extraneous light sources could impact our measurements.

In order to be used for AFM, a sharp tip must be attached to one of the QTF prongs. When oscillating, its prongs move in the way depicted in Figure 2.16(b), therefore the way the tip is attached, determines how the scan is going to happen. Usually only two ways of attaching the tip are considered: parallel or perpendicular to one of the prongs (Figure 2.16(c, d), respectively). In (c), known as shear-force, the deflection happens parallel to the sample surface, while in (d), known as tapping-mode, the deflection is orthogonal to the sample surface.

Here we are going to provide a basic overview of how an AFM system based on QTFs usually works: the QTF, with the tip already attached to one of its prongs is forced to oscillate at its resonant frequency and a phase-locked loop (PLL) monitors the phase or the

amplitude of the signal as a function of the driving frequency. As the tip approaches and interacts with the sample, it causes a small change in the QTF oscillating frequency. As shown in Figure 2.17, at the resonance peak there is a considerably large change in phase as a function of frequency, therefore, even the slightest shift due to tip sample interaction can be detected by the PLL, that acts to keep the frequency shift at a user specified set point. This is usually done by extending and contracting a piezoelectric element to which the QTF is attached, consequently changing the tip/sample interaction. A number of measured parameters, such as the signal amplitude, frequency variation, as well as the voltages applied to z-piezo during a scan can be utilized for image synthesis.

Finally, it is important to note that, in the case of our system, besides the differences in interaction modes in which AFM and STM are based, most of the instrumentation is the same and shared among both techniques, apart from the current preamplifier, exclusive to STM, and the need for a PLL, exclusive for AFM. The SPM controller, the scanning stage and piezoelectric actuators are used interchangeably.

FIGURE 2.17: Frequency sweep response from a quartz tuning fork. The upper plot shows the amplitude response as a function of frequency. The bottom plot show the phase response as a function of frequency.

2.1.4 TIP-ENHANCED RAMAN SPECTROSCOPY — TERS

Although through Raman spectroscopy one is able to obtain chemical, structural and functional information from a sample, it is still a diffraction limited technique. On the other hand, scanning probe microscopy usually provides much higher spatial resolution, even reaching the sub-nanometric level, but, as shown, the level of information it is capable to extract from a sample is limited.

TERS is a near-field scanning optical microscopy (NSOM) technique that combines a scanning confocal micro-Raman spectroscopy system (Section 2.1.2) with a SPM (Section 2.1.3) in which the SPM tip acts as a nanometric sized optical antenna. This nanoantenna, when correctly placed in the focal point of a strongly focused laser beam, and only a few nanometers away from the sample under investigation, is capable of locally enhancing the excitation field and to detect the evanescent waves that originate from the interaction of light with sample features smaller than its wavelength, transferring to the far-field information that would otherwise be "trapped" in the near-field regime. As a consequence, the spatial resolution is no longer limited by the wavelength of the excitation source, but by the nanoantenna's apex radius, which can be $\approx 10\,\text{nm}$ [50, 108], therefore providing structural and chemical information from a sample in the nanometric scale. TERS has already been used to characterize isolated dopant atoms in nanostructures [78] and recently resolu-

FIGURE 2.18: Diagram showing different microscopy techniques with their chemical specificity as a function of spatial resolution. TERS combines advantages from both Raman and SPM. (adapted from [47])
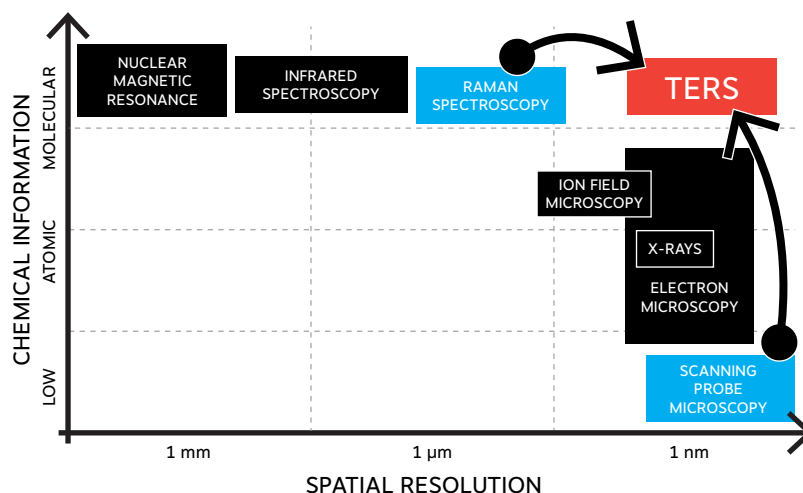
tions in the Angstrom scale have been achieved [109, 110] where the actual optical sensor is one or a few single atoms at the end of the nanoantenna.

Figure 2.18 is a diagram showing different microscopy techniques with their chemical specificity as a function of spatial resolution. TERS is the result of two Nobel prize winners: Raman spectroscopy and SPM.

The first documented enhancement of a Raman signal was done by Fleischmann *et al.* in 1974 [111], where a small amount of pyridine molecules adsorbed on a silver electrode, which acted as a substrate, had its Raman signal largely enhanced. Following Fleischmann's footsteps, other publications showed that specially prepared metallic surfaces, usually roughened or containing clusters of nanoparticles, could enhance the scattered Raman signal by orders of magnitude [112], possibilitating even the detection of single molecules [113, 114]. Named surface-enhanced Raman scattering (SERS), this technique showed that, through plasmonic ressonance, scattered signal from the near-field regime could be detected and propagated to the far-field [115]. Although largely utilized since the 1970s, SERS is still a diffraction limited technique, due to the fact that the incident laser illuminates a large number of nanoparticles at the metal surface, which, in the end, act as multiple nanoantennas. Therefore, even if SERS is capable of detecting near-field signal coming from single molecules, it is not possible to precisely localize from where the near-field signal originated.

Looking back, it might seem obvious that by reducing the surface area of the metal substrate, minimizing it to hold a small number of nanoparticles or even a single nanoparticle, could drastically improve

spatial resolution, but it was only in 1985 that Wessel proposed "*A new concept ... for an optical probe with spatial resolution unlimited by diffraction effects.*" [116]. In his proposal, a submicrometer-sized antenna would be controlled by an SPM system in close proximity to the sample surface and collect the incoming electromagnetic field. Although very similar to what was proposed by E. H. Synge in 1928 [25], Wessel's article has no mention to Synge's work and also remained in the theory realm.

The year 2000 was specially important in the field of nano-optics, where four independent groups published results in which Raman spectroscopy measurments were conducted in the nanoscale regime with the help of metallic tips controlled by SPM systems [27, 64, 65, 117]. Of all the published works, the name **tip-enhanced Raman spectroscopy** was debuted by Stöckle *et al*. Titled "Nanoscale chemical analysis by tip-enhanced Raman spectroscopy", this work demonstrated that the utilization of a metal tip brought into close proximity to a sample surface could indeed greatly enhance the Raman scattered signal, as with SERS, but with the added, and previously predicted advantage of providing high spatial resolution, which was no longer limited to the wavelength of the excitation source, but to the dimension of the tip's apex. The assembled system used an AFM for tip control, which was placed on top of a backscattering configuration, similar to the system described in Section 3.1. Such a combination of SPM and micro-Raman setups soon proved to be ideal for this newly created SNOM field.

The evolution of SPM provided the much needed control over the critical tip/sample distance. The optical signal intensity decays exponentially as the tip/sample distance z increases, as given approximately by $I \propto (z + r_{\text{tip}})^{-8}$, where r_{tip} is the tip radius [35, 118, 119].

SPM allowed not only a precise tip positioning anywhere on the sample, but provided the added advantage of bringing relevant information not readily available through optical spectroscopy, such as topographic data and local density of states, for STM. Since this additional information is acquired simultaneously with the acquisition of the optical signal in TERS measurements, it can be directly correlated to the Raman spectroscopy data, further enriching the obtained results even from biological samples in aqueous solutions [120].

Following Stöckle *et al*. publication [27], a large number of TERS related work has been published [121–125] in which either AFM or STM have been utilized [126–133] and combined with various
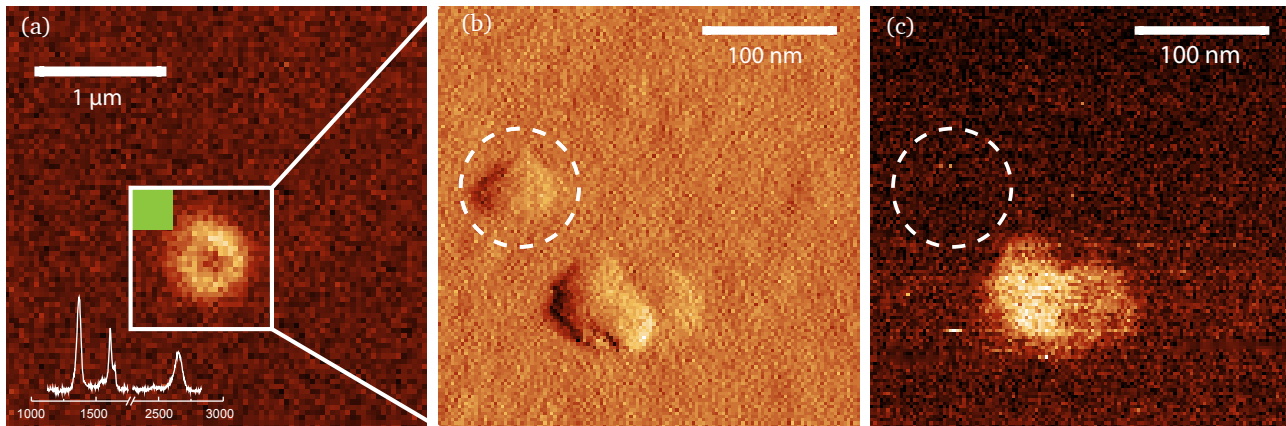
FIGURE 2.19: (a) $3.3 \times 3.3\,\mu m^2$ APD image from a sample of graphene nanoflakes acquired during a micro-Raman confocal scan with a bandpass filter for a characteristic Raman band from graphene that gets activated by the presence of disorder in the crystalline lattice (see Section 2.2.3). The Raman spectrum at the bottom right was taken at the flake inside the white square. The x-axis is in Raman shift (cm^{-1}). (b) AFM topography scan from a $320 \times 320\,nm^2$ area located inside the white square in (a). The green solid square represents the actual scan area size. (c) TERS image based on the intensity of an specific graphene Raman band (2D band, see Section 2.2.3) acquired simultaneously with the (b). The white dashed circle is marking the same location where in (b) a non-graphitic contamination is clearly visible.

micro-Raman setups, both commercially available as well as custom assembled ones, such as the one used in this work (see Section 3.1).

As an example of the advantages brought forward by TERS, consider Figure 2.19 which shows the exploration of a sample containing graphene nanoflakes by using TERS (see Section 3.3 and Section 4.3). Figure 2.19(a) shows a confocal APD image taken from a $3.3 \times 3.3\,\mu m^2$ area. Micro-Raman spectra taken show typical graphene signature, as shown by the Raman spectrum in the bottom right of Figure 2.19(a). It is clear that, due to their small size, the structure could not be optically resolved. Figure 2.19(b) is a $320 \times 320\,nm^2$ AFM topography image acquired simultaneously with the TERS scan performed at center of the location highlighted by the white square in Figure 2.19(a). The actual scan area corresponds to the size of the green solid square. The acquired topography image reveals that in fact there are two structures underneath the blurry confocal APD image. It would be easy to assume that both elements are graphene flakes that in Figure 2.19(a) didn't get spatially resolved. However, the optical TERS image in Figure 2.19(c) clearly shows that this is not the case. The area highlighted by the white dashed circle in Figure 2.19(b) should also appear in Figure 2.19(c) if both had similar spectral signature, which proves that the structure at the left of the image is not graphene, being probably some unidentified contamination in the sample.

Such example reinforces the importance of near-field optical spectroscopy, specially TERS, where other available techniques capable of resolving such small features would fail. Our results obtained through TERS will be explored in Chapter 4.

2.2 GRAPHENE

The focus of this section is to discuss why graphene is the material of choice for this work and what makes Raman spectroscopy such an important graphene characterization tool.

2.2.1 STRUCTURE & PROPERTIES

Graphene is a two-dimensional sheet of carbon atoms with a thickness of a single atom. The carbon atom has six electrons in total, of which two are strongly bounded to the atomic nucleus (core electrons), having no impact in atomic bondings. Thus, four valence electrons are available to participate in chemical bondings. In monolayer graphene each carbon atom is bonded with three other neighboring atoms forming C-C σ bonds, leaving an available vertical π bond (Figure 2.20). It is from this left over bond that graphene sources its unusual electrical, thermal and, most relevant to this work, its optical properties. These π bonds is what makes Raman spectroscopy specially suitable for graphene characterization is the fact that optical transitions are resonant to any wavelength from the UV to the infrared.

Graphene is a carbon allotrope solely composed of sp^2 hybridized carbon atoms, arranged in a hexagonal, honeycomb like, crystalline structure [19], serving as the basis of every other sp^2 carbon materials. As shown in Figure 2.20, when stacked, it becomes ordinary graphite; in a rolled up form, it becomes a carbon nanotube [136–138]; folded in a ball-like shape, it becomes a nanometric sphere known as a fullerene [139]. Figure 2.21 shows the Raman spectra from various sp^2 hybridized carbon materials, from the perfect crystallyne monolayer graphene at the top, to the disordered amorphous carbon at the bottom. As expected, even though these materials are solely composed of carbon atoms, the way these atoms are bounded give rise to distinct Raman spectra.

Monolayer graphene contains two carbon atoms in its unit cell, deemed A and B (Figure 2.22(a)). When two graphene sheets are stacked, they form a bilayer graphene with either AA or AB stacking, where the most common configuration is the AB stacking, also called Bernal stacking [140] (Figure 2.22(b)). In AB stacking, one of the layers is shifted from the other in such a way that every other atom from one layer has its projection casted on the geometrical center of the hexagons formed by the atoms in the subsequent layer.

graphite

graphene

nanotube

fullerene
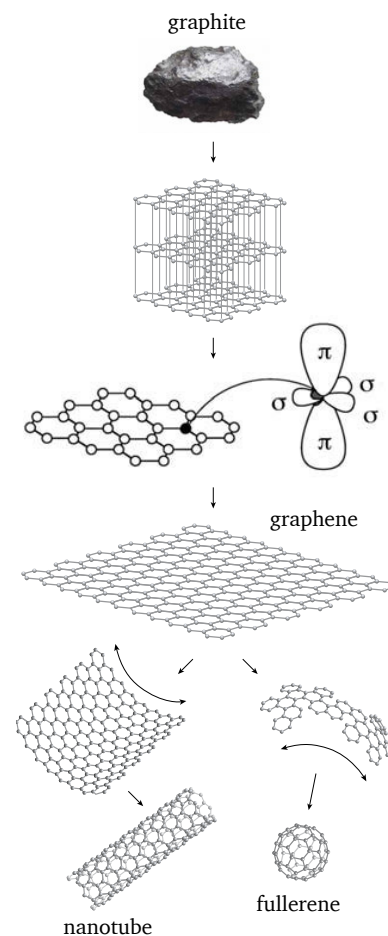
FIGURE 2.20: Depiction of various sp^2 nanocarbons. From top to bottom: a picture of a lump of graphite and an illustration showing that it is composed solely of sheets of carbon atoms connected in a honeycomb like lattice. The representation of a monolayer graphene highlights a carbon atom and shows its three in-plane C-C σ bonds and the out of plane π orbitals. Following is an illustration showing how a graphene sheet in a rolled up form becomes a carbon nanotube and when folded in a ball-like shape, it becomes a fullerene (adapted from [134, 135]).

FIGURE 2.21: Raman spectra from an assortment of sp^2 hybridized carbon materials. From top to bottom: graphene, highly-ordered pyrolitic graphite (HOPG), single-walled carbon nanotube (SWNT), damaged graphene, single-walled carbon nanohorn and amorphous carbon (adapted from [92]).
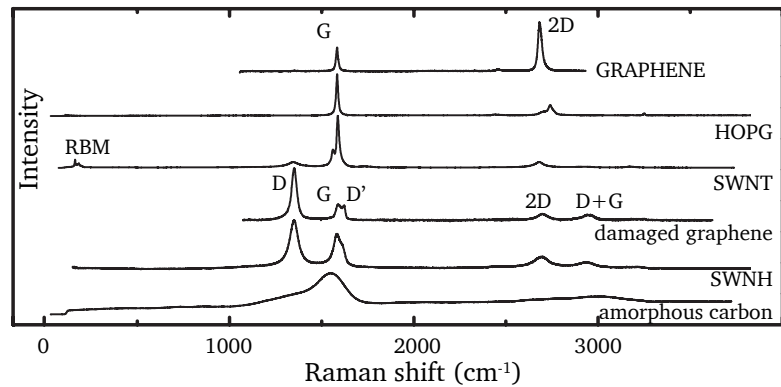
Graphene's existence has been speculated for decades, but it was only in 2004 that it was unquestionably isolated and characterized by a team of researchers from the University of Manchester, led by Russian-born physicists Andre Geim and Konstantin Novoselov. Their work, titled "Electric field effect in atomically thin carbon films" [141] earned the 2010 Nobel Prize in Physics.
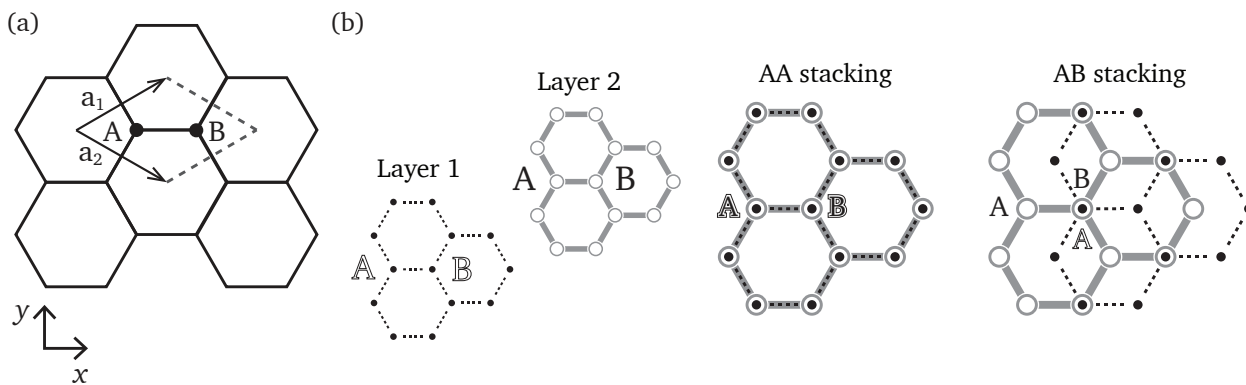
FIGURE 2.22: (a) monolayer graphene's unit cell with the atoms A and B and unit vectors a_1 and a_2 highlighted. (b) Illustration showing the formation of a bilayer graphene with AA and AB stacking, respectively.

Since its discovery, graphene has been seen as a promise in the field of nanotechnology. Considered to possess "*the perfect atomic lattice*" [135], graphene is 350 000 times thinner than a sheet of paper [142], it is optically transparent, with a transmittance of ∼98 % [143] and when it comes to the field of electronics, it has a mobility 100 times greater than silicon, reaching numbers as high as 10^5cm^2/V [144], thermal conductivity comparable to diamond and 10 times greater than copper — around 30 to 50 W cm^{-1} K^{-1}, while copper is limited 4 W cm^{-1} K^{-1} [145], it is extremely flexible, but at the same time stronger than steel, presenting a Young's modulus of 1 TPa [146], while steel is ∼200 GPa. In addition, graphene supports very high current densities, reaching values greater than 1×10^8 A cm^{-2}, 100 times higher than that supported by copper [147].

2.2.2 SAMPLE PREPARATION & CHARACTERIZATION

From a sample preparation perspective, graphene samples are easily obtainable through simple mechanical exfoliation [148], where only a piece of adhesive tape and a chunk of graphite are needed, allowing for cheap, fast, easy and *in-loco* sample preparation. Such a preparation method is appropriate for research purposes, but unworthy for industry application, due to its lack of scalability and non-reproducibility. A more scalable and reproducible approach is the growth of graphene by chemical vapor deposition (CVD). CVD gown graphene can achieve much larger surface areas [149] than those created by simple mechanical exfoliation and with a controlled growth pattern [150]. As a side effect of the nucleation process, they also present a highly polycrystalline structure with a large number of domain boundaries [151], which has a direct and negative impact on many of graphene's properties, such as its thermal and electrical conductivity [152] and mechanical strength [153]. In Section 4.4 we provide results of using TERS with STM in the exploration of CVD grown graphene samples. It is interesting to note that while AFM is usually insensitive to the transitions from one crystalline domain to another, STM is very sensitive to grain boundaries, which are line-like defects [81, 154], or any other kind of perturbation in the crystalline structure of the material due to variations imposed by these transitions in charge transport characteristics, where, together with Raman spectroscopy, becomes an important characterization tool.

2.2.3 RAMAN SPECTROSCOPY

To our knowledge, the first Raman spectrum of graphite was acquired in 1970 as reported by Tuinstra and Koenig [155]. Since then, Raman spectroscopy has been of fundamental importance in the characterization of carbon based materials, being considered one of the most important and versatile tool available [92, 138, 140, 156–160]. Focusing on graphene, Raman spectroscopy has been successfully used to determine the number of graphene layers [91, 161], the existence, amount and type of defects [81, 82, 162–166], strain and stress [67, 69, 70, 167–170] and doping levels [74, 171–173]. All this information must be extracted from the Raman spectrum acquired during each measurement and analyzed. In this sense, spectral features such as the frequency ω of a Raman band, its shape, width Γ, intensity I, usually studied in relation to other bands, can be used to characterize a graphene sample [92].

FIGURE 2.23: Raman spectrum taken from a highly defective graphene sample, which can be infered from the magnitude of the D band, highlighted in blue. Highlighted in orange and purple is the G band and 2D band respectively. Inside the circles is represented the graphene's hexagonal lattice. At each band, the red arrows point in the direction associated with the vibration. The D' band and D+G band, which are associated to disorder as well, are also visible. The excitation wavelength was a 632.8 nm from a HeNe laser.
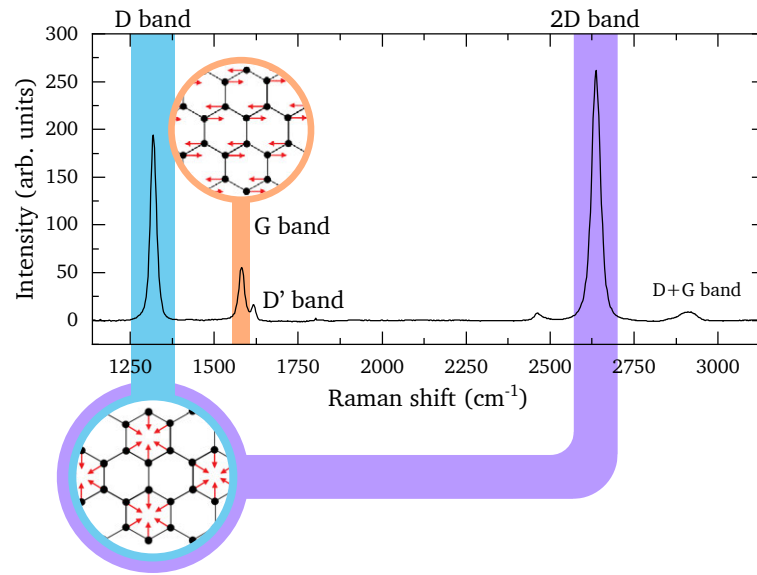
Monolayer graphene, with a pristine two-dimensional crystalline lattice, has two prominent Raman bands: the G band and the 2D band, also known in the literature as G' band (read as "g-prime band"). The G band originates from a first-order (one phonon) Raman scattering process, involving a phonon associated with the C-C bond stretching that happens in the hexagonal plane, and it is present in every sp^2 hybridized carbon system. Being located at $\approx 1580\,cm^{-1}$, the G band is considered a relatively high frequency band when compared to the vibrational modes of other materials. This fact can be explained by the small atomic mass of carbon atoms associated to the high strength of the C-C σ bond. Such high frequency has the positive consequence that small variations in the G band's frequency ω_G can be easily measured [92].

The 2D band, on the other hand, originates as an overtone involving two-phonons (second-order Raman scattering process). A similar effect, with scattering moderated by one phonon and one defect, gives rise to the lower frequency D band. The D band is only activated in the presence of disorder (defect) in the crystalline lattice, when the symmetry is broken. Apart from the needed existence of a defect, both D and 2D bands originate from the same in-plane breathing like vibrational motion of the carbon atoms. Due to their second-order origin, the frequency of these bands is dispersive[9] while the G band is non-dispersive. Under a 532 nm wavelength excitation, the D band and 2D band present a Raman shift of $\approx 1350\,cm^{-1}$ and $\approx 2690\,cm^{-1}$, respectively [158].

Figure 2.23 shows the characteristic Raman spectral signature of a highly defective graphene sample, which can be asserted based

[9]Varying frequency with the excitation wavelength.

on the presence of an intense D band and other disorder associated bands, named D' band and D+G band [174]. The blue bar highlights the D band and inside the circle is depicted the breathing like motion of carbon the atoms, which is responsible for the D band and 2D band modes. The 2D band is highlighted in purple. The orange bar highlights the G band and the illustration inside the white circle depicts the C-C bond stretching motion. When the atoms move in the vibrational modes, they distort the crystal lattice. The D and 2D modes keep the hexagonal symmetry, and for this reason they are called totally symmetric mode. In group theory the mode symmetries are classified, the G band being named E_{2g} mode and the D (or 2D) band being named A_{1g} mode in hexagonal systems like graphene [92, 175].

AB-stacked bilayer graphene's unit cell contains four carbon atoms and, due to additional forces involved in the layer coupling process, an incremental addition of layers has a direct impact in the Raman spectrum, specially in the 2D band, which will present an increase in its full width at half maximum (FWHM or Γ_{2D}) due to the activation of additional modes that, combined, cause a widening of the peak. The shape shifting of the 2D band allows, for example, the characterization of the number of layers contained in a graphene sample (see Figure 2.6(c)) [91].

▶ STRAIN & DOPING

Raman spectroscopy is also an important tool to investigate strain and doping in graphene systems. The frequency ω_G of the G band and ω_{2D} of the 2D band, from monolayer to multilayer graphene, are very sensitive to strain, being used to investigate and quantify the phenomenon through a frequency redshift [176, 177]. Based on the measured frequency shift of the G and 2D Raman band ($\Delta\omega_G, \Delta\omega_{2D}$), the magnitude of the strain can be derived, where the greater the redshift, the greater the strain. The problem with this approach is that charge doping, usually caused by the graphene's interaction with the substrate, might interfere with these vibrational modes, thus affecting the outcome of an analysis. In 2012 Lee *et al.* devised a method, based on a correlation between the frequencies of the G and 2D bands (ω_G, ω_{2D}), to optically separate strain from charge doping in graphene [69]. Shown in Figure 2.24 is Lee *et al.*'s correlation diagram where a given point P(ω_G, ω_{2D}) can be decomposed as a linear combination of unit vectors (e_T, e_H), where e_T corresponds to tensile(+e_T) or compressive strain(-e_T) and e_H corresponds to hole

FIGURE 2.24: Plot correlating the frequencies from the G and 2D Raman modes (ω_G, ω_{2D}) from which the amount of strain and doping can be derived. Given a point $P(\omega_G, \omega_{2D})$, the vector OP formed can be decomposed along the unit vectors (e_T, e_H), where e_T corresponds to tensile($+e_T$) or compressive strain($-e_T$) and e_H corresponds to hole doping, as shown in the inset at the lower right corner (adapted from [69]).
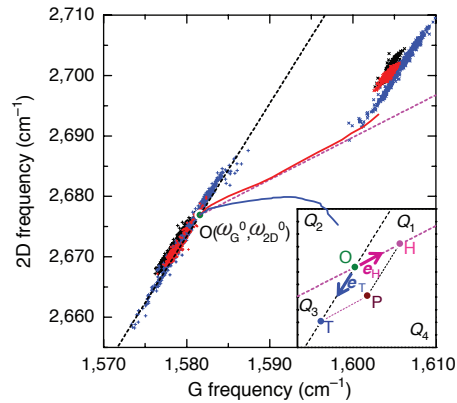
doping. Based on the contribuitions from each of these vectors, one can quantify the amount of strain and doping in a given graphene sample.

In Section 4.1 we present results where the method to separate strain from doping as proposed by [69] was applied, while in Section 4.5 we present results of tip-induced strain on suspended graphene where such method is also used (see Figure 4.12(f)).

▸ DEFECTS

Specially important is the Raman response in graphene due to the presence of defects in the crystalline lattice. Disorder has a significant impact on graphene's properties and therefore must be well understood and characterized. From a geometrical approach, defects in graphene, due to its two-dimensional nature, can be either point-like (0D) or line-like (1D). (Figure 2.25(a)) shows a diagram with amorphization routes for sp^2 carbons, through which it is possible to separate point-like defects from line-like defects [81]. As reported, 0D defects arise from the existence of dopants, vacancies or functional chemical groups. Its characterization is made through the average distance between the nearest defects (L_D), as shown pictorially in Figure 2.25(b). On the other hand, 1D defects originate from the existence of crystallographic edges or atomic dislocations of the material's crystalline structure, being characterized, geometrically, by the average distance of the centroids of the crystallites formed by the enclosing edges (L_a), as shown in Figure 2.25(c). The proposed diagram shows the ratio of the areas taken from the graphene D and G bands, named A_D/A_G ratio, as a function of Γ_G. Through this diagram it is possible to classify, from a topological standpoint, the quality of any sp^2 carbon, from perfect to completely disordered (amorphous carbon), being an important tool not only in the study of the effects

FIGURE 2.25: (a) Amorphization routes for sp^2 carbon materials with $(A_D/A_G)E_L^4$ as function of Γ_G, where E_L^4 is the laser power to the 4th power. Illustrations showing graphene samples consisting purely of (b) point defects and (c) line defects, where L_D is the average distance between the nearest point defects and L_a is the average crystallite size. (d) Raman spectra from samples following the pure point defect route. (e) Raman spectra from samples following the pure line defect route. Each spectrum in (d, e) has a corresponding green circle in (a) (adapted from [81]).

these defects have on materials, but also as quality monitoring tool, for example in a manufacturing processes that has graphitic materials as a base component.

The Raman data utilized to generate the given diagram was solely based on spectra acquired by micro-Raman, with no near-field information. In Section 4.3 we build upon Cançado's *et al.* work [81] by introducing measurements done in the near-field regime as well as in the far-field showing that, due to interference and field confinement effects, the results differ when comparing both techniques. From a metrological point of view, results obtained from diffraction limited techniques must be carefully analyzed, specially when dealing with nanometric sized structures.

2.3   TERS ENHANCEMENT FACTOR & SPATIAL COHERENCE

Raman scattering has historically been regarded as a spatially incoherent process [36, 178, 179], which means that light scattered from distinct sample locations get summed up incoherently and, as a consequence, the intensity of the scattered signal in the far-field, I_{FF}, is proportional to the scatterer volume, V, and given by

$$I_{FF} \propto V|\hat{\epsilon} \cdot \alpha \mathbf{E}|^2 \,, \tag{2.12}$$

where $\hat{\epsilon}$ is the unit vector that defines the scattering polarization direction, being α and $\mathbf{E}$, as previously defined in Section 2.1.2, the polarizability of the medium and the strength of the incident electric field, respectively.

In the context of TERS, the concept of a numerical value known as enhancement factor, f_e, is commonly found in the literature as a way to characterize a TERS tip based on the enhancement exerted on the Raman signal [55, 180, 181], being the enhancement factor commonly defined as the ratio between the near-field and the far-field intensities per unit volume [180]. In a 2D-system it is given by [181]

$$f_e = \frac{I_{NF} - I_{FF}}{I_{FF}} \frac{r_{focus}^2}{r_{tip}^2} \,, \tag{2.13}$$

where I_{NF} and I_{FF} correspond to the intensity of the Raman signal with and without the presence of the tip, respectively. r_{focus} and r_{tip} are the radius of the laser spot and the tip's apex radius, respectively. It is easy to see from Eq. (2.13) that even small variations in the laser spot size will make the calculated f_e to change, even for the same tip, thus being an arbitrary way of calculating f_e.

Eq. (2.13) [36] is, however, an oversimplification of the TERS enhancement factor. It has been shown that the TERS enhancement actually involves the concept of correlation, which is intrinsic to crystal excitations, such as phonons. The phonon correlation length, L_c, is typically an order of magnitude smaller than the wavelength of the visible light, therefore being inaccessible in the far-field regime, and Eq. (2.12) remains valid. However, L_c is accessible in the near-field regime and, depending on the symmetry of the vibration mode, the intensity of the scattered field can be affected by constructive or destructive interference.

In order to experimentally show how interference effects impact the intensity of the Raman signal, a tip-approach procedure can

be performed. In such procedure, a tip interacting with the sample surface is progressively retracted, while a Raman spectrum is acquired at each step. With the Raman spectra acquired, the intensity of Raman bands under scrutiny can be plotted as a function of the tip/sample separation with the distance at each step, ΔZ, being given by

$$\Delta Z = Z_0 + \sum_{i=0}^{t} d_i \; , \qquad (2.14)$$

where Z_0 is the initial tip/sample separation distance (usually given by set point adjustment, as explained in Section 2.1.3), d_i corresponds to a constant distance covered by each step and t is the total number of steps. Figure 2.26 show a graphical representation of a tip-approach procedure.
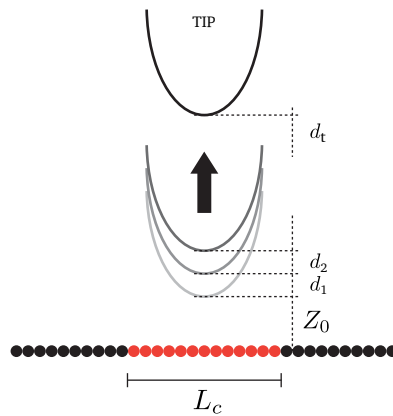
FIGURE 2.26: Illustration of a tip-approach procedure with its relevant parameters as given by Eq. (2.14). The small solid circles represent the sample. Light scattered from a region smaller than the correlation length L_c, represented by the red circles, are subjected to interference (adapted from [182]).

Figure 2.27 shows two plots from the same tip-approach procedure taken at the border of a pristine graphene flake.[10] Note that the horizontal axis corresponds to ΔZ as given by Eq. (2.14). In Figure 2.27(a) the absolute intensity of the Raman bands is plotted, while in Figure 2.27(b) the intensity from each band has been normalized by the initial intensity found in Figure 2.27(a). Figure 2.27(b) shows not only a decrease in the intensity of the Raman bands as a function of the increasing tip/sample distance, but it also shows that each Raman band has a different intensity variation as a function of distance. It is important to note that even though the D and 2D bands have the same vibrational symmetry, the fact that the intensity of the D band drops more sharply is due to the fact that, being a pristine graphene sample, the disorder is located only in a very narrow region at the border, which behaves as a 1D scatterer, thus is more affected by the tip/sample distance variation [119]. Also note that, when the tip is further away from the sample, the intensity from all the bands converge to a common value, which corresponds solely to the far-field contribution.

[10] As explained in Section 2.2, the D band is activated by a disorder in the crystalline lattice, for this reason it is present at the border of a pristine graphene, thus in order to have the D band present in the tip-approach, this region was chosen.

FIGURE 2.27: Plots showing the intensity of the Raman D, G and 2D bands as a function of the tip/sample separation distance. The black triangles, blue circles and red squares represent the intensity of the D, G and 2D bands, respectively, as acquired experimentally. (a) Intensity from each band as acquired experimentally. (b) Normalized intensity from (a) for both the most intense (set to 1) and less intense (set to zero) measurement. In (a) and (b) the solid curves beneath the scattered points represent the fitted theoretical curves as described in [35], from which f_e and L_c have been derived (adapted from [36]).
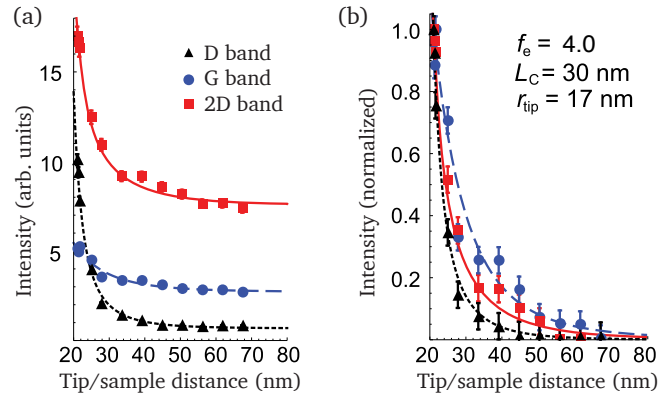
In a companion work [35], it was proposed a model that can be used to infer a realistic tip enhancement factor, f_e, as well as a way to find the correlation length, L_c, given that the tip's apex dimensions, the tip/sample distance separation, Z_0, and the intensity of the acquired spectra at each point, are provided.

Ref. [35] also shows that it is relevant to consider the possible ways in which the incident field can interact with the tip/sample system, since such interactions can be constructive or destructive, thus impacting the intensity reaching the detector. Such interactions can be represented by the following series: S, TS, ST and TST, where S (sample) represents the incident field interacting with the sample; TS (tip/sample) represents the incident field scattering at the sample and then at the tip, respectively; ST (sample/tip) represents the incident field scattering at the tip and then at the sample; TST (tip/sample/tip) represents the incident field scattering at the tip, then sample and then the tip, respectively. Since S does not interact with the tip, it will not be considered. The following table (Table 2.1), derived from [35], details the interference effects suffered based on each interaction mode:

Table 2.1: TS, ST and TST interactions for the G and 2D bands, where C, D and N stand for constructive interference, destructive interference and no interference, respectively.
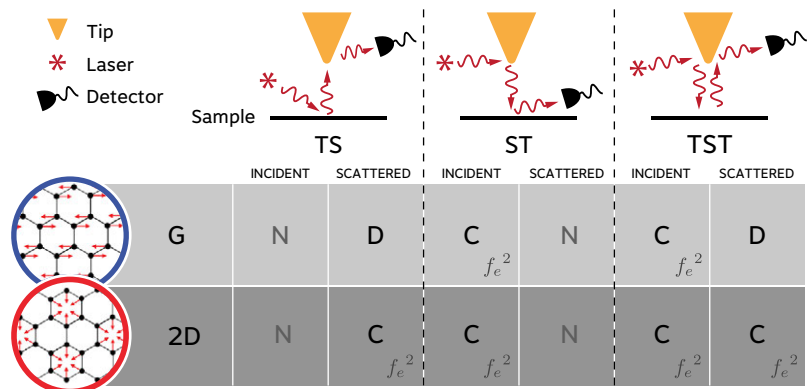
Considering that at each constructive interaction f_e has a quadratic effect on the intensity of the signal reaching the detector, the intensity of the G band is given by

$$I_\text{G} = \alpha f_e^{\,2},$$

(2.15)

while the intensity of the 2D band is given by

$$I_\text{2D} = \gamma f_e^{\,4} + \delta f_e^{\,2}.$$

(2.16)

Eq. (2.15) and Eq. (2.16) will be further explored in Section 4.3.

Recently the relevance of TERS spatial coherence was demonstrated for gallium sulfide (GaS) [183], generalizing the overall importance of this aspect to other two-dimensional systems. The concepts presented here will be further explored in the work presented in Chapter 4.

3

Technical Aspects

This chapter is divided in five sections: Section 3.1 is dedicated to the TERS system, with special emphasis in the optical part, and will discuss the improvements that were made to the previous equipment [37]. Section 3.2 is devoted to the adaptations performed in order to implement a STM based TERS system, including the development of a STM scanhead, its transimpedance preamplifier and the necessary adaptations that had to be made for STM measurements. Section 3.3 provides details on how to prepare samples containing isolated graphene, as well as sample validation procedures, including TERS measurements on such samples. Section 3.4 has the objective of introducing the highly efficient plasmon-tunable tip pyramids (PTTPs), which was used in most of the work presented here, and the reasons why it is better than other tips available. Finally, Section 3.5 will discuss the softwares that were developed in order to work with hyperspectral images and that made possible the extraction of data from hundreds of thousands of Raman spectra that were acquired.

3.1   THE TERS SYSTEM

As presented in Chapter 1, the TERS system described in this thesis was based on the previous work of many scientists, including the work of Dr. Paulo Araujo, as described in his thesis [37]. The current system, that will be described in this Section, was fully assembled during this work, but shared some components used in Araujo's work, such as: APD detector, spectrometer, nanopositioning stage and the AFM scanhead[1], therefore such topics will be left out of the discussion, and related details can be found in [37]. Another significant change was the replacement of the SPM controller from a twenty year-old model to a more modern one, with digitally integrated modules, which demanded the rewiring of the entire system and the configuration of a new controlling software. Details about this new SPM controller can be found Appendix A.

[1]The AFM scanhead went through many interactions, such as better wiring options and the replacement of electronic components that malfunctioned, became obsolete or had better alternatives available, but the basic design idea remained the same.

3.1.1   OPTICAL SYSTEM
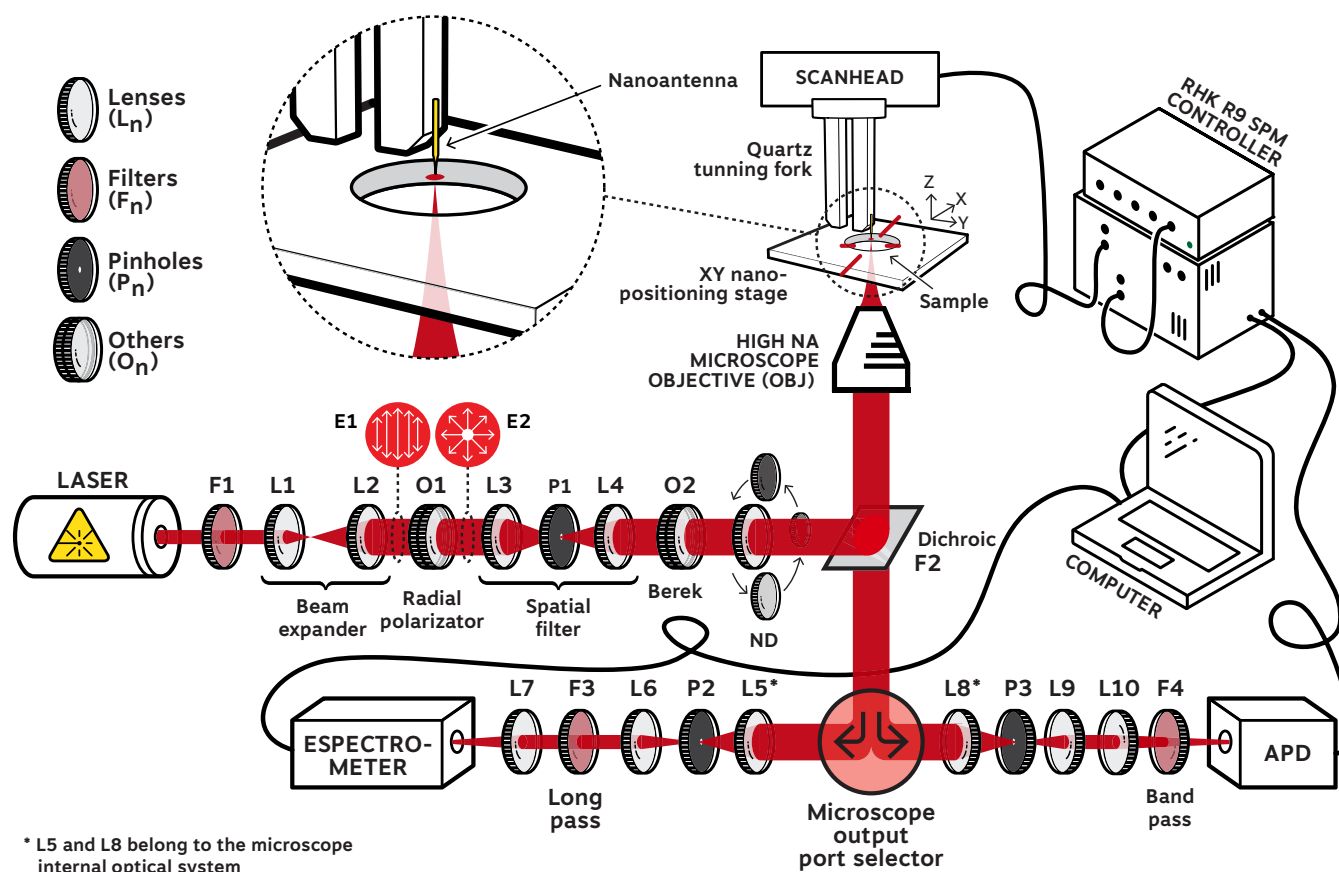
FIGURE 3.1: Schematic illustration of the described TERS system, with emphasis on the optical path. L_n represent lenses, F_n represent filter elements, P_n represents pinholes, while O_n represent other types of elements that will be properly identified in the text.

Figure 3.1 is a schematic depiction of the TERS system where the most important elements are labeled for easier referencing. Tables in Appendix B provide a list of all the components described here.

What follows is an overall description of all the optical and optome-chanical elements required for the construction of a system capable of performing optical and spectroscopic measurements and images at the micro and nanometric scale, as well as the order in which they are placed and, when applicable, their purpose. The objective here is to provide an overview of the optical alignment process in order to facilitate system reproduction.

For TERS, it is fundamental to have an aberration free and radi-ally polarized laser beam to achieve satisfactory results, therefore special care must be taken in the placement and selection of the optical components, such as the type of lenses used, focal lengths and coating characteristics. Considering the large available space on the optical table, the use of cemented achromatic doublets lens and, whenever possible, with larger focal length was the appropriate choice. Although cheaper, plano-convex lenses, specially those with a short focal length (≤ 50 mm) should be avoided. A good balance be-tween value and price can be found in the achromatic doublet lenses, which are composed of two optical elements and designed to reduce chromatic and geometric aberrations, which are frequent in single lens design and especially at shorter focal lengths. Special attention must be taken with regard to the usually provided antireflective (AR) coating. Although coated lenses have improved transmissivity, they are designed to work efficiently under a certain wavelength range. The utilization of a coated lens in the wrong range will impact the performance of the system. In our system the coating of choice is usu-ally in the 400 to 700 nm range (Figure 3.2(a)) for the lenses before the microscope and in the 650 to 1050 nm range (Figure 3.2(b)) for the lenses after the microscope. This choice is based on the fact that we are mostly interested in the Stokes Raman scattering and since our excitation is from a Helium/Neon (HeNe) laser, with a 632.8 nm wavelength, the Stokes wavelength of our samples are usually above the 700 nm recommended range, thus we use one type of coating before the sample, where the wavelength of interest is the laser, and another range after sample interaction, where the wavelength of interest is the Stokes Raman component.

The entire TERS system, with the exception of a few components,[2] is assembled on top of an optical table, which is partially covered by a metal housing(see Appendix C). The first element to be installed on the optical table, more specifically inside the metal housing, is a Nikon Eclipse Ti-U inverted optical microscope. The advantage of using this inverted geometry, as already discussed in Section 2.1.2, is that it favors the coupling of the laser spot with the scanning probe scanhead, which is placed atop, as shown in Figure 3.1. The
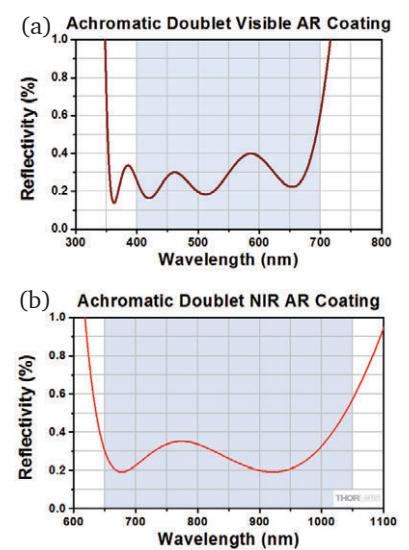
FIGURE 3.2: Plots showing the reflectivity as a function of wavelength for AR coatings. (a) Visible AR coating and (b) near-IR coating. (adapted from [184]).

[2]The only elements placed outside the op-tical table are: the computer, the SPM con-troller and the drivers for the nanopositioning stage and picomotor, which are located on a rack underneath the optical table.

inverted geometry also facilitates the usage of oil-immersion, high-NA microscope objectives. This Nikon microscope is factory equipped with three distinct output optical ports that can be chosen from a manual optical path selector knob.[3] Considering the numbering in the selector port going from 1 to 4, we have: (1) directs 100 % of the beam intensity to the optical path located orthogonally to the left of the microscope in respect to the eyepiece. This path is used to direct the beam to the spectrometer; (2) directs 100 % of the beam intensity to the eyepiece of the microscope; (3) directs 90 % of the beam intensity to the optical path located on the right of the microscope in respect to the eyepiece, while the remaining 10 % is directed to the eyepiece. This port is used to direct the beam to the APD[4]; (4) directs 90% of the beam intensity to an optical path parallel to the microscope's body and located below the eyepiece. This port has an attached camera whose acquired image is used for focusing, using the laser diffraction pattern as a reference (see Appendix C.4). In total there are three cameras in the system: one in the port described above, one in the right ocular of the eyepiece and one attached to a long distance microscope, whose image is used to assist in the tip-approach process.

[3]This port selector dial has been custom motorized to facilitate the usage of the system without requiring manual intervention(see Appendix C).

[4]The reason this port was allocated to the APD and not to the spectrometer is because an APD is a more sensitive device and used mostly for sample mapping, therefore this 10 % loss is less problematic.

OPTICAL PATH — LASER TO INVERTED MICROSCOPE

(a) INTO METAL CASE   MIRROR ●   RADIAL POLARIZER (ARCOPTIX)   COLLIMATION (F=250 mm)   LASER LINE FILTER   LASER

SPATIAL FILTER

● MIRROR   F=60 mm   PINHOLE 25 μm   F=40 mm   LASER BEAM EXPANDER (F=30 mm)   OUTSIDE METAL CASE

(b) MICROSCOPE   ● MIRROR   N.D. FILTERS   BEREK   ● MIRROR   INSIDE METAL CASE

FIGURE 3.3: Excerpt images of the optical path between the laser and the inverted microscope with the optical elements labeled. (a) shows the path outside the metal housing, while (b) shows the path inside it.

Figure 3.3 is a picture of the system from inside and outside the metal box and is provided as a reference. What follows is a step–by–step description of all the optical elements before the microscope entrance.

The laser is a linearly polarized Helium/Neon (HeNe) with a 632.8 nm wavelength. It is installed at a distance of ≈ 140 cm from the microscope, which is the minimum distance necessary to comfortably install the needed optical elements between the laser and the microscope. This distance should be kept minimal in order to reduce positional variations in the laser beam caused by factors such as vibrations, humidity and temperature variations that might cause small deviations in the laser focal position in the sample plane. Care should be taken to place the laser beam parallel to the optical table

and with its polarization perpendicular to it (i. e. vertically oriented polarization) as shown in Figure 3.5(a). This orientation is necessary for the correct operation of the radial polarizer, described later.

Following the optical path from the laser, the next element is a laser line filter (F1). Laser line filters are a special type of bandpass filter whose main purpose is to allow the transmission of only a narrow frequency range (full width at half maximum bandwidth: 2.4 nm (typical); 4 nm (maximum)), suppressing, therefore, secondary lines that might exist. Its placement distance to the laser is not relevant, as long as the laser is collimated when going through it, however it is important to follow the orientation (usually a white arrow) marked in its encapsulation.

After the laser and the microscope have been positioned and tightly held in place, the mirrors that guide the laser beam to the sample are installed. In the setup described here, four mirrors are utilized[5]. Two mirrors are located outside the metal housing (marked by blue dots on Figure 3.3(a)), whose function is to guide the beam to inside the metal housing, through a hole in the metal panel, while providing the necessary freedom to move the beam while keeping it parallel to the optical table. The other two mirrors form an assembly known as *periscope* (marked by red dots on Figure 3.3(b)), whose purpose is to elevate the laser beam up to the rear optical entrance of the microscope, while providing the necessary freedom to precisely align the beam. Once inside the microscope, the beam should hit the center of the dichroic mirror, which will reflect the laser in a 90° angle towards the microscope objective. Any angulation when entering the microscope, may cause the beam to deform as it enters the microscope objective, thus resulting in image degradation, as well interfere with the polarization. One way to assert that the laser beam is correctly aligned is to place a piece of mirror acting as a sample. If the incident laser beam is properly focused, its back-reflection must be collimated. Moreover, by looking through the eyepiece, making sure that the laser power is sufficiently low as not to cause any eye injury, one can be sure the laser is properly aligned. Inside the left eyepiece ocular, there is a transparent target with a marked cross. This cross pinpoints the center of the microscope's optical path and therefore it is where the laser should hit (Figure 3.4). This can be accomplished through the adjustment of both mirrors of the periscope. To check if there is any angulation in the beam, the user should rotate the microscope's focus adjustment knob, which acts by moving the microscope objective up and down, while looking through the eyepiece. The laser spot, as seen through the eyepiece should look perfectly circular. If by moving the

[5]The mirrors are not represented in Figure 3.1, due to the fact that they are only used to facilitate the alignment, even though they are labeled in Figure 3.3. It is important to note that a minimum of two mirrors is necessary to properly direct a laser beam while keeping it parallel to the optical table.
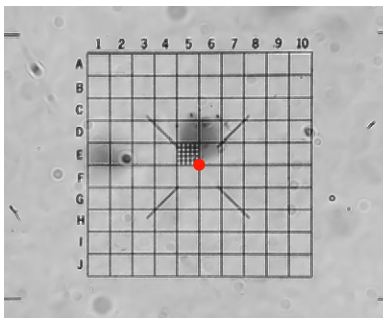
FIGURE 3.4: Target marker as seen through the eyepiece of the microscope. The marker is located inside the left eyepiece. The red dot, which has been placed here as a reference (it is not actually the laser), highlights the center where the laser should be.

focus, the laser spot becomes an ellipse, moves off center or presents a comma like shape, it means that the beam is not properly aligned and should be fixed.

If the system in question was only to be used for micro-Raman spectroscopy, it would be safe to say that, after this alignment, the excitation path was complete[6]. However, for TERS based on the backscattering configuration, the laser needs to be radially polarized [30], therefore, additional optical elements are necessary to fulfill the desired conditions.

The idea of first positioning the optical microscope, followed by the laser and mirrors, is to facilitate the placement of the other optical components. Every time a new component is placed, the laser focal point position is checked to see if any large change in position occurred, being the newly placed component adjusted until the focal point is back to the desired position.

The first elements to be placed after this initial alignment are two achromatic doublet lenses, the first one (L1, $f_{L1} = 30\,\text{mm}$), whose purpose is to expand the laser beam and the second one (L2, $f_{L2} = 250\,\text{mm}$) to recollimate the expanded laser beam. Knowing that the beam coming out of the laser has diameter of $\text{ø}_{\text{laser}} \approx 700\,\mu\text{m}$ (as per manufacturer's datasheet), after these lenses, the collimated beam will have a diameter of $\text{ø}_{\text{beam}} \approx 6\,\text{mm}$ given by

$$\text{ø}_{\text{beam}} = \text{ø}_{\text{laser}} \frac{f_{L2}}{f_{L1}}$$

$$\text{ø}_{\text{beam}} = 0.7\frac{250}{30} = 5.8\,\text{mm}\,, \qquad (3.1)$$

which is sufficient to cover a large area of the optical window of the next element (O1), a radial polarization converter. Such an expanded beam facilitates the alignment and configuration of this device.

The radial-polarization converter (Figure 3.5(b,c)) converts the linearly polarized laser beam to a radially polarized beam, which is essential for the correct coupling between the laser and the nanoantenna, improving the mechanism responsible for the enhancement of the local electrical field [50, 185]. It is important to note that for this component to work correctly, the laser must enter its optical window with its polarization vertically aligned. The alignment procedure of this element requires extreme care and the steps needed to accomplish it are throughly documented in the product manual, being outside the scope of this work to reproduce this information.

Following we have three elements which, together, form a spatial filter: two achromatic doublet lenses with a pinhole located at

[6]Although this could be considered a fully working excitation configuration, depending on the diameter of back aperture of the microscope objective, an incompatible laser beam width would result in an Airy disk far from optimal, resulting in spatial resolution loss or unnecessary cropping of the beam
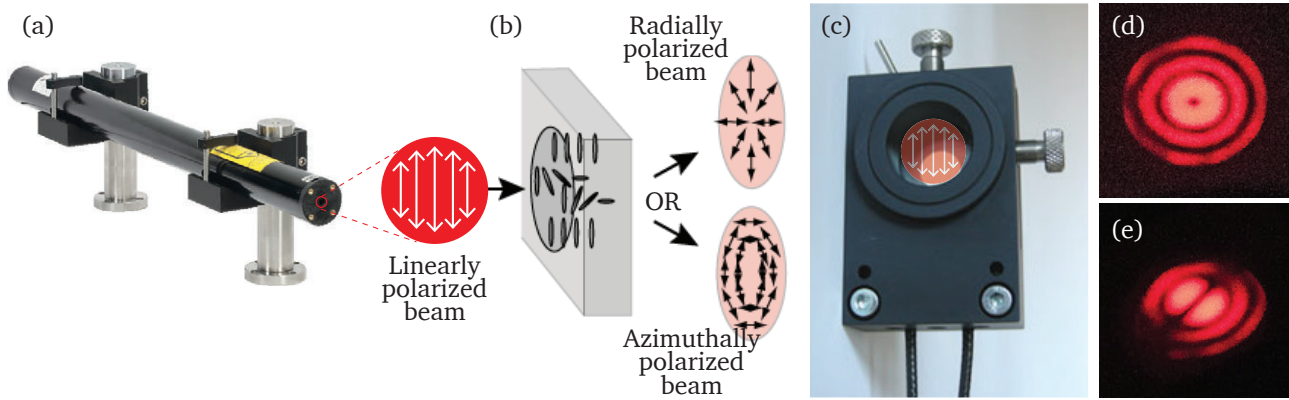
FIGURE 3.5: (a) Illustration of the HeNe laser showing how the linear polarization must be oriented with regard to its fixing. (b) Illustration depicting the polarization converter and its possible outcomes: radial or azimuthal polarization. (c) Actual photograph of the Arcoptix radial-polarization converter. (d) Profile image of a radially polarized beam on a piece of paper. (e) Same as (d), however after passing through a linear polarizer, which blocks all the components in the direction that the linear polarizer was placed, while allowing the other components to go through. (a) is adapted from [186], (b, c) are adapted from [187].

the focal point of both lenses. The first lens (L3, $f_{L3} = 40\,\mathrm{mm}$) is responsible for focusing the beam into a pinhole (P1, $\varnothing_{P1} = 25\,\mu\mathrm{m}$). The use of this pinhole, positioned near the focal plane of this first lens, is to allow the transmission of the transverse mode of the radial polarization, eliminating higher order modes that might be present in the laser beam, therefore only the central peak of of the diffraction pattern is transmitted. Other patterns that might be produced by particles in the air or on the lenses previous to the spatial filter, are also attenuated.

The second lens of the spatial filter (L4, $f_{L4} = 60\,\mathrm{mm}$) is chosen based on the desired diameter of the collimated output beam. To achieve the nominal excitation numerical aperture of the microscope objective, thus achieving the highest spatial resolution possible with the provided NA, the beam diameter must match the diameter of the objective's back aperture. The oil immersion microscope objective used in the system has a back aperture diameter of $\varnothing_{obj} \approx 9.5\,\mathrm{mm}$, therefore we need an additional diameter increase of 1.5× when compared to the beam diameter after (L2), and, for this reason, (L4) has a focal length $f_{LA} = 60\,\mathrm{mm}$. Figure 3.5(d) is a photograph of the laser beam after (L4), projected on a piece of paper.

After (L4), the beam is then directed by the two dielectric mirrors previously placed, to the interior of the metal housing, where microscope and photodetectors are located. The next element to be placed is a filter wheel (ND1) with six positions; five of them contain absorptive neutral density filters that are used to adjust the intensity of the laser that reaches the sample. One of the positions is left empty, so the laser can go through, without any attenuation. The filter wheel has been custom motorized and can be remotely activated (see Appendix C.3).

FIGURE 3.6: (a) Photograph of the inverted microscope fitted with the steel base and before the motorization improvements. (b) Close-up photograph of the nanopositioning stage fixed inside the steel base and with the steel plate and sample holder attached. Through the glass coverslip it is possible to see the microscope objective frontal lens. (c) Exploded illustration showing the steel base as well as all the elements that sit on top of it (3D model assembled with the help of Vitor Monken).

The next element is a polarization compensator (O2). After getting converted from linear to radially polarized, the beam will get transmitted and reflected by several optical elements before reaching the sample. At each interaction with these elements, small phase changes occur causing a distortion in the polarization. Known as *Berek*, this optical device is capable of correcting the laser polarization in order to compensate for phase aberrations that are commonly introduced during the path of the laser to the sample, which guarantees that the correctly polarized laser will reach the sample.

The laser beam then reaches the inverted optical microscope. Figure 3.6 shows the inverted microscope as well as an exploded detail view of how the sample/nanopositioning stage/objective are coupled together. Once inside the microscope, the laser beam gets reflected by a dichroic beamsplitter (F2) into the back aperture of the microscope objective (OBJ), which will focus the laser on the sample plane. At this moment it is important to assess the quality of the radial polarization that is hitting the sample. This can be done by

placing a linear polarizer $\approx 1\,\text{cm}$ above where the sample should be. By visual inspection, the pattern projected on the polarizer should be similar to that shown in Figure 3.5(e). If that is not the case, the Berek should be adjusted to compensate the aberrations that have been introduced. Details on how to use the Berek is outside the scope of this work. The topic Radial Polarization Validation in Section 3.1.1, provides an experimental procedure to assess if the polarization at the sample plane is appropriate.

After getting focused on the sample, the backscattered light is collected by the same microscope objective and follows the inverse path. However this time the inelastically scattered light gets transmitted through (F2), while the elastic scattered light is reflected back in the direction of the laser source, with only a small leakage getting transmitted. The Raman signal is then directed to one of the available optical paths of the microscope, based on the position of the selector knob.

OPTICAL PATH — MICROSCOPE TO SPECTROMETER
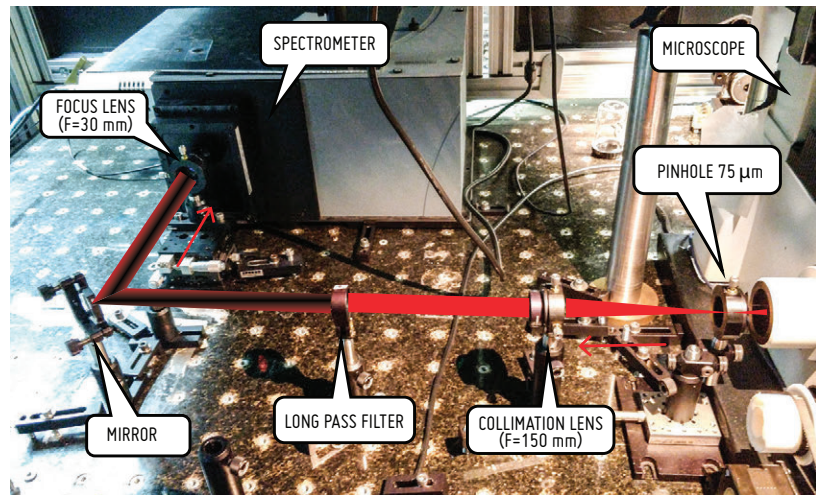
FIGURE 3.7: Photograph of the optical path between the microscope and the spectrometer with the optical elements labeled.

With the port selector set to "Spectrometer", the scattered light gets focused by a 200 mm lens located inside the microscope (L5), into a pinhole (P2, $\text{\o}_{\text{P2}} = 75\,\mu\text{m}$) which improves system confocality. The beam then travels through an achromatic doublet lens (L6, $f_{\text{L6}} = 150\,\text{mm}$) and is collimated to a diameter of $\text{\o}_{\text{beam}} \approx 7\,\text{mm}$, given by

$$\text{\o}_{\text{beam}} = \text{\o}_{\text{obj}} \frac{f_{\text{L6}}}{f_{\text{L5}}}$$

$$\text{\o}_{\text{beam}} = 9.5 \frac{150}{200} = 7.125\,\text{mm}. \tag{3.2}$$

The collimated beam will get transmitted by a long-pass filter, responsible for attenuating even further any Rayleigh scattered light

left over, and allowing to pass light with lower frequencies. The beam is then focused by yet another achromatic doublet lens (L7, $f_{L7} = 30\,\text{mm}$) into the spectrometer. Given that the spectrometer has a f-number, $F_\# = 4$, as provided by the manufacturer, and the beam diameter, as calculated in Section 3.1.1, is $\varnothing_{\text{beam}} = 7.125\,\text{mm}$, L7 must have, in order to match the spectrometer's f-number, a focal length $f_{L7} \approx 30\,\text{mm}$, which is calculated by

$$f_{L7} = F_\# \times \varnothing_{\text{beam}}$$
$$f_{L7} = 4 \times 7.125\,\text{mm} \tag{3.3}$$
$$f_{L7} = 28.5\,\text{mm} \approx 30\,\text{mm}.$$

This lens is placed on a XYZ stage (where Z corresponds to the beam direction of propagation), which allows for a more precise focusing of the beam through the slit of the spectrometer. This slit is motorized and usually kept, during regular operation, with an opening width of $30\,\mu\text{m}$. If the beam is properly focused on the entrance plane, no noticeable change is observed when opening it from 30 to $200\,\mu\text{m}$, except an increase in the background signal. During the initial alignment of the spectrometer, the slit is usually kept with a width of $200\,\mu\text{m}$.

OPTICAL PATH — MICROSCOPE TO APD
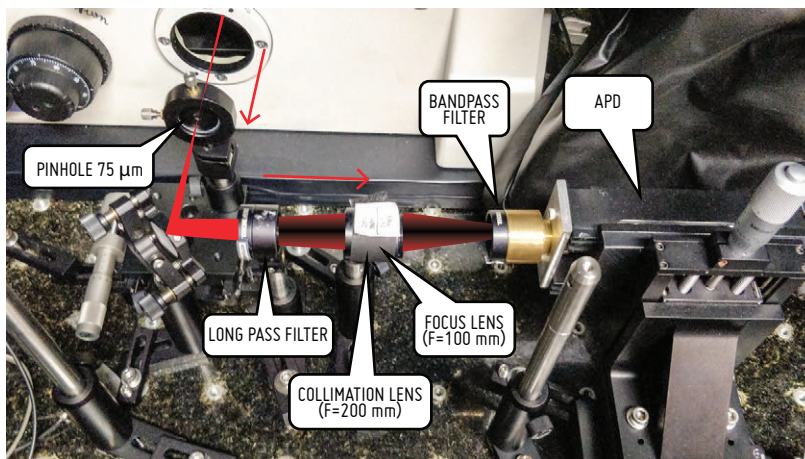
FIGURE 3.8: Photograph of the optical path between the microscope and the APD with the optical elements labeled.

Another option is to send the scattered signal from the microscope to the APD, which is possible by appropriately changing the microscope port selector. The optical elements on this path have the same purpose and are placed in the same order as those on the path to the spectrometer, although the pinhole and lenses have size and focal length to match the requirements for imaging with an APD. The pinhole (P3) has an orifice size of $75\,\mu\text{m}$ and is placed on a flip mount. This is necessary to facilitate a realignment of the APD, if needed. The achromatic doublet lenses (L9) and (L10) have focal

FIGURE 3.9: (a) Nile Blue molecules as imaged by a radially polarized excitation beam. (b) Illustration matching the orientation of the molecules in (a). (c) APD image from a Nile Blue sample acquired with our system. ((a) and (b) are adapted from [50])
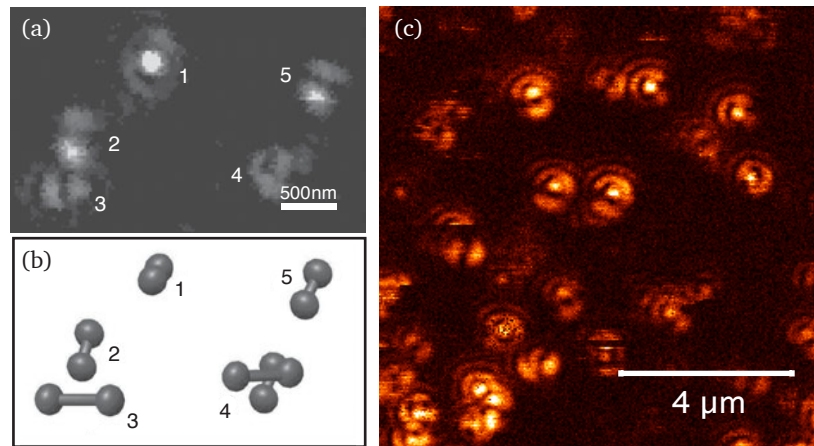
lengths of 200 mm and 100 mm, respectively. The only distinguishing element, when comparing to the path going from the microscope to the spectrometer, is the presence of a band-pass filter (F4), responsible for selecting a specific Raman spectral band, as explained in Section 2.1.2.

The APD has an active sensor area diameter of $\emptyset_{\text{APD}} = 175\,\mu\text{m}$, according to the manufacturer, and is placed on a XYZ stage, necessary for precise positioning and focusing in regard to the optical path.

RADIAL POLARIZATION VALIDATION

As already pointed, correct radial polarization at the sample plane is crucial to the coupling between the laser and the nanoantenna [50, 185]. In order to assess the quality of the polarization at the sample plane, as well as a way to obtain the PSF of the system, a sample containing sparse Nile Blue molecules is used. Nile Blue [188] is a dye molecule with an absorption peak at $\lambda_{\text{abs}} \approx 630\,\text{nm}$, equivalent to excitation from a HeNe laser line, and emission at $\lambda_{\text{emission}} \approx 660\,\text{nm}$, far enough from the absorption and therefore easy to detect. Nile Blue has an interesting characteristic of behaving as a dipole, reaching maximum emission when oriented with the polarization of the excitation field [50].

With a properly prepared sample, individual molecules are easily isolated, acting like an impulse, and due to their random orientation at the sample plane, combined with the strong polarization of the laser in the z-axis, one is able to assess the local field distribution as a function of the molecule's orientation [189]. Molecules vertically aligned with respect to the sample plane are only sensitive to the vertical component of the electric field, appearing as symmetric circles (Figure 3.9), thus if the laser spot at the sample plane is not properly polarized, those molecules perpendicular to the sample plane will not

be visible in the raster scanned image. The absence of such features is a warning sign that the polarization is not properly configured. Such a sample can also be used to assess the spatial resolution of the microscopy system, as discussed in [190].

3.1.2   SPM SYSTEM

In the system described here, as shown in Figure 3.1, the SPM scanhead sits on the top of the sample, while the laser shines from below. The scanning is done by moving the sample, while laser and nanoantenna stay fixed in place. This configuration is based on the requirement that the laser and nanoantenna must be optically aligned during the experiment. As the sample is moved underneath the tip, the feedback system must act on the tip's vertical position in order to match the configured set point specified by the user (see Section 2.1.3). Such configuration makes it possible to carry out spectroscopy measurements (confocal and near-field) in addition to SPM and nanomanipulation measurements using the same probe. Ref. [37] provides details regarding the AFM scanhead used. Details on the STM scanhead are provided in the next Section (Section 3.2).

3.2 INSTRUMENTATION FOR STM
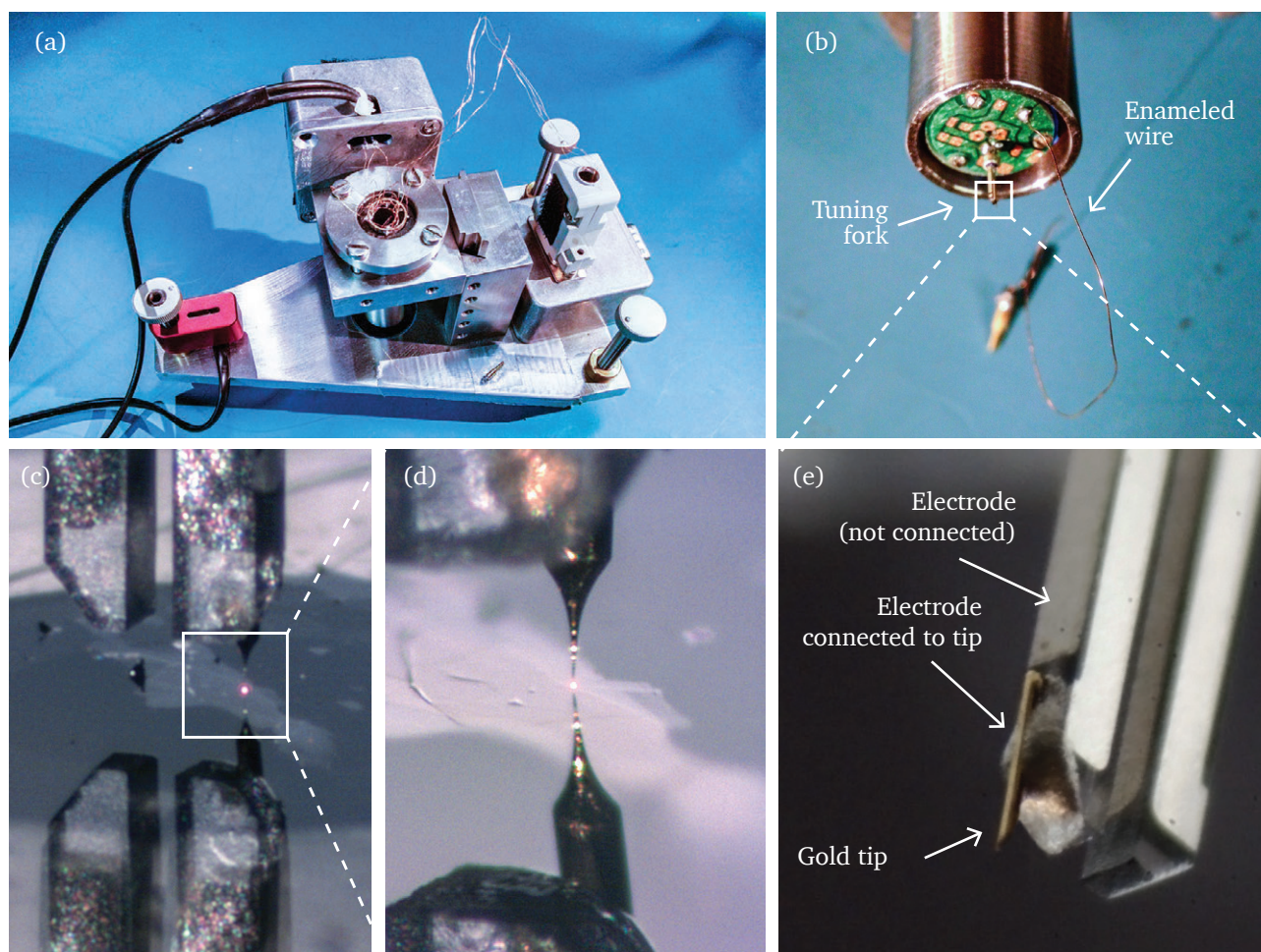
FIGURE 3.10: (a) Photograph of the complete STM scanhead. (b) Photograph of the circuit board used to electrically contact the tip/tuning fork assembly. Note that there are no electric components soldered to this board, which was developed for AFM usage only. Also visible is the enameled wire that connects the probe assembly to the current preamplifier. (c) Photograph from the experimental setup showing part of the tuning fork with an etched gold tip attached. The sample is graphene exfoliated on an ITO covered coverslip. What appears to be the presence of another probe coming from the bottom is actually the reflection of the real probe. The red dot in the middle of the image is the laser spot. (d) Zoomed in view from (c). (e) Close-up view of the STM probe showing the etched gold tip connected to the tuning fork through the use of silver paint.

3.2.1 STM SCANHEAD & CURRENT PREAMPLIFIER

In order to extend the measurement capabilities of the TERS system, a scanning tunneling microscope scanhead was proposed and built (Figure 3.10). It was assembled on the same steel structure as the existing AFM scanhead [37], which facilitates exchanging from AFM to STM whenever needed, requiring only the rewiring of some electrical connections.

The STM tips, which must be conductive, were made from chemically etched gold wires and mounted on quartz tuning forks (see Appendix D). Contrary to AFM, where the tuning fork is the feedback sensor, here it is only used to provide structural support and the needed electrical connection from the tip to the circuitry (Figure 3.10(e)). The tuning fork is soldered to a circuit board that was designed as an amplification stage for the AFM scanhead, but here it serves only as a stable socket with the needed electrical contacts to connect the tip to the current preamplifier.
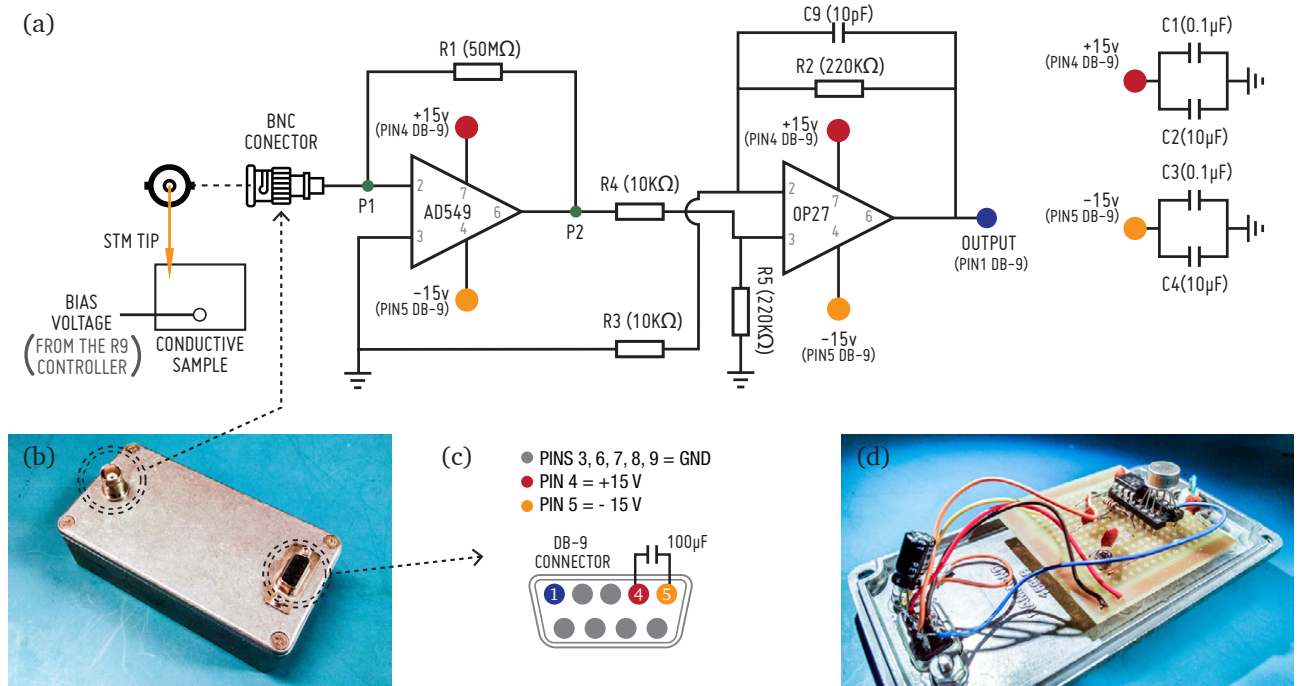
FIGURE 3.11: (a) Schematic of the current preamplifier circuit. (b) Final appearance of the preamp inside its metal casing. (c) Pinout of the DB-9 connector. (d) Assembled circuit on a perforated circuit board.

3.2.2 THE STM CURRENT PREAMPLIFIER

The current preamplifier is a transimpedance amplifier designed to convert the tunneling current to voltage and amplifying it to working levels. Due to quantum tunneling very low current levels, usually ranging from hundreds of pA to tens of nA, a STM preamp must provide an ultra-low input bias. Figure 3.11(a) presents the schematic of the implemented circuit. It consists of two amplification stages based on operational amplifiers (opamps). The first stage is a transimpedance amplifier responsible for converting the tunneling current into electrical voltage. Its gain is calculated by considering an ideal opamp, where no current flows into the inverting and non-inverting inputs. Applying Kirchhoff's 1st law to point $P1$ in Figure 3.11, the voltage output on point $P2$ is given by

$$I_{P1} + \left(\frac{V_{P2} - 0}{R1}\right) = 0 \qquad (3.4)$$

$$V_{P2} = -R1 \times I_{P1} , \qquad (3.5)$$

where $R1$ is a $50\,\text{M}\Omega$ metal oxide special purpose gain resistor with a $\pm0.5\,\%$ tolerance from Vishay®. In this case, the transimpedance amplifying stage converts the tunneling current into electrical voltage providing a gain of $50 \times 10^6\,\text{V}\,\text{A}^{-1}$. For its construction we chose Analog Devices' AD549 operational amplifier. This opamp, as defined by its datasheet [191], is an ultralow input-bias current operational amplifier designed specifically for applications where very low input current is required. The 2nd amplification stage elevates the voltage

to working values; considering $R2 = R5$ and $R3 = R4$, the output voltage from the 2nd stage is given by

$$V_{\text{out}} = \frac{R2}{R4}P2 \ , \qquad (3.6)$$

where, in the end, we have a conversion factor of $1\,\text{V}\,\text{nA}^{-1}$.

Although the 1st stage must use specially selected components, aiming noise reduction, the 2nd stage doesn't need the same finesse and is based on more ordinary components, such as the more general OP27 operational amplifier.

The current preamplifier was developed with the assistance of prof. Dr. Roberto Paniago from the Department of Physics at UFMG.

3.2.3 ELECTRICAL CONNECTIONS

FIGURE 3.12: (a) CVD grown sample on a glass coverslip. The coverslip is mounted on a sample holder by four small magnets. The sample holder is on top of the nanopositioning stage. The bias is applied through the enameled wire which is connected to the sample by a small drop of silver paint. Through the coverslip it is possible to see the oil immersion objective and the laser spot (red dot). (b) piece of HOPG connected to a metal disk by the means of a double-sided carbon tape. The bias voltage is applied through the labeled enameled wire in the same way as in (a).
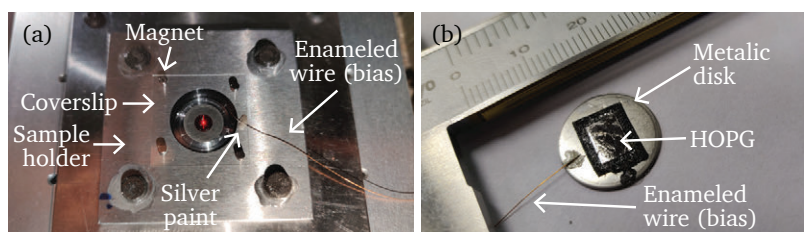
The bias voltage, which is software controlled, is feed directly from the SPM controller to the sample through a coaxial cable (model RF RG174, 50 Ω impedance). On one end, the coax cable is connected through a BNC male connector to the SPM controller. On the other end, which goes to the sample, the BNC's core wire is exposed by stripping it from its insulating protection. Since the core wire is too thick and rigid to be connected directly to the sample, in order to avoid any accidental movement that could rupture the connection and damage the sample or other parts of the system, the exposed coax core is soldered to a $\approx 100\,\mu\text{m}$ thick enameled wire[7] which gets connected to the sample through a conductive silver paint[8] (Figure 3.12).

To electrically connect the tip to the preamp, a piece of enameled wire is soldered to the circuit board in a point where it is electrically connected to the STM tip through one of the tuning fork's metal plates (Figure 3.10(b) and (e)). Similarly to what was done for the bias wiring, the enameled wire is then soldered to a coax which is connected through a BNC male connector to the input of the current preamp, which is a female BNC connector. Once inside the metal casing that encloses the preamp's circuitry, this BNC is directly soldered

[7]Pirelle® Pireform R with specified gauge of 37 AWG

[8]SPI Flash-Dry Silver Colloidal Suspension. Item #: 04998-AB

to the inverting input (pin #2) of the AD549 opamp (Figure 3.11).
One important consideration that must be taken into account is the
stray capacitance on the path from the tip all the way along the wire
that carries the tunneling current to the input of the preamp. The
bandwidth of the preamp is inversely proportional to the length of
this wire, therefore it is important to keep the path from the tip to
the preamp as short as possible. This is accomplished by placing the
preamp on top of the inverted microscope, along side the scanhead.
The opamps are powered directly from the SPM controller, which pro-
vides a ±15 V from a fully linear power supply designed for low noise
performance, which is externally exposed through a DB-9 female
connector, having pin #4 as +15 V and pin #5 as −15 V. The preamp
was designed to also use a DB-9 connector, where, to avoid confusion,
the ±15 V follows the same pinout as the SPM controller's power
supply. The preamp's output voltage is connected to the channel #2
input BNC of the SPM controller.

3.2.4   TEST RESULTS
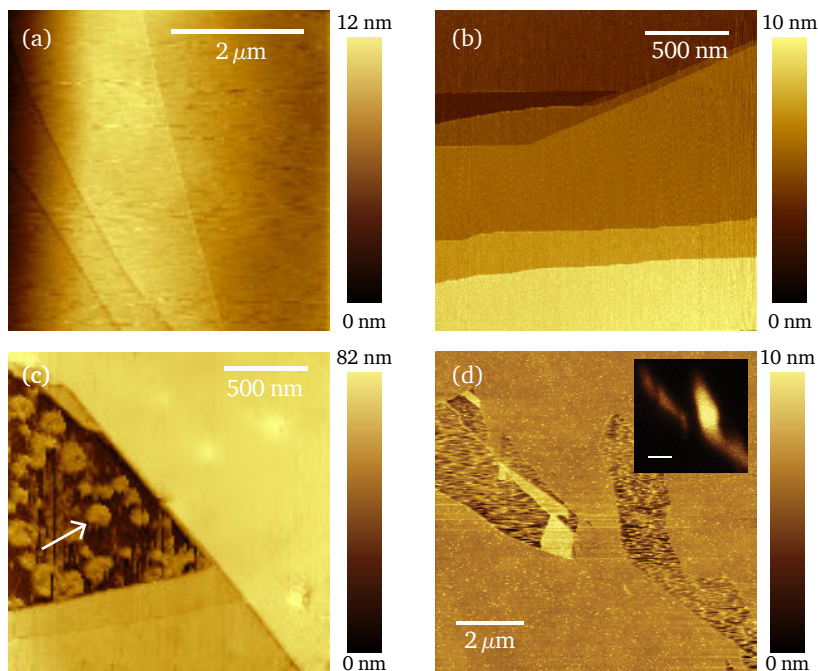
FIGURE 3.13: (a) STM image of atomic car-
bon planes from an exfoliated HOPG sample.
(b) STM image also from HOPG but with a
scan area smaller than (a). (c) STM image
from HOPG exfoliated on an ITO covered
coverslip. (d) STM image of MoS$_2$ exfoli-
ated over an ITO covered coverslip. The
inset shows a confocal Raman image equiv-
alent to the same region.

Figure 3.13 show some experimental results obtained with the
Scanning tunneling microscopy (STM) system. In Figure 3.13(a) we
have the first image acquired with the new STM scanhead and the
designed current preamplifier. The sample is a mechanically exfo-
liated HOPG transfered to a metal plate to which the bias voltage
was applied (Figure 3.12(b)). In the resulting image we can clearly
see the layered planes of carbon atoms. Figure 3.13(b) was also
acquired from a HOPG sample, but this time in a smaller scan area.

Figure 3.13(c) is also from a sample of mechanically exfoliated HOPG, but this time it was transfered to a coverslip that was previously coated with indium tin oxide (ITO). ITO is a transparent conductive thin film commonly used when transparency and conductivity are need. The circle-like formations seen on the image (as highlighted by the white arrow), is the ITO covered coverslip, while the more flat surface corresponds to the layered carbon planes. In order to convert the voltage that gets applied to the z-piezoelectric element to a dimensional value, a conversion factor is obtained by scanning a standardized grating, which has a characterized height. Figure 3.13(d) is a sample of Molybdenum disulfide (MoS_2) also exfoliated on a coverslip covered with ITO. The inset shows a confocal Raman image.

Experimental results obtained with the implemented STM instrumentation, including TERS results, are also shown in Section 4.4.

3.3 SAMPLES FOR TERS

FIGURE 3.14:   (a) solution containing graphene flakes dispersed in H_2O with a non-disclosed surfactant. (b) CamGraph graphene powder before dilution. (c) $5\,\mu g$ of CamGraph graphene powder being dissolved in $20\,mL$ of isopropanol on a sonicator. (d) Coverslip on the sample holder with the graphene solution already dried out. (e) Image obtained through the eyepiece of the microscope exhibiting in (1) a suitable searching region for individual nanographene flakes due to the apparent low concentration and in (2) an inadequate region due to the apparent high concentration.

Proper sample preparation is fundamental when planning a TERS experiment. Knowing that the near-field information is only able to propagate a few nanometers before evanescence, a clean sample, with a very clean top surface is required. Due to the geometry of our system, where the nanoantenna approaches the sample from above and the laser comes from the bottom of the coverslip, the sample most be transparent and devoid of impurities or any other materials not related to the subject under scrutiny, which otherwise might act as a barrier attenuating or completely blocking the near-field signal, or it may even cover up the Raman signal of interest.

3.3.1 GRAPHENE NANOFLAKES

Here we describe the necessary procedures to prepare samples of graphene nanoflakes that are appropriate for TERS measurements based on graphene from two different sources. One provided by the MGgrafeno [192] project team, which consists of graphene flakes dispersed in a solution containing H_2O with a non-disclosed surfactant (Figure 3.14(a)). The solution provided by the MGgrafeno project was produced by a pilot process through liquid-phase exfoliation of natural graphite extracted from mines at the state of Minas Gerais, Brazil. The other is a commercially available graphene from Cambridge Nanosystems under the name CamGraph® G1 graphene powder [193] (Figure 3.14(b)), which, according to the manufacturer, consisted of graphene flakes with one to five layers without the presence of additives, catalysts or metal impurities.

SAMPLE PREPARATION protocol

The sample preparation procedure described here can be accomplished with off the shelf equipments and chemicals. Following is a list of what is required to make ≈20 mL of solution containing an adequate concentration of graphene nanoflakes. The only difference in the preparation process from the graphene from MGgrafeno and the CamGraph graphene is the fact that the last is provided in powdered form and therefore requires a initial dilution as follows:
Using a high precision scale, measure 5 μg of graphene powder. Transfer the powder to a 25 mL beaker and slowly pour 20 mL of isopropanol (purity ≥99.5 %) while gently stirring the flask until complete solubilization of the powder into a pitch black homogeneous solution. Figure 3.14(c) shows the resulting solution.

From here on, the process is exactly the same for both graphene sources, considering that the CamGraph powder has already been diluted.

▶ LIST OF MATERIALS

- Solution containing graphene nanoflakes;

- isopropanol (purity ≥99.5 %);

- beaker (25 mL);

- microscopy glass slide (any size);

- microscopy coverslip (20 × 20 × 0.17 mm[9]);

- micropipette (10 μL);

- hotplate (90 °C);

- sonicator;

- deionized water (Milli-Q® or similar);

- N_2 (dry blow).

[9]The 0.17 mm thickness assumes that the user has an oil immersion objective. It is important to check the objective's requirement

► PREPARATION PROCEDURE

- Add 20 mL of isopropanol to the empty 25 mL beaker;

- With a micropipette draw 10 μL from the graphene solution and drop it in the beaker with isopropanol;

- seal the beaker with Parafilm® or PVC film and place in the sonicator for 3 minutes;

- place the clean microscopy glass slide on the hotplate with its temperature set to 90 °C;

- place the clean coverslip over the glass slide on the hotplate;

- wait ≈5 minutes for the temperature to reach equilibrium;

- use the micropipette and drip 10 μL of the graphene solution onto the coverslip;

- remove the coverslip from the hotplate as soon as the drop on the coverslip evaporates (≈20 s);

- rinse the coverslip with running deionized water for ≈30 seconds;

- Apply a gentle blow of N_2 to the coverslip until dry (≈30 seconds).

Given the above preparation protocol, six samples were prepared, being three from each graphene source. What follows is a sample validation routine involving visual inspection, micro-Raman and TERS exploration.

SAMPLE VALIDATION THROUGH VISUAL INSPECTION

An initial inspection is performed even before taking the sample to the microscope, being done by the naked eye. The sample must look completely transparent and with only a slight coated appearance where the solution was dropped. Figure 3.14(d) shows the sample, already on the sample holder, being visually inspected. Factors that most influence the final quality of the produced sample are: the solution's initial concentration, hotplate temperature and the droplet volume. With the sample appropriately mounted, it is taken to an optical microscope for further inspection. The graphene flakes should be spread all over the drop area and usually with a higher concentration at the borders. A very low initial concentration of the solution makes the task of finding a region with an appropriate amount of isolated

nanoflakes arduous. If the sample is left to dry in ambient conditions, without the assistance of a hotplate, usually the nanoflakes agglomerate mostly at the border of where the drop fell and this high concentration makes it hard to find individually isolated nanoflakes, thus we use a hotplate, with its temperature set to 90 °C, to accelerate the drying process. Also, it is our observation that the drop volume determines not only the size of the final sample area, but also the dynamics of the drying process.

After this initial assessment, the next step is to take the sample to the system in order to prospect for a suitable region to carry out the measurements. Once on the inverted optical microscope, with the assistance of a white light source the sample is visually inspected and an area where a graphene concentration can be visually spotted is located. In our system this is done by manually moving the sample holder while looking through the eyepiece of the inverted microscope. Figure 3.14(e) shows an obtained image where we can see a region with low (Figure 3.14(e)(1)) and high (Figure 3.14(e)(2)) concentration. Our experience suggests that the most promising areas to find isolated graphene nanoflakes are those apparently devoid of any material, similar to those shown in Figure 3.14(e)(1), however occurring nearby ($\leq$200 μm) from areas with easily visible concentrations, such as those in Figure 3.14(e)(2).

SAMPLE VALIDATION THROUGH RAMAN IMAGING

Following the initial visual inspection, the sample is then explored through micro-Raman spectroscopy. The laser power was set to $\approx$2.4 mW, as measured at the sample, for this initial exploration without the presence of the tip. The scan speed, as well as the laser power, might be adjusted for any given scan depending on a number of factors, such as the signal intensity, sample temperature threshold, scan area and the presence of the tip. Therefore, whenever relevant for the discussion, the actual used values will be disclosed. For a confocal APD scan with such laser power, the scan speed is usually set to 1 s/line, while for a SPM/TERS experiment, the scan speed is usually limited to 500 nm s^{-1}. This is based on the fact that faster scans can jeopardize the tip integrity. When using a TERS tip (see Section 3.4), due to the malleability of pure gold, from which it is made of, any slight collision with the sample surface will damage the tip's apex causing a diameter increase and impairing its plasmonic capabilities. Also, for TERS with our nanoantennas, the laser power must usually be $\leq$300 μW, as measured at the nanoantenna.

FIGURE 3.15: APD images acquired from the same sample containing graphene nanoflakes, but at different locations on the coverslip. The bandpass filter on the APD was centered on the graphene's G band. The graphs below each image plot the intensity count obtained from the APD at the positions marked by the dashed lines. (a) $30 \times 30\,\mu m^2$ scan from an excessively concentrated region. (b) $30 \times 30\,\mu m^2$ scan from a different region. The bright yellow spot is due to a contamination of unknown origin in the sample that had a very intense photoluminescence response, $\approx 30\times$ more intense when compared with the signal coming from (a), thus the scan area is not appropriate for TERS. (c) $20 \times 20\,\mu m^2$ scan from a clean area with individual sparse flakes. (d) Raman spectra taken from points P1, P2, P3 and P4 highlighted in (c). Below (a-c) is provided a line profile taken from the position of the white dashed line. In (c) two line profiles are taken from two distinct locations, "aa" and "bb", as labeled, showing the difference in intensity from both locations.

Initial exploration was done with an APD, due to its higher sensibility, which allows faster scans. The APD was equipped with a combination of two bandpass filters, whose intersection gives rise to a narrower bandpass filter appropriate for imaging the graphene G band excited with a 632.8 nm laser line. One filter is centered on 700 nm with a 13 nm bandwidth and the other is centered on 725 nm with a 40 nm bandwidth. This combination acts as a single bandpass filter centered on ≈ 706 nm ($\approx 1633\,cm^{-1}$) with a FWHM of ≈ 9 nm ($\approx 170\,cm^{-1}$), where only the graphene G band ($\approx 1580\,cm^{-1}$) is transmitted.

Figure 3.15(a) shows the resulting image from a $30 \times 30\,\mu m^2$ scan area. A first glance at the obtained image is enough to infer that the current scan area has a very high concentration of graphene flakes, therefore it is not an appropriate location to try to find isolated ones. Before considering the preparation of a new sample, we manually moved the sample to another location and tried another scan[10], with the results shown in Figure 3.15(b). The bright yellow spot had an atypical high intensity response, when compared with another region on the same sample, as shown in Figure 3.15(a), meaning this is a fluorescent contamination of unknown origin and therefore should be avoided or it could damage the TERS tip. The graph below the image is a section showing the intensity line profile at the position of the white dashed line. Figure 3.15(c) shows the result of a $20 \times 20\,\mu m^2$ scan area. A visual inspection of the acquired image shows a sparse density of graphene flakes in the area. Figure 3.15(d) shows four Raman spectra taken from the highlighted points in Figure 3.15(c). As expected, the amplitude of the G band is higher on those points that had a higher intensity on the APD image.

It is important to observe that the intensity variation is a relevant indirect measure of the nanoflake size. In theory, if every graphene

---

[10]This manual movement of the sample should be done before placing the SPM scanhead on top of it, otherwise it becomes a daunting task and there is a possibility of damaging the tip. For this reason it is important to extensively characterize the sample before proceeding with SPM.

FIGURE 3.16: Confocal and TERS results obtained from a sample containing graphene nanoflakes. (a) and (b) show confocal micro-Raman images acquired with an APD with a composite bandpass filter for the G band. (b) shows the image of an isolated nanoflake that cannot be spatially resolved due to its small lateral size. (c) shows the AFM topography image obtained during a near-field hyperspectral scan. The brightest spot in the image corresponds to an AFM height of ≈ 12 nm from the coverslip surface, as shown by the line profile obtained at the position of the white dashed line and plotted on the upper right graph. (d) and (e) are near-field hyperspectral images generated from the D and G Raman bands respectively. (f) Shows is the Raman spectra obtained at the point marked in (e) with (red spectrum) and without (blue spectrum) the presence of the tip. The observed spectral enhancement for both D and G band was $I_{NF}/I_{FF} \approx 12$ and for the 2D band was $I_{NF}/I_{FF} \approx 18$ (adapted from [194]).

nanoflake were smaller than the Airy disk, presenting exactly the same pristine crystalline structure, including the number of layers, based on Eq. (2.12), intensity variations could be directly related to their physical dimensions. Since the number of layers and the amount of defects present are highly variable from one flake to another, the intensity cannot be used as a direct measure of size, however it is valid to use it as a starting point and to assume that the fainter ones are likely smaller. Also, due to a flake's small size compared to the excitation wavelength and, consequently, the Airy disk, it can be considered an impulse stimulus to the imaging system. Thus its response in the acquired image is an approximation of the optical system's PSF, which explains why they all look similar in Figure 3.15(c).

TERS OF A GRAPHENE NANOFLAKE

To throughly map the sample, another $50 \times 50\,\mu m^2$ APD scan was performed, as shown in Figure 3.16(a), followed by a $1.8 \times 1.8\,\mu m^2$ scan with the resulting image shown in Figure 3.16(b). It is relevant to notice the inability to spatially resolve the given nanoflake due to the diffraction limit, thus such a flake is an interesting candidate for a near-field experiment.
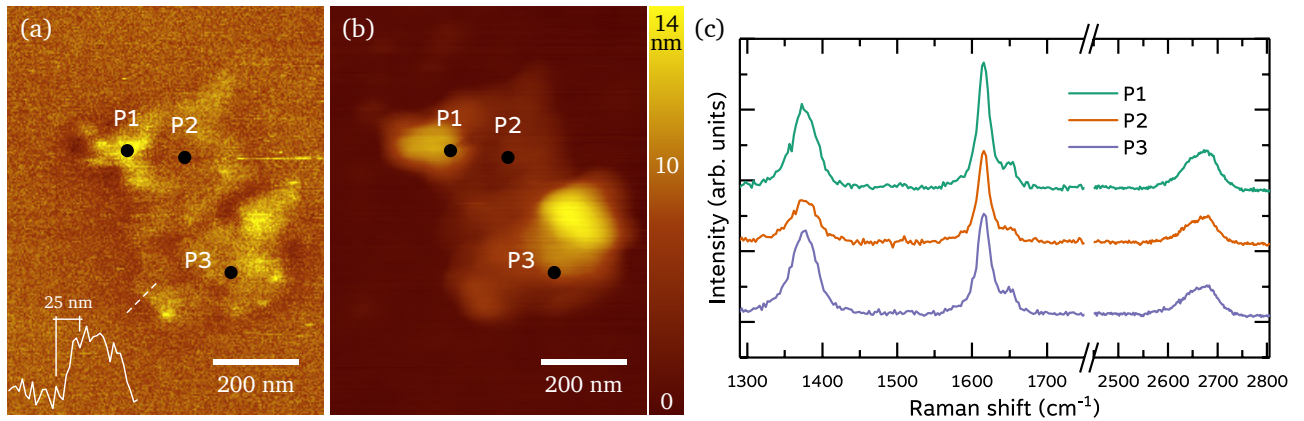
FIGURE 3.17: (a) TERS image of the graphene nanoflake acquired with an APD with a bandpass filter combination for the G band (same as in Figure 3.16). The white line profile at the bottom right is the intensity profile from the position of the dashed white line. (b) AFM Topography image obtained simultaneously during the same scan procedure. (c) TERS spectra corresponding to points P1, P2 and P3 as shown in (a, b).

With a suitable region properly mapped, the scanhead, with the nanoantenna already mounted, is placed on top of the inverted microscope. An AFM-TERS hyperspectral scan was performed (see Section 3.5.1). The data used to generate the images shown in Figure 3.16(c-e) were acquired simultaneously, during the same scan procedure. Figure 3.16(c) is the AFM topography image, while (d) and (e) are near-field optical images generated from the intensity of the D and G Raman bands in graphene, respectively. Figure 3.16(f) shows the Raman spectra with and without the presence of the tip (red and blue spectra, respectively). Given the near-field intensity of a given band as I_{NF} and the far-field intensity from the same band, I_{FF}, the TERS response shows a spectral enhancement for both D and G band $I_{NF}/I_{FF} \approx 12$ and for the 2D band $I_{NF}/I_{FF} \approx 18$.

Based on the fact that graphene is a two-dimensional system, the resulting gain in signal intensity corresponds to an expressive enhancement factor, that comes as a consequence of the efficient near-field information collection by the nanoantenna (see Section 3.4). When comparing the acquired AFM topography image in Figure 3.16(c) with the near-field images generated from the hyperspectral scan data in Figure 3.16(d, e), it becomes clear that the nanoflake was optically resolved below the diffraction limit.

Figure 3.17 shows one last scan performed on this same nanoflake, but this time on a smaller $1 \times 1\,\mu m^2$ area. Once again it is clear the ability to capture the local field enclosed by the nanoantenna apex diameter. The white graph inset on Figure 3.17(a) represents the intensity profile from the G band at the border sectioned by the white dashed line. The sharp edge indicates a spatial resolution of $\approx 25\,nm$, as highlighted by the dimension line. Raman spectra where acquired with a longer integration time from points P1, P2 and P3, with the results shown in Figure 3.17(c), revealing a spectral variation that

can be extracted from a sample below the diffraction limit. Because features such as number of layers, grain boundaries, strain, doping and defects greatly affect the characteristics of a material, it is important to understand if the information revealed through TERS is capable of bringing any relevant new information that micro-Raman is incapable to provide.

The obtained results shown here were fundamental to validate not only the sample preparation protocol, but the TERS system and the employed nanoantennas. Further micro *versus* nano exploration is discussed in Chapter 4.

3.3.2 EXFOLIATED GRAPHENE WITH HELIUM ION MICROSCOPE PATTERNED LINE DEFECTS
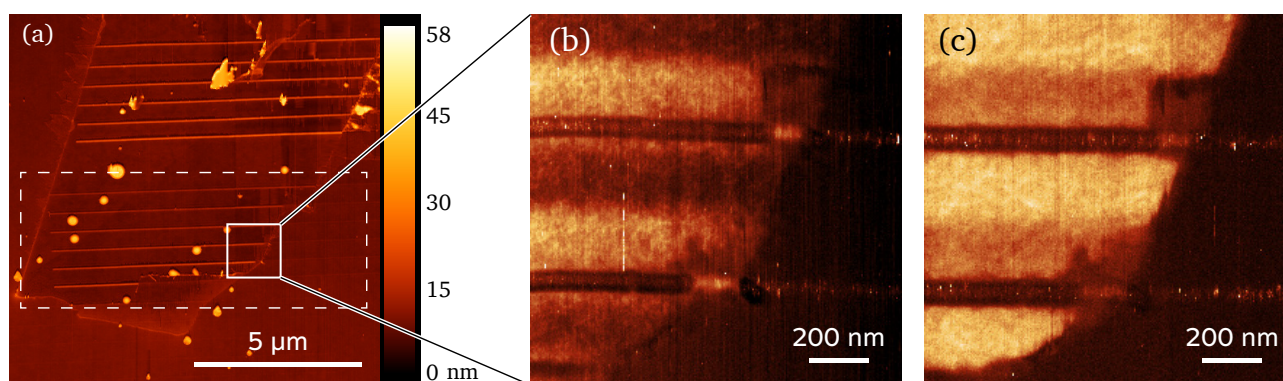
FIGURE 3.18: (a) Topography image from a $12 \times 12\,\mu$m scan area. (b) APD image (D band) from a $1.28 \times 1.28\,\mu$m scan area in the location highlighted by the solid white square in (a). (c) APD image (2D band) in the same location as (b). The white dashed square in (a) received an estimated dose of $\approx 1.2 \times 10^{17} \text{He}^+/\text{cm}^2$

Instituto Nacional de Metrologia, Qualidade e Tecnologia

The sample reported here was created at the *Divisão de Metrologia de Materias* of Inmetro, the National Institute of Metrology, Quality and Technology of Brazil. It consists of an exfoliated single-layer graphene sheet that was submitted to a milling process in which defect lines were controlled patterned by helium ions microscopy. The ions were accelerated with an energy potential of 30 kV, colliding with the sample surface at a 45° angle and generating the patterned lines shown in Figure 3.18(a). The equipment used was an ORION NanoFab Helium Ion Microscope, manufactured by Zeiss Company, and the all the measurements were performed by Dr. Thiago L. Vasconcelos, from Inmetro.

Figure 3.18(a) shows an AFM topography image from the entire graphene sheet, in which the vertical straight lines correspond to defect lines patterned by the helium ions. The region highlighted by the white dashed square received doses of $\approx 1.2 \times 10^{17} \text{He}^+/\text{cm}^2$. Figure 3.18(b, c) shows a $1.28 \times 1.28\,\mu\text{m}^2$ APD images from the graphene's D and 2D bands, respectively, taken from the location highlighted by the white rectangle in Figure 3.18(a). Based on the provided images, it becomes clear that the sample was optically

resolved below the diffraction limit. A hyperspectral TERS scan was also performed in the same location as Figure 3.18(b,c) and the resulting analysis based on this graphene sample, as well as from the samples discussed in Section 3.3.1 will be presented in Section 4.3.

3.3.3 TWISTED BILAYER GRAPHENE GROWN BY CHEMICAL VAPOR DEPOSITION

FIGURE 3.19: (a) SEM image from the CVD grown graphene sample. (b) APD micro-Raman confocal image from a spectral range that includes the D and G Raman bands (spectral energy between $1250\,cm^{-1}$ and $1780\,cm^{-1}$). (c) Raman spectra at 3 different locations marked in (b) by the numbers 1, 2, and 3, after background subtraction. Spectrum #1 is the Raman spectrum of a twisted bilayer graphene, #2 corresponds to a bilayer graphene and #3 corresponds to a single-layer graphene. SEM image in (a) was provided by our collaborators from Aalto University.

This sample consists of a chemical vapor deposition (CVD) grown twisted bilayer graphene [195] on a glass coverslip. Figure 3.19(a) shows an scanning electron microscopy (SEM) image from the sample. Figure 3.19(b) shows an APD confocal micro-Raman image from both the D and G Raman bands. In order to better characterize the sample, spectra were acquired at the points marked in Figure 3.19(b), which are shown in Figure 3.19(c). The spectral intensity of the G band in the spectrum labeled 1 in Figure 3.19(c), indicates the presence of a resonant twisted bilayer graphene [195]. The graphene layer covers an area of $\approx 5 \times 5\,mm^2$. Due to such a large conductive area this sample is specially interesting to be investigated by STM-TERS, which is reported in Section 4.4

The sample was created in the Department of Micro and Nanosciences of the Aalto University, Finland, by Prof. Juha Riikonen.

3.3.4 SUSPENDED GRAPHENE MEMBRANES

FIGURE 3.20: Exfoliated graphene before (a) and after (b) being transfered to a 500 nm thick SiN$_x$ membrane, perforated with 10 µm diameter holes. In (c) a photograph of the entire *Si* slab placed on top of the sample holder. (a, b) were provided by Dr. Aravind Vijayaraghavan.

The sample shown in Figure 3.20 consists of a mechanically exfoliated graphene that was transferred to a silicon substrate covered by a 500 nm thick SiN$_x$ (silicon nitrate) layer in which 10 µm circular holes have been carved through a photolithography process [196]. The sample was developed in collaboration with Dr. Aravind Vijayaraghavan from the University of Manchester. He also provided the photograph in Figure 3.20(a) which shows one of the graphenes before being transfered to the Si/SiN$_x$ substrate shown in Figure 3.20(b). The graphene membrane fully covers the 10 µm holes.

Due to the geometry of this sample, it is possible to press the graphene membrane from above while simultaneously acquiring the Raman signal from underneath. The TERS system described in Section 3.1 is highly suitable for this kind of nanomanipulation experiment and the results of such exploration is reported in Section 4.5.

3.4 IMPROVEMENTS IN OPTICAL ANTENNAS TECHNOLOGY

The term antenna, according to the IEEE *Standard Definitions of Terms for Antennas*, is defined as "*a means for radiating or receiving radio waves*" [197]. Radio waves, as well as light, is a propagating electromagnetic radiation, but whereas radio wavelengths range from the millimeter to the thousands of kilometers range, the wavelength of light, in the visible spectrum, range from approximately 380 nm (violet) to 750 nm (near-infrared). This large discrepancy in wavelength is fundamental to understand what sets radio antennas apart from optical antennas. Antennas are transducers with the purpose of converting electromagnetic radiation into localized energy, and vice-versa, where the length ℓ of the antenna is directly related to the wavelength λ of the propagating field. Considering that a half-wave dipole antenna has a length $\ell = \lambda/2$, if we take the lower limit of the radio spectrum, with wavelengths in the millimeter range, building antennas this size does not present a technology challenge, being totally feasible. However, considering nanometer sized wavelengths, with a needed accuracy in units of a nanometer, it becomes technologically challenging. The manufacturing process of such small structures is not the only limiting factor here. Under a low frequency regime, such as those in the radio frequency, only intraband transitions are present in metals, thus, in this frequency range, metals can be modeled as almost perfect conductors. On the other hand, as the frequency of the electromagnetic field increases, metals can no longer be considered perfect conductors, therefore its ability to work as an antenna is now strongly related to surface plasmon resonances, whose wavelength is smaller than the wavelength of the incident radiation [198]. Therefore what dictates the light/antenna coupling is no longer the relation between the antenna's length ℓ and the wavelength of the incident field, but the wavelength of the surface plasmon resonance, more specifically of the localized surface plasmon resonance (LSPR). LSPR is defined as the resonant oscillatory movement of conductive electrons on nanostructures smaller than the incident field's wavelength [199].

TERS probes can be manufactured from a gold wire through an electrochemical etching process (Figure 3.21). In the end, the goal of achieving a tip with a nanometric sized apex is possible, given a well characterized setup and the ability to stop the corrosion process at the right moment, even though having a tip with a nanometric sized apex does not guarantee the availability of LSPR, which is in fact dictated
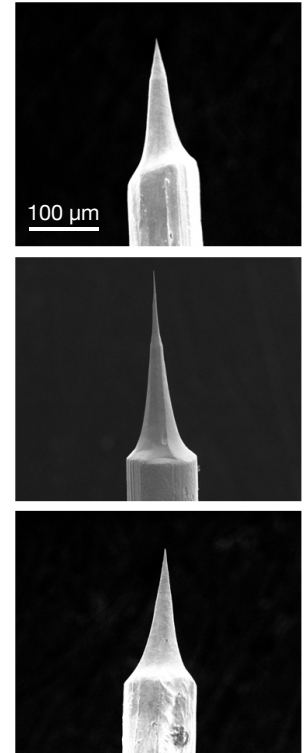

FIGURE 3.21: Etched tip as seen by a scanning electron microscope (SEM) where one can see the undesirable variation of the etching process.
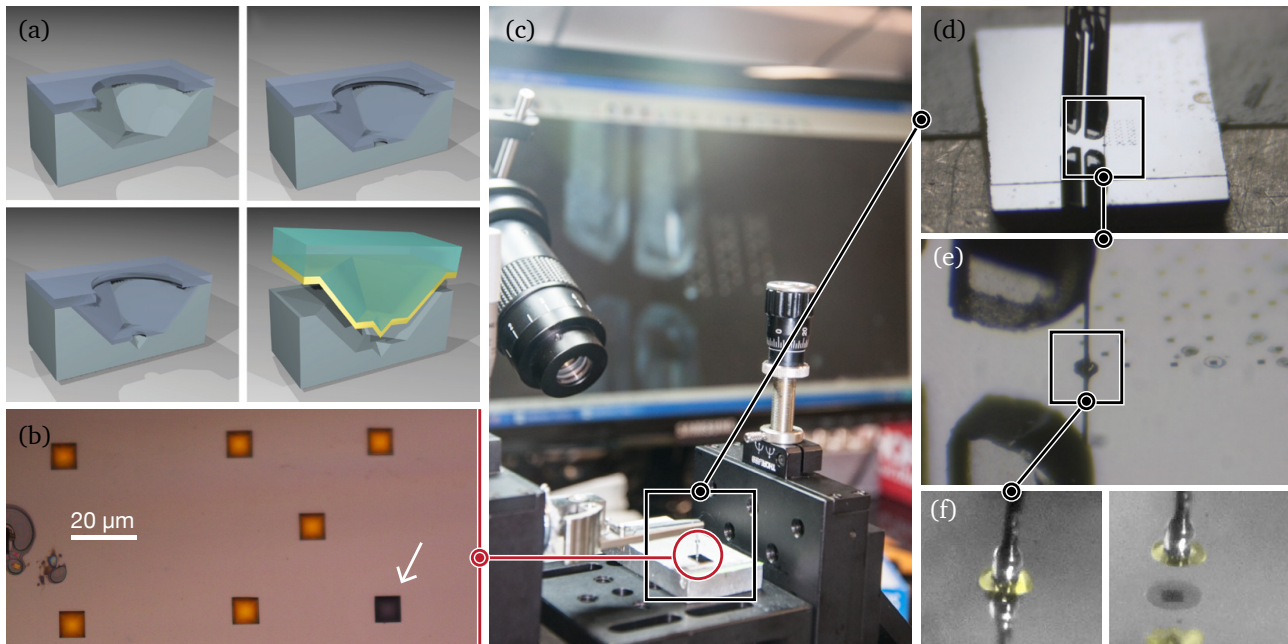
FIGURE 3.22: (a) Illustration showing the steps involved in the fabrication of a PTTP, from the etching steps, to gold deposition and tip extraction (from [40]). (b) Silicon template after gold evaporation as seen from an optical micrsocope. The darker square (white arrow) is a cavity from where a tip has already been extracted. (c) Extraction setup with camera attached to a long distance microscope. The monitor in the back shows the image as seen from the camera. (d) Tuning fork with attached tungsten wire already placed inside a cavity containing a gold pyramid ready to be extracted (view from the camera). (e) Zoomed in image from (d). (f) The exact moment when a PTTP is extracted from the silicon template. The image has been artificially colored to to highlight the gold and geometry of the PTTP.

by the underling crystalline structure (gold crystallites). Thus, in the end, chemically etched tips have a very low yield, not only due to the intrinsic variance in the electrochemical etching process, but mostly due to intrinsic need of having a nano-crystallite gold structure forming a resonant cavity in the right position near the apex, which cannot be controlled by such fabrication process.

Aware of such difficulties, we proposed [39] a reproducible route for tuning LSPR on electrochemically etched gold tip [38, 41]. The technique revolves around the execution of an incision at a distance L from the apex, where changing L results in a fine-tuned LSPR mode.

Although proved effective, this process still required the fabrication of good quality electrochemically etched gold tips as well as the additional focused ion beam (FIB) milling step for every single tip, which is an expensive and, in the case of the etched tips, manual and time consuming process. Based on an existing processes of creating pyramids like structures on silicon wafers, which can be used as a template for large scale production [200], this process was improved [40, 42].

These new nanoantennas, named plasmon-tunable tip pyramids (PTTPs), were developed with the purpose of creating optically efficient probes, with high yield, through a scalable manufacturing method. The fabrication process, as described in [42], is based on a photolithography process where a silicon wafer is chemically etched, generating a pyramid-shaped cavity. Gold is evaporated on the surface of the silicon wafer where the etched cavities act as molds. After the evaporation step, the PTTPs are extracted and the nanoantenna
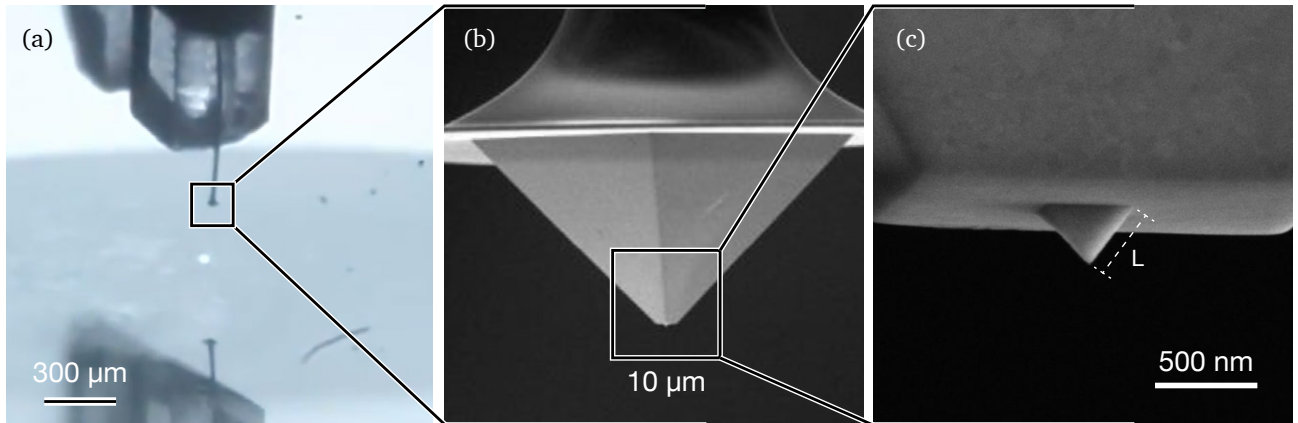
is ready for usage. Previous to the extraction process a small piece of tungsten wire is glued to one of the prongs of a tuning fork. With a diameter of only 15 μm, it is to this tungsten wire that an extracted PTTP will be attached (Figures 3.22 and 3.23).

During the first experiments with this new nanoantenna topology, we sought to obtain experimental data using PTTPs of varying sizes of L, where L in a PTTP is equivalent to the length of the pyramid edge that connects its apex to its base (Figure 3.23(c)). The length L allows an adjustment in the resonance of the surface plasmons, hence the name plasmon-tunable tip pyramids. In Figure 3.24(a) we have a plot showing the enhancement of differing sizes of L obtained on monolayer graphene. Figure 3.24(b) shows two spectra: the green line is without the presence of the nanoantenna and the red line is with the nanoantenna interacting with the sample. The PTTP used had an $L = 500$ nm and a 20 nm apex diameter, as measured through SEM.
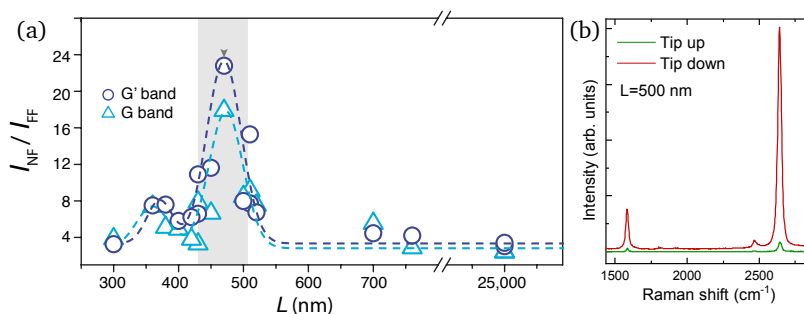
FIGURE 3.24: Enhancement data obtained from a monolayer graphene sample from various PTTPs with varying L lengths (adapted from [40]). Two Raman spectra obtained from a monolayer graphene with (red) and without (green) the presence of a PTTP. The utilized PTTP had an apex size of 20 nm, as measured by a SEM and a $L = 500$ nm.

From all the limitations imposed by etched tips (Figure 3.21), the most hindering is that their optical response is unpredictable. Even if they provide near-field enhancement, the magnitude of the result is usually one order of magnitude less than what we have been achieving with the PTTPs. The PTTP provided the enhancement needed to perform TERS in 2D systems, enabling the TERS signal to overcome the far-field.

3.5 SOFTWARE DEVELOPMENTS & SYSTEM INTEGRATION

3.5.1 HYPERSPECTRAL IMAGING

APDs are very efficient photon counters, enabling the generation of raster scanned images at a relatively fast pace[11], but its usage can be severely limited due to its intrinsic inability to distinguish wavelength variation, thus depending on external bandpass filters. Spectrometers, on the other hand, can be two orders of magnitude slower[12], but when used as a scanning data acquisition device it presents great advantages. The acquisition of an entire Raman spectrum per point provides the user with an invaluable amount of data, allowing not only the correlation of Raman peaks in the same spectrum, but also to correlate spectral and spatial data. Such a technique is know as hyperspectral imaging (HSI) [201].

[11]In our system, in order to obtain a Raman signal-to-noise ratio acceptable for scientific analysis, the maximum scan speed is $\approx 10\,\mu\mathrm{m\,s^{-1}}$ (for a strong Raman scatterer such as graphene). This results in an acquisition time in the order of a few minutes to tens of minutes for a whole image, depending on the desired pixel resolution and image size.

[12]This is based on the equipment we have at our disposal. There are spectrometers equipped with electron multiplying CCDs (EMCCDs) that are capable, according to the manufacturer, of single photon counting and high acquisition speeds, in the same order of magnitude as those from an APD.

FIGURE 3.25: (a) Representation of a data parallelogram. Each cell in the front face (cyan) corresponds to a measurement location and consequently a pixel in the final image. The z-axis, named "spectra", is the data storage for the spectra acquired, one for each point. The highlighted green and orange areas in the spectra axis corresponds to a band that has been selected to generate the image in (c) and (d). (b) Raman spectrum showing two selected Raman bands used to create (c) and (d). (c) is an image generated from the intensity of the graphene's G band and (d) is from the intensity of the 2D band. Both images were synthesized from the same spatial position acquired in a single hyperspectral acquisition. (e) APD image with a bandpass filter centered on the frequency of the G band (adapted from [194]).
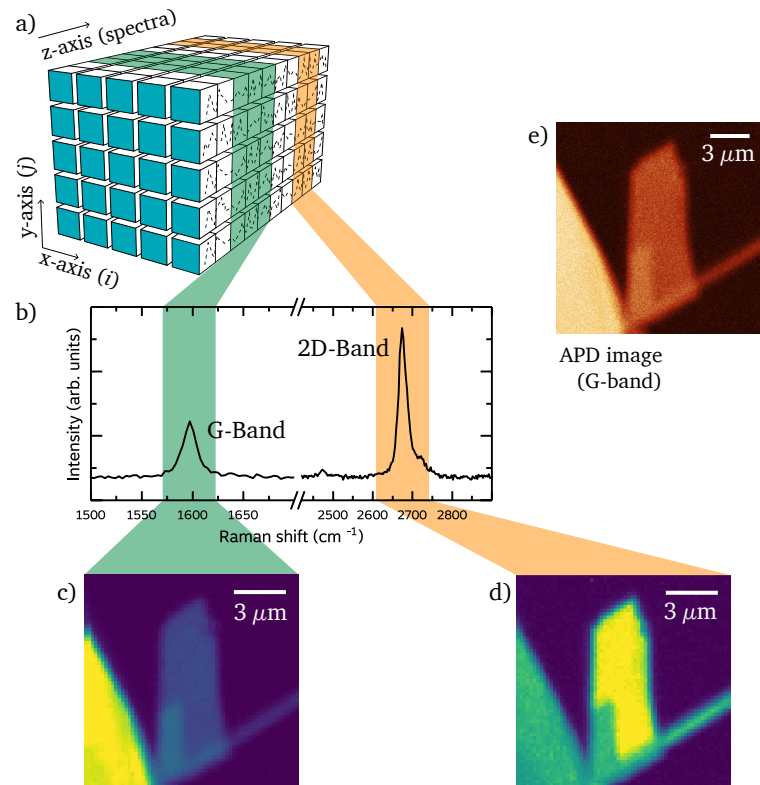
A hyperspectral image comprises a three-dimensional set of data and can be understood as a data parallelogram (Figure 3.25(a)), where one of the faces represents the (i, j) spatial coordinates of the final image in the same way as in a two-dimensional image, but stored in each coordinate is one Raman spectrum. Therefore, a hyperspectral image is composed from dozens, or even thousands of individual spectra, each one contained in a specific row/column

- (i, j) - coordinate. Each point (i, j) in this data parallelogram can be mapped to a coordinate (x, y) in the real space, given that this meta-information was somehow stored. In order to be able to perform hyperspectral image with the TERS system, there was the need to integrate the scanning system, spectrometer and the SPM controller. This was necessary in order to synchronize the spectral acquisition with each step of the scanning process, so we could actually build the aforementioned data parallelogram. The spectrometer used in our system is an isolated system, with its own proprietary software and without features for dealing with three-dimensional data. It provides a way to acquire spectral data based on external triggering and also the possibility of saving the data as a sequence of spectra, but lacking the storage of any additional meta-data, such as the physical dimensions involved in the scan and the total number of points in each dimension. The SPM controller, which is a more open and capable system, and also responsible for all the scanning procedures, was programmed to trigger the spectrometer at each movement of the scanning stage and wait until the spectrometer finished acquiring the data. After the spectrum is acquired, the SPM controller moves the scanning stage once again, triggers the spectrometer and the procedure repeats, as shown in Figure 3.26. In the end, two files are needed to reconstruct the data: the spectral series saved by the spectrometer software and another proprietary file belonging to the SPM controller, where scan parameters, such as the scan speed and the scan dimensions are stored. In spite of the advantages, it is important to emphasize that one of the limitations of the technique is the usually long period of acquisition necessary to obtain the data, where, depending on the signal strength, could take hours to complete. This is due to the low quantum efficiency of CDDs and the signal losses in spectrometers in general when compared to APDs. Therefore, depending on the situation, the use of the technique might be unfeasible. As an example, in order to obtain a final hyperspectral image from a 64 x 64 pixels scan, a total of 4096 spectra will be acquired.

Due to the large amount of spectral data acquired during each experiment and due to its hight dimensionality, the visualization and analysis of hiperspectral images is not a trivial task and softwares were developed to parse and analyze the stored data.
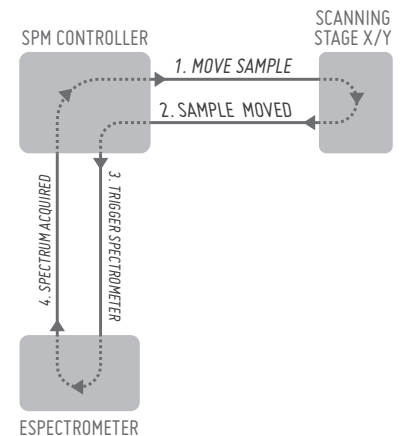
FIGURE 3.26: Sequence of events needed to integrate the system in order to execute a hyperspectral scan.

HSPE – HYPERSPECTRUM TOOLBOX

After a hyperspectral scan, in order to generate an actual image, one must choose a way to extract what will become the pixel value from each spectrum contained in each coordinate. One simple way to approach this problem is to extract a single numerical value from each spectrum based on certain criteria, for example by averaging the n highest intensity points inside a certain selected interval and using the resulting value as the pixel intensity.

FIGURE 3.27: Screenshot from the HSPE software showing in (a) one of the spectra contained in the dataset, (b) tools available for creating, editing and removing bands. In (c) images generated from the two user created bands, where the arrows indicate the correspondence between band and image.
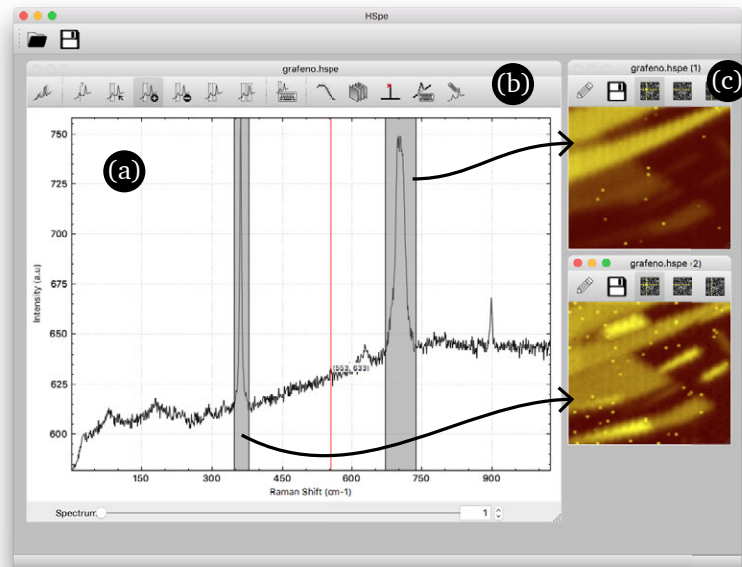
Based on this concept, a software for image generation from a hyperspectral dataset was developed. Named HSPE, it provides the user with a graphical user interface (GUI) where one is able to explore all the spectra inside a hyperspectral dataset and, by graphically selecting a region on any spectrum from the dataset, an image is generated. Figure 3.27 show the software interface where a hyperspectral dataset is already open and two regions have already been selected by the user (Figure 3.27(a)) and the generated images, one for each band, are displayed (Figure 3.27(b)).

The software works in the following way: After opening a hyperspectral image, the user is able to browse through every spectrum in the dataset. With a given spectrum displayed, the user is able to click and drag over the spectrum in order to select a spectral region. After releasing the mouse, a window with an image based on the selected region is automatically generated and displayed. The algorithm employed works in the following abstracted manner: after the user selects a region, the software first removes the background as a
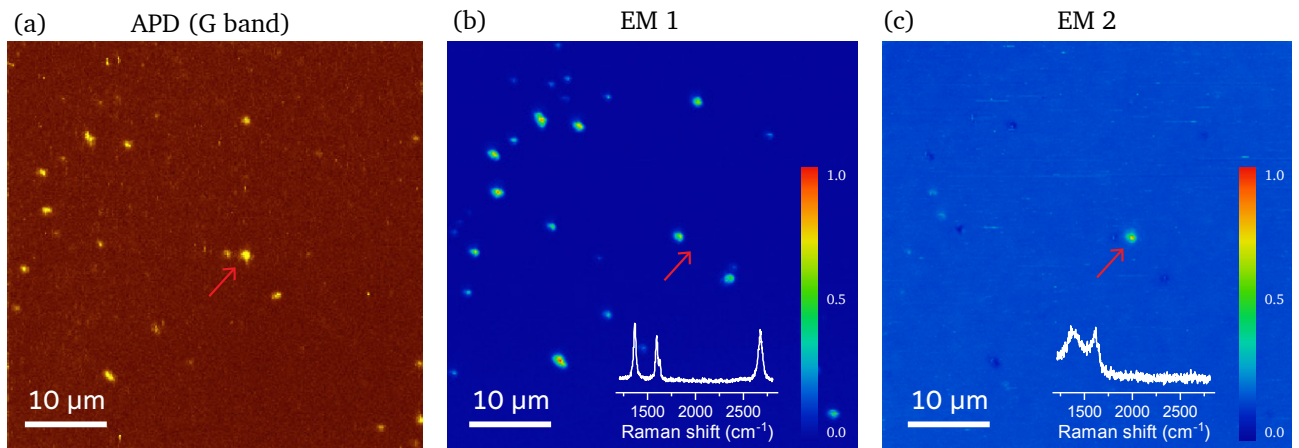
FIGURE 3.28: (a)APD scan (G band) from a $50 \times 50\,\mu m^2$ area. A hyperspectral scan was acquired from the same area and went through a spectral unmixing to generate (b-d). (b) Generated image based on the abundance of EM 1 (inset in at the bottom of the image), which is the spectral fingerprint of highly defected graphene. (c) Generated image from EM 2 (inset in at the bottom of the image), which corresponds to an amorphous carbon fingerprint. The red arrow in (a-c) correspond to the same position and points to the amorphous carbon position, showing that spectral unmixing was able precisely isolate it. The color scale in (b, c) is the contribution of the given EM in each pixel, where 1.0 actually means the original position of this EM in the image.

means to have a baseline at the zero position. To find this baseline, the software averages the intensity from five points immediately the left and five points immediately to right of the first and last points in the selected region, respectively. Then the software subtracts all the points inside the given range from the equivalent coordinates of this line. This is done for all spectra in the dataset. Following this linear background removal, the software then finds the point with the highest intensity. Given this point, it averages its intensity with the intensity from the first point immediately to the left and to the right. This is obviously done automatically for all the spectra in the hyperspectrum. The resulting intensity becomes the pixel intensity in the displayed generated image [202].

SPECTRAL UNMIXING

Spectral Unmixing [203, 204] is a dimensionality reduction tool [205], that, in its simplest form, needs no input from the user except the acquired data and the dimensionality of the newly reduced dataset. It is based on the concept of finding unique, representative spectra in a given dataset, known as endmembers (EM) [206], and to map its contribution to a given pixel in the final image, known as its abundance.

The unmixing process is based on the number of endmembers, n_{EM}, given by the user, where, in the end, the dimensionality of reduced dataset will be equal to n_{EM}. The algorithm works to find amongst the dataset the n_{EM} most distinct spectra that represent the entire dataset. As a final step, the unmixing algorithm calculates the abundance maps, being one for each endmember. An abundance map is an image where the intensity of each pixel, given from 0 to 1, represent the endmember's contribution to the intensity of that given pixel, being 0 no contribution up to 1, meaning the pixel is identical to that endmember.
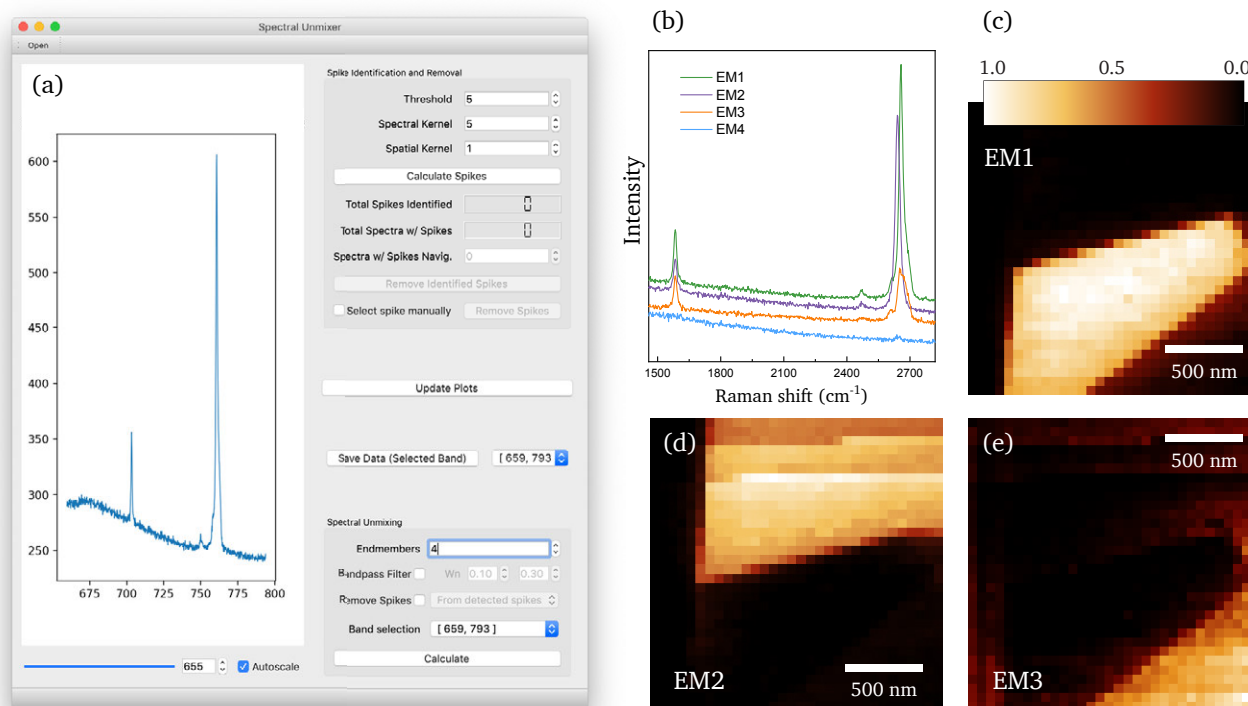
As an example of its usefulness, spectral unmixing can help deter-
mine if a sample contains spectral signatures that might indicate any
kind of contamination, which could be hard to do through APD imag-
ing and even from a hyperspectral scan in which the analysis is done
through the selection of spectral bands, as explained in Section 3.5.1.
This is due to the fact that if the extraneous emission happens to fall
in the same wavelength as the band under analysis, it would appear
to be legit. Spectral unmixing allows such exploration in a fast and
effortless way. As an example, consider Figure 3.28, where in (a)
we have a confocal APD image (G band) obtained from scanning a
$50 \times 50\,\mu m^2$ area. A hyperspectral confocal scan was also performed
on this same area and it was comprised of 256×256 points, there-
fore containing a total of $65\,536$ spectra. Figure 3.28(b, c) shows the
abundance maps generated from EM 1 and EM 2, respectively, whose
spectral signature is shown in white as an inset to each figure.

It is important to notice that spectral unmixing was efficient to
isolate a single nanoflake that had a spectral signature characteristic
of amorphous carbon, highlighted by a red arrow in Figure 3.28(a-c),
which would have been impossible to do in a single APD scan, due
to the fact that the D and G Raman bands are present in amorphous
carbon, as well as in highly defective graphene, as can be clearly seen
in (a). Also, based on the unmixing output, it is safe to say that the

selected area can be considered free of any considerable, micrometer sized, contaminants, showing only the presence of a single amorphous carbon flake amongst the expected graphene flakes.

In order to facilitate the usage of the spectral unmixing technique, as well as to provide the user with additional tools embedded in a GUI, a custom software named Spectral Unmixer was developed. Given a hyperspectral dataset the only required parameter is n_{EM}. Figure 3.29(a) shows the interface of the software with a loaded dataset. The results in (b-e) are from the calculation with $n_{EM} = 4$, where in (b) we have the actual spectral signature from them. (c,d,e) is the abundance map from EM1, EM2 and EM3, respectively. The abundance map of EM4, which maps to the signature of the background, is not show.

The Spectral Unmixer was programmed in Python V 3.x. In order to find the endmembers and calculate their abundances, it uses a python implementation of the N-FINDR [206] and of the fully constrained least squares [207] algorithms, both provided by the PySptools Python package [208], a freely available Python library for hypespectral imagery analysis. The Spectral Unmixer was developed by: Hudson Miranda, Taiguara Tupinambás, Eduardo Ribeiro, Jailton Coelho and Cassiano Rabelo.

3.5.2   SOFTWARE FOR AUTOMATIC BASELINE REMOVAL & PEAK FITTING OF GRAPHENE'S RAMAN SPECTRA

The tools discussed so far for dealing with hyperspectral datasets can be considered easy to use and provide important feedback from a given sample, but they are limited in the granularity of the information they are able to extract. The range selection method used in the HSPE, for example, is based on an amplitude estimation, which, in a crude way, could be used to determine the peak amplitude and its position, but could fail in relevant situations, such as when two Raman bands overlap.

Three parameters are commonly used in Raman spectroscopy when referring to a certain Raman peak: its position, ω, its amplitude, I and its full width at half maximum, Γ. In graphene, for example, disorder gives rise to the D and the D' bands, as seen in Section 2.2.3. As shown in Figure 3.30, the aspect to consider here is that the G and D' bands orverlap, therefore, in order to extract individual parameters from each band, such overlap must be considered.

Due to the need of performing detailed Raman analysis, including the correlation of multiple bands from the same spectrum, a software
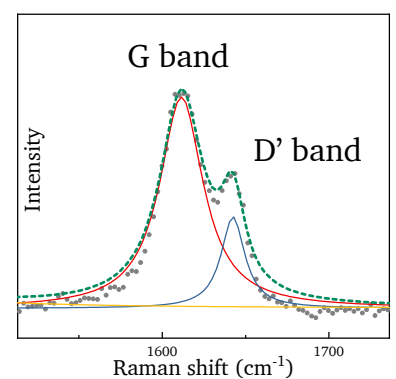
FIGURE 3.30: Graphene Raman spectrum showing the overlapping G and D' bands. The dots represent the original acquired data. The red and blue solid curves are the Lorentzian fit for the G and D' bands, respectively. The dashed green curve represent the sum of the two Lorentzians.
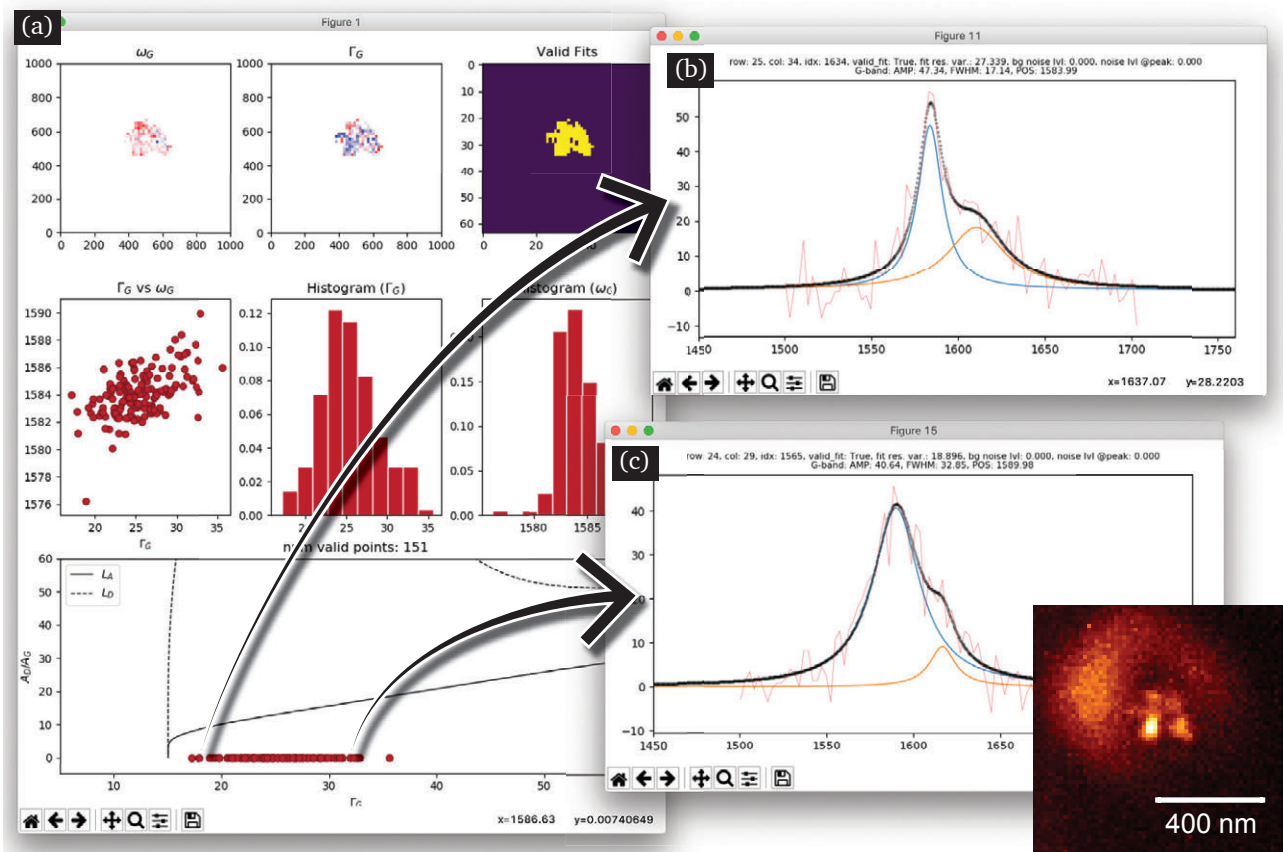
FIGURE 3.31: (a) Analysis window that is shown after the successful fit of a hyperspectral image dataset. In the top row is shown: image generated based on the ω_G and Γ_G values obtained from the fit, while the last image is a mask where the yellow pixels represent fits that passed the validation procedure. In the 2nd row we have a $\Gamma_G \times \omega_G$ plot, followed by histograms of the Γ_G and ω_G, respectively. In the last row is a plot of Γ_G as a function of A_D/A_G, but since in this batch run, due to user demand, the D band was not fitted, the data is placed at $A_D/A_G = 0$. By clicking on any of the fitted points in the analysis window (a), the window shown in (b) and (c) will be displayed, showing the actual Raman spectra and its related fit, allowing user a close inspection of the quality of the fit. The solid blue and orange curves represent the G and D' bands, respectively, while solid black curve represents the sum of both fits. The thin red curve represents the Raman spectrum as acquired.

[13]The Lorentzian function is the expected response from a damped harmonic oscillator subjected to an external force, in the limit of $\omega \gg \Gamma$

for automatic baseline removal and peak fitting in graphene based structures was developed. Since it has a focus on graphene, its fitting capabilities are limited to the D, G, D' and 2D Raman bands from single-layer to few-layer graphene samples. The software starts with four Lorentzian functions,[13] one for each band, centered according to theory [91, 92]. After automatically fitting the requested peaks, validation routines are performed where the fits that fail a given criteria, such as fitting parameters did not converge within desired values or peaks that show results incompatible with those foreseen by the Raman theory, will get automatically marked for exclusion. The software was developed in Python v.3.x and uses a number of routines from Peak-o-Mat [209], an open source software for peak fitting.

Figure 3.31 shows the result of running the software on a hyperspectral image dataset, where all the parameters from the four fitted bands can be obtained for thousands of spectra in one batch. With this

information available, meaningful graphs, such the relation between ω_G and ω_{2D}, which indicate the amount of strain and doping [69], as seen in Section 2.2.3, can be plotted. In Figure 3.31(a) is shown the analysis window that is presented after running the batch fitting process. The data in this example is from a hyperspectral scan in a $1 \times 1\,\mu\text{m}^2$ scan area containing a graphene nanoflake, as shown in the image at the bottom right corner, which was generated based on the intensity of the D band.

The analysis window provides the user with the opportunity to inspect the results and validate the quality of the automated fit that was performed. The 1st image in the top row of Figure 3.31(a) was generated based on the ω_G from the fitted data, while the 2nd image was generated based on the Γ_G. The 3rd image is the automatically generated mask showing the location (yellow pixels) of all the valid fits in the dataset. As one can see, based on the generated mask, the automated fit successfully disregarded most of the far-field contribution, which can be seen as a doughnut shaped halo around the nanoflake in the image at the bottom right corner of Figure 3.31.

The 1st plot in the 2nd row of Figure 3.31(a) shows Γ_G as a function of ω_G, while the 2nd and 3rd plots are histograms from Γ_G and ω_G, respectively. The plot in the last row is A_D/A_G as a function of Γ_G [81], but since, per user choice, the software did not fit the D band, the A_D/A_G value for every point is set to zero. Finally in Figure 3.31(b, c) we have the actual fit that gave rise to the points indicated by the arrows coming from Figure 3.31(a). The solid blue curve represents the Lorentzian fit of the G band and the solid orange curve represents the fit of the D' band. The black thick line represents the sum of both fits, while the red thin line represents the Raman spectrum as acquired. The user can access this additional inspection window by simply clicking in one of the points in Figure 3.31(a).

Such software was invaluable for the work presented Chapter 4, when hundreds of thousands of graphene spectra were fitted from a myriad of samples.

4

Research results

4.1 HIGH RESOLUTION IN GRAPHENE

The sample investigated here, as described in Section 3.3.2, is a mechanically exfoliated monolayer graphene that underwent a process in which defect lines were created by a highly energetic beam of helium ions. These ions were accelerated with an energy potential of 30 kV by a helium ion microscope (HIM). The analysis presented here is based on two hyperspectral image scans (HSI) acquired from the sample: one micro-Raman scan (far-field, FF) and a TERS scan (near-field, NF), both acquired on the same location and with the given parameters:

TABLE 4.1

HSI ACQUISITION PARAMETERS

	micro-Raman (FF)	TERS (NF)
Scan area	$1.28 \times 1.28\,\mu m$	$1.28 \times 1.28\,\mu m$
Number of pixels (w×h)	64x64	64x64
Integration time (sec.)	1	0.7
Laser power	$690\,\mu W \pm 3\%$	$95\,\mu W \pm 3\%$

The parameter differences have been considered in the analysis with the data being compensated accordingly, where each spectrum in the HSI is normalized by the integration time and laser power.

Figure 4.1 shows hyperspectral images generated from the intensity of the D, G and 2D bands, respectively, where Figure 4.1(a–c) corresponds to the micro-Raman scan (FF) and Figure 4.1(d–f) corresponds to the TERS scan (NF). The white arrows highlight two positions where the HIM beam traversed the sample, while the text
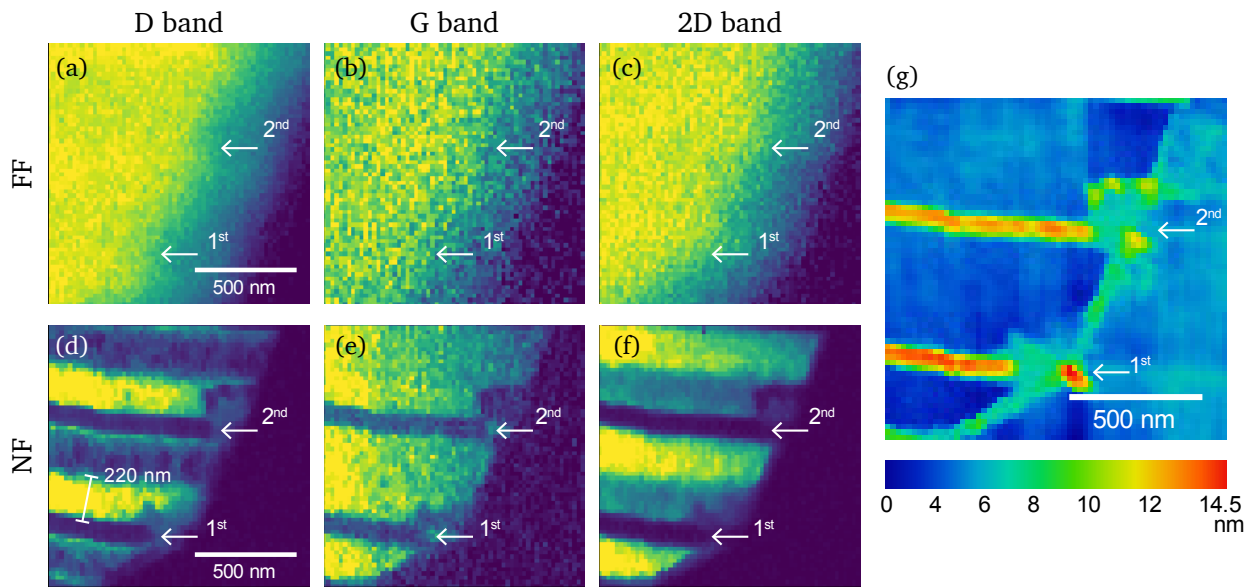
FIGURE 4.1: Images generated based on two hyperspectral image scans: one in the FF (1st row) and another in the NF (2nd row) regimes. The images were generated based on a selected interval corresponding to the D (a,d), G (b,e) and 2D (c,f) bands, as described in Section 3.5.1. The white arrows mark the location where the HIM beam traversed the sample and the order in which it did. The dimension line in (d) measures the width of the highly defective region. (g) AFM topography image acquired simultaneously with the HSI NF scan. The experiment was performed at Inmetro.

labels indicate the order in which it did. By comparing row FF and NF, it is clear that the micro-Raman scan, due to the diffraction limit, brought a limited amount of information from the sample at such small scale, with the images generated from each Raman bands showing an uniform distribution over the whole scanned area. The smooth effect at the border is expected due to the fact that, below the diffraction limit, the border cannot be spatially resolved.

Figure 4.1(d) corresponds to the mapped intensity over the selected spectral range equivalent to the D band, as described in Section 3.5.1, which was generated from the NF HSI. The image shows that there is a higher concentration of defects localized at only one side of where the HIM beam struck the sample and extending for ≈ 220 nm. It is interesting to note that such information is not present in the AFM topography image shown in Figure 4.1(g), which is limited to reveal elevations in the sample surface where the helium beam scanned the sample. Such elevations, known as nanotumefaction [210] (NT), is an indication that a high dosage of helium ions was used, which has the side effect of causing a sputtering effect, causing the swelling of the SiO_2 and the damaging of the graphene on the sputtered elevation.

Figure 4.2 presents perspective views generated from the AFM topography height data. The *faux* color in Figure 4.2(a) corresponds to the color coded height, as shown below the image, mapped on the 3D data. The cross section S1 is plotted in Figure 4.2(b) where the nanotumefaction, at the section location, reaches a height of almost

(a) AFM Topography

(b) S1

(c) D band

(d) 2D band

FIGURE 4.2: (a) Three-dimensional (3D) representation of the AFM topography acquired data, where the *faux* color is mapped to the height. The height in the Z-axis has been scaled, to facilitated the visualization, by $\times 100$ compared to the scale from the X- and Y-axis. (b) Plot from cross section S1 in (a) showing the nanotumefactions and the order in which they were created. (c,d) Same 3D topography shown in (a) but mapped to the surface of the 3D representation is the D and 2D band images shown in Figure 4.1(d,f), respectively. The illustrations at the bottom of (c,d) depict a view from cross section S2 showing the HIM beam at an angle $\theta = 45°$ as it strikes the sample. The red lines inside the SiO_2 substrate represent the secondary emissions.

12 nm in the first location and 9 nm in the second location.

The fact that the D band is not uniformly distributed on both sides of the nanotumefaction, combined with the AFM topography data, which shows an uniform elevation on both sides, indicates that the HIM beam struck the sample at an angle and not orthogonally to the sample plane. When helium ions collide with the sample, they cause secondary emissions and, due to this angle of attack, these secondary emitted particles damaged the monolayer graphene on the opposite side. Figure 4.2(c) depicts the same AFM topography, but color mapped with the intensity of the D band as taken from Figure 4.1(d). The two red arrows mark the positions where the D band is more intense. The illustration below the 3D images in Figure 4.2(c,d) depict a view from cross section S2 showing the HIM beam striking the sample at an angle $\theta = 45°$, where the red strikes represents the secondary emissions. In Figure 4.2(d) the AFM topography image is mapped with the intensity taken from the 2D band in Figure 4.1(f). It has been established that the intensity of the 2D band decreases in locations where the intensity of the D band is high [211], in agreement with the results observed here.

So far the analysis was based on the intensity of the Raman bands, but in order to characterize the sample from a disorder related perspective, such as has been done in [81] and discussed in Section 2.2.3, a proper fit of the Raman spectral bands was performed in both the FF and NF HSIs, using the software described in Section 3.5.2.

Figure 4.3(a,c) is a plot of $A_D/A_G \times \Gamma_G$ for both NF and FF, while in Figure 4.3(b,d) the color of the pixels is given by the associated color that such spatial location has on Figure 4.3(a,c). The gray pixels

FIGURE 4.3: (a, c) Plot of the area of the D, A_D, over the area of the G, A_G, Raman bands as a function of the G band FWHM, Γ_G. The Raman bands were fitted from the HSI scans obtained in the FF and NF, respectively. Given the color of a point in (a), the same color was use to color the pixel in (b), given that it was from this pixel that the spectra used to generate the point in (a) was acquired. The same logic applies to (c, d). (e) Plot of the line profile S1 located in the transition from a highly defective area to an area with a lower amount of defects as highlighted in (d), where the blue dots corresponds to the line profile and the red curve corresponds to converged fit using a Boltzmann bent step function (BBSF). (f) is a joint plot of both (a) and (c), where the green dots correspond to the FF and the red dots correspond to the NF. $X1$ marks the center of mass of the FF data distribution, while $X2$ marks the center of mass of the NF data distribution.

(background) correspond to spectra that did not pass the validation routines after the fitting algorithm, which automatically identifies the presence or absence of the D and G Raman peaks. The black arrows point the same locations marked by the white arrows in Figure 4.1. Figure 4.3(a,b) does not show any obvious spatial correlation, contrary to what happens in (c,d), where it is evident the existence of a highly defective area neighboring only one side of the nanotumefactions. In order to determine the width of the transition from this highly defective area to an area containing a lower amount of defects a line profile was extracted at the location indicated by S1 in Figure 4.3(d) and plotted in Figure 4.3(e). The curve was then fitted with a Boltzmann bent step function (BBSF), which is given by

$$ f(x) = y_0 + \frac{h}{2}\tanh\left(\frac{\xi}{W}\right) + \alpha\xi + \beta\xi^2, \ \xi = x - x_0 \, , \qquad (4.1) $$

where W corresponds to the width. The regression converged with the following values: $x_0 = 123.57 \pm 1.5$ nm, $y_0 = 72.73 \pm 1.2$ nm, $W = 30.04 \pm 3.3$ nm, $h = -89.39 \pm 6.6$ nm, $\alpha = 44.62 \pm 31$ μm^{-1}, $\beta = 95.95 \pm 117$ μm^{-2}. Based on the value of $W = 30.04 \pm 3.3$ nm,
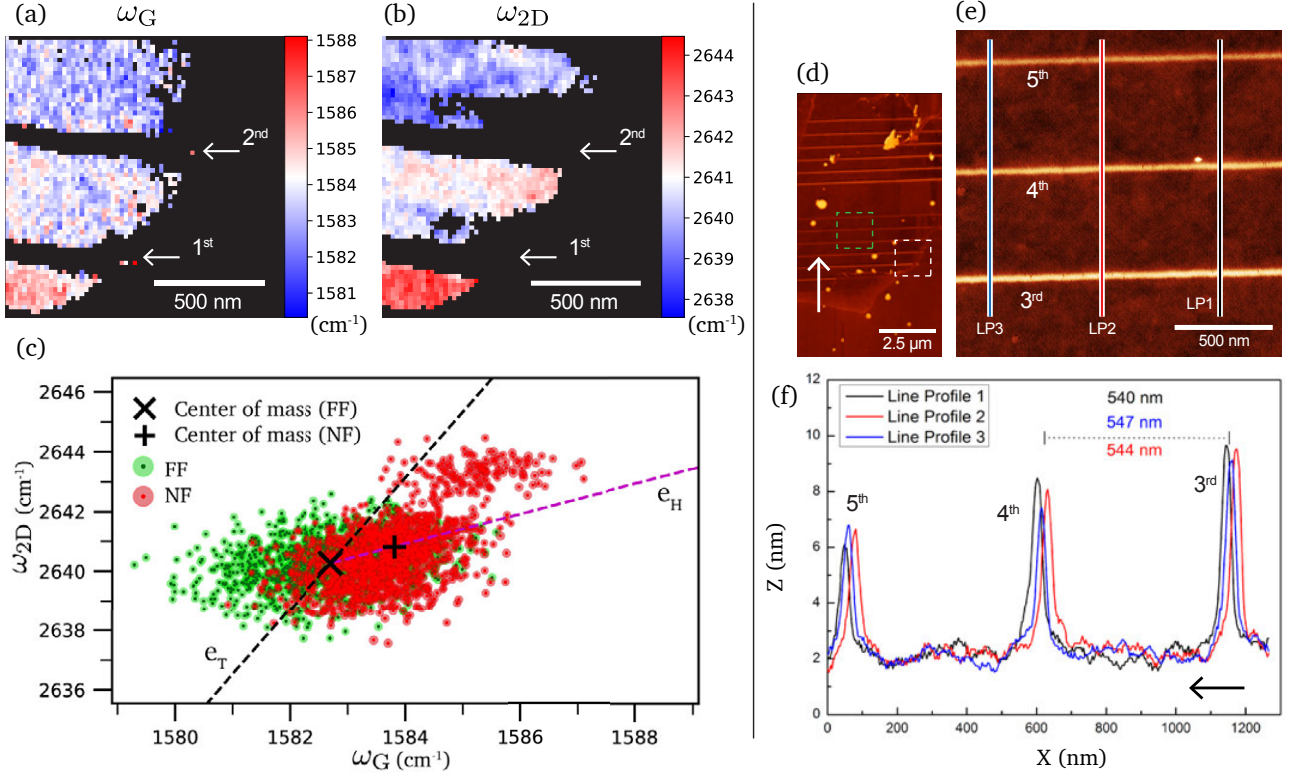
FIGURE 4.4: HSI images generated from the position of the G (ω_G)(a) and 2D (ω_{2D})(b) bands, respectively. The white arrows mark the location where the HIM beam traversed the sample, while the text labels indicate the order in which it did. (c) Plot of $\omega_G \times \omega_{2D}$ as in [69], with the direction vectors e_T and e_H, which correspond to strain and doping respectively. The "X" and "+" marks the center of mass of the FF and NF distribution, respectively. By moving the e_H vector to the center of mass of the FF, it becomes clear that the NF center of mass moved in the doping direction. (d) AFM topography image where additional HIM patterned lines can be seen. The white arrow points to the direction on which the lines were produced. The white dashed square represent the location from where the HSI data has been acquired, while the green dashed square corresponds to the location where another AFM topography image was taken, which is shown in (e) and encompasses three additional patterned lines, labeled 3rd, 4th and 5th, based on the fact that, given the direction in which the patterning took place, they were made after the two ones inside the HSI area. (f) shows three line profiles taken from the black, red and blue lines shown in (e) and labeled (LP1, LP2, LP3), respectively. The black arrow points the order in which the nanotumefactions were produced.

it is safe to say that the actual width of the transition from this highly defective area to an area containing a lower amount of defects is significantly smaller then the optical resolution achieved, which is equivalent to the tip's apex diameter, as measured through SEM.

In Figure 4.3(e) we plot both FF and NF points on the same $A_D/A_G \times \Gamma_G$ graph. The points $X1$ and $X2$ are located in the center of mass of FF and NF data distribution, respectively. It is important to note that although the value of Γ_G is approximately the same ($\Gamma_G \approx 21\,\mathrm{cm}^{-1}$), the A_D/A_G value is significantly different.

Such discrepancy in the location of $X1$ and $X2$, the centers of mass, contradicts a common sense expected result, where the normalized average of all spectra from the NF and FF based on data acquired from the same location and similar experimental conditions, should yield similar results, which is clearly not the case. This will be further explored in Section 4.2.

The TERS HSI exploration revealed yet another collateral effect resultant from the HIM procedure. Figure 4.4(a,b) shows two images generated based on the frequency of the G and 2D bands, ω_G, ω_{2D}, respectively, where it is observed a shift in the position of both Raman bands along the image's vertical direction, as shown by the color variation. Figure 4.4(c) plots ω_G as a function ω_{2D}, which is a clear indication that, according to [69] and as discussed in Section 2.2.3, the graphene sample was doped during the milling process that generated the patterned defect lines. Such finding explains why the height of the nanotumefaction presented, on each consecutive line, a decrease in its height, as shown by the line profile in Figure 4.4(f), where the black arrow points in the direction the process took place. Based on the exposed information, it is considered that during the milling process, the graphene sample became more and more positively charged, which caused a decrease in the kinetic energy of the He^+ ions at the moment of interaction with the sample, consequently reducing the nanotumefaction effect as the experiment progressed. It is also relevant to observe that the TERS data shows different doping characteristics, when compared to the micro-Raman acquired data, as shown in Figure 4.4(c).

Such findings would not come easily with other microscopy techniques, specially in such a non-invasive way, which show the importance of Raman spectroscopy beyond the diffraction limit and the relevance to industry related processes and metrology.

4.2   NEAR-FIELD INTERFERENCE: TIP-APPROACH ON G VERSUS 2D BANDS

As discussed in Section 2.3, Raman scattering in the far-field regime is assumed to be a spatially incoherent process, whereas in the near-field regime spatially coherent processes have to be considered, and the TERS enhancement factor depends on the symmetry of the vibrational modes [35, 36]. Therefore different symmetries show different enhancements due to interference effects. In order to explore such phenomena, a series of TERS analysis during tip-approach procedures were performed. First on an exfoliated monolayer graphene sample, with a pristine crystalline structure, then on a graphene nanoflake, which, as already discussed in Section 3.3.1, is highly disordered.
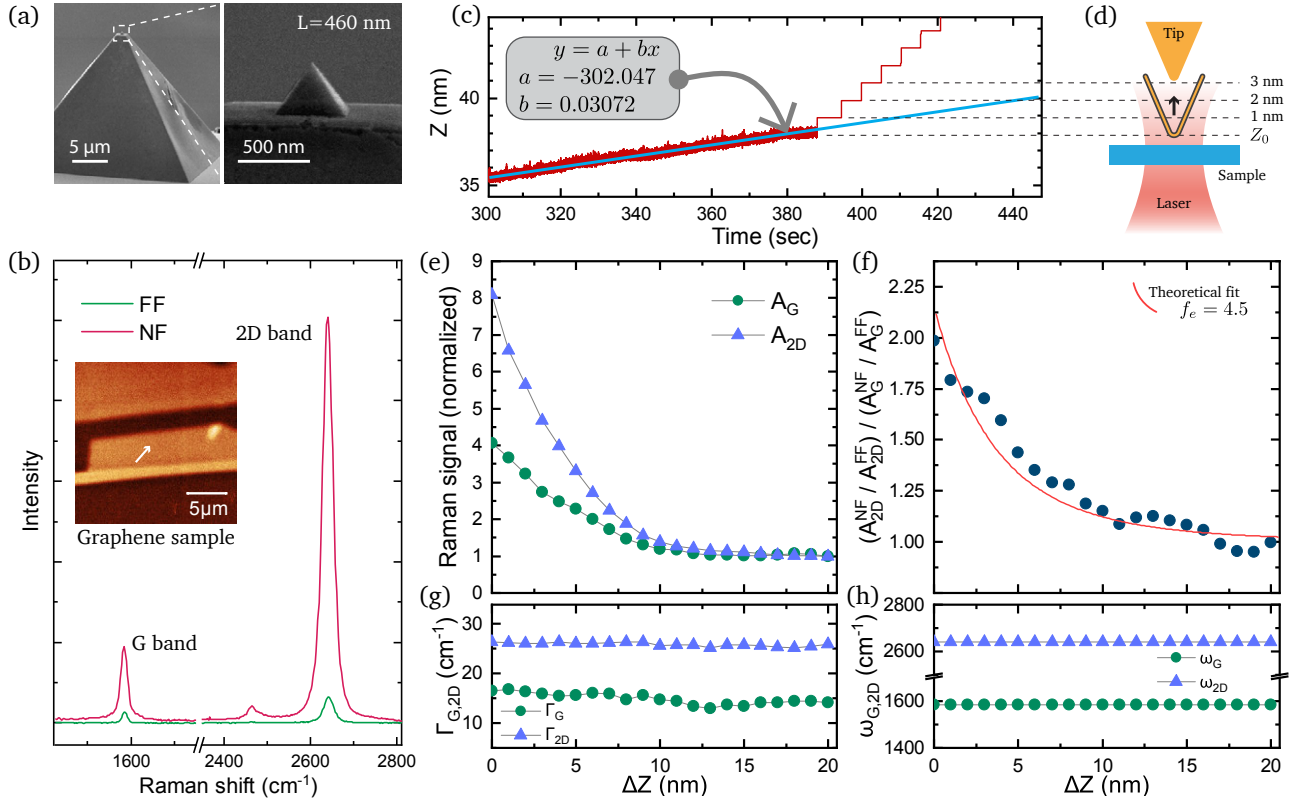
FIGURE 4.5: (a) SEM image taken from the PTTP used in the experiment ($L = 460$, $r_{\text{tip}} \approx 20\,\text{nm}$) (b) Raman spectrum acquired with (red) and without (green) the presence of the tip. The inset is a 2D band APD image of the sample, where the tip of the white arrow points the approximate location where the experiments on this sample took place. (c) Fragment of the logged data showing the tip's position along the z-axis (vertical) as a function of time. From 300 to 390 s, the tip was being controlled by the feedback loop, thus constantly moving vertically as to respect the configured set point. The slight inclination of the curve indicates a constant vertical drift, common in SPM. The blue line is the linear fit from which the drift speed can be assessed. The equation, as well as the fit values are shown inside the gray box. The slope parameter (b) indicates a vertical drift of $0.03\,\text{nm s}^{-1}$. At approximately second 390 the actual tip-approach procedure took place, which is indicated by the stepped appearance. From this point onwards the tip moves up by 1 nm, holds this position for 5 s and repeats the procedure. The upwards movement of the tip is depicted in (d). (e) Plot of the area of the G (green circles) and 2D (blue triangles) bands as extracted from the fitted spectra as a function of the tip distance. The data was normalized by the area of each respective band as acquired at $\Delta Z = 20\,\text{nm}$. (f) Plot of A_{2D}/A_G normalized by the far-field acquired spectrum. The solid red curve is the theoretical fit according to [35] which results in a enhancement factor of $f_e = 4.5$. (g,h) Plot of $\Gamma_{\text{G, 2D}}$ and $\omega_{\text{G, 2D}}$, respectively, as a function of tip distance.

Figure 4.5(a) shows a scanning electron microscopy (SEM) image of the PTTP used for the experiment. It has an $L = 460\,\mathrm{nm}$ and a tip apex radius $r \approx 20\,\mathrm{nm}$, according to SEM measurements. In order to assess the working quality of the PTTP and to assert that the laser and tip are correctly aligned, a Raman spectrum with a $100\,\mathrm{s}$ acquisition time and with the tip interacting with the sample was acquired. The tip was then fully retracted, which took it to a distance of $\approx 700\,\mathrm{nm}$ from the sample surface. Such distance corresponds to approximately two orders of magnitude away from the near-field emission range, therefore the acquired spectrum presents only far-field contribution. With the tip in this retracted position, another spectrum is acquired with the same acquisition parameters. Figure 4.5(b) shows a combined plot of the acquired spectra, where the red curve is the result with the presence of the tip (NF), while the green curve is the result with the tip retracted, therefore without the presence of the tip (FF). The inset shows a 2D band APD image where the white arrow points to the approximate location of where this and the following procedure took place. Figure 4.5(c) shows a fragment of the data log responsible for monitoring the position of the tip along the z-axis. In this graph, the x-axis is the time reference, while the y-axis corresponds to the vertical position of the tip. From second 0 (not shown), up to second 390, the tip was left interacting with the sample, thus the feedback control system is constantly working to keep it within the configured set point and, for this reason, the graph curve has a noisy aspect. At approximately second 390, the actual tip-approach procedure started, which consisted in: move the tip 1 nm away from the sample; acquire a 5 s spectrum; repeat. The step like waveform in Figure 4.5(c) shows the time evolution of the distance traveled by the tip. It is relevant to point-out that as soon as the tip-approach process starts, the feedback loop is turned off, which explains the disappearance of the noisy signal right after second 390, where the tip is no longer trying to maintain its interaction with the surface. The linear fit in Figure 4.5(c) shows that the system presented a vertical drift of $\approx 0.03\,\mathrm{nm\,s^{-1}}$, which does not impact the outcome of the experiment considering its time scale. Figure 4.5(d) is a depiction of the tip-approach process for better understanding.

Figure 4.5(e) is a plot showing the integrated areas of the G band (green circles) and 2D band (blue triangles) of the graphene sample as a function of the tip distance, normalized by the area of each respective band at $\Delta Z = 20\,\mathrm{nm}$[1]. As shown, the enhancement of the 2D band with the presence of the tip is approximately twice the enhancement exhibited by the G band, with such difference decreas-

[1]$\Delta Z = 0$ corresponds to the tip interacting with the sample. The actual distance, as previously discussed, is not trivial to assess, but it is commonly considered to be $\approx 5\,\mathrm{nm}$ [35].

ing as the tip/sample distance increases. As already pointed out, the difference in the observed enhancement between these graphene Raman bands can be explained by the symmetry difference between G and 2D bands [35, 36].

Figure 4.5(f) is a plot of A_{2D}/A_G, normalized by the far-field. The solid red curve is the theoretical fit according to [35], which considers near-field interference effects for the modes with different symmetries (E_{2g} for the G band and A_{1g} for the 2D band). The phonon coherence length, ℓ_c, was fixed as $\ell_c = 45$ nm, according to previous experimental results [183]. A tip radius, $r_{tip} = 20$ nm, as measured by SEM was also fixed. The only fitting parameter was the enhancement factor of the tip, found to be $f_e = 4.5$. Given by the quality of the fit, it is possible to say that the experimental result is very consistent with the theoretical expectations.

Finally, in Figure 4.5(g,h) we show that, during this tip-approach procedure, neither $\Gamma_{G, 2D}$ nor $\omega_{G, 2D}$ presented significant change, as expected.
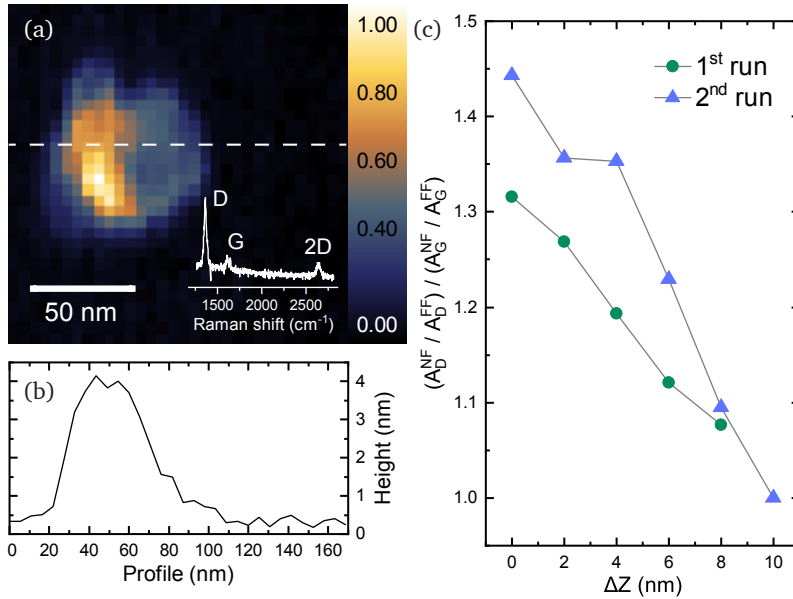
FIGURE 4.6: (a) Abundance map generated from an endmembers extracted by the unmixing software (Section 3.5.1). The white spectral signature on the inset corresponds to the endmember used to generate the abundance map, whereas the color scale corresponds to its contribution to each pixel. The scan was performed over a 170×170 nm area. (b) Line profile extracted from the AFM topography data (not shown) at the location indicated by the white dashed line in (a). (c) A_D/A_G plot from two independent tip-approach procedures performed within a few minutes window apart and on the same location, with the same tip/laser power/acquisition time.

Given that the D and the 2D bands present the same totally symmetric ($A_{1}g$) mode, it is expected that the D band should exhibit the same near-field interference properties as the 2D band, therefore, a tip-approach was performed on a graphene nanoflake. The sample was prepared as described in Section 3.3.1 and the scan was acquired from a 170×170 nm area, which is $\approx 2\times$ smaller than the diffraction limit. Figure 4.6(a) shows an abundance map generated from the endmember whose spectral signature is shown in the bottom right corner, over the image. The color bar represents the contribution of

this endmember in the generated image. Figure 4.6(b) is a line profile taken from the AFM topography data (not shown) at the position indicated by the white dashed line in Figure 4.6(a). Two tip-approach procedures were carried out. In both of them the tip was retracted as far as 14 nm, but the acquired spectra were only in condition to be fitted up to 10 nm. After this point, the Raman signal from the nanoflake was so weak that an excessively long time would be needed to acquire it and, as previously explained, due to vertical drift, the data would not correspond to the actual expected distance, which would jeopardize the analysis. Figure 4.6(c) is a A_D/A_G plot from both tip-approach procedures. It is important to note that, although both were acquired within a few minutes interval and with the same acquisition parameters and laser power, the enhancement in the 2nd run was $\approx$10 % better. It is not uncommon to see such variations when working in the nanoscale, where drifts in the order of a few nanometers can significantly impact the perceived enhancement. Despite the slight difference between both runs, the predicted behavior was experimentally proven, where vibrational modes with different symmetry, such as G and D/2D bands, due to interference related effects, present different enhancement factors in the near-field regime. This result explains why the data center of mass $X1$ and $X2$ in Figure 4.3(e) did not coincide, and this aspect will be further explored in the next section.

4.3 DEFECT CHARACTERIZATION WITH TERS

Considering that the D/G ratio is regarded as extremely important for Raman based metrology of defects in graphene related structures, the fact that this ratio changes due to interference related effects shows that a parameterization work is needed in order to understand how micro and nano-Raman can be used, consistently, to quantify defects in graphene related systems.

Here we present results based on a comparison between micro and nano-Raman spectroscopy performed on three distinct selected graphene nanoflakes, and with different tips, in order to evaluate how the enhancement factor impacts the results. The sample was prepared as discussed in Section 3.3.1 and the results are based on the analysis of the HSI data acquired. Relevant scan information is provided in Table 4.2.

Table 4.2: HSI scan information

Data (micro and nano)	Scan area (nm^2)	# lines	Pixels/line	Pixel size (nm)	Spectra count
Flake-A	700×700	64	64	10.9	8,192
Flake-B	1000×1000	64	64	15.6	8,192
Flake-C	1500×1500	64	64	23.4	8,192
				Total # spectra	24 576

Figure 4.7 presents the three selected nanoflakes, one per row. The first column (Figure 4.7(a)) shows the images generated based on the spectral range of the graphene's D band, as extracted from the FF HSI, while the second column (Figure 4.7(b)) shows the images generated based on the same spectral range as Figure 4.7(a), but extracted from the NF HSI. The third column (Figure 4.7(c)) shows the AFM topography image, which was acquired simultaneously during the NF HSI scan procedure. Finally, the fourth column (Figure 4.7(d)) shows the amorphization diagram, as discussed in Section 2.2.3, of each nanoflake, with the FF (green circles) and NF (red circles) data being shown on the same plot.[2] These plots clearly show that, each nanoflake shows distinct deviations on the center of mass of the data acquired in the NF and FF regimes, with Flake-A showing the largest deviation and Flake-C showing the smallest. Based on the contrast observed in the TERS images (Figure 4.7(c)), we anticipate that the deviation is larger for experimental data obtained with higher levels of field enhancement taking place.

The concept of using the D/G ratio in the form of an amorphization diagram was proposed in [81] as a way to characterize defects in

[2]Each point in the plot originated from a Raman spectrum acquired during the HSI scan, but only the points that passed the automatic fit validation ended up in the plot.

(a) micro-Raman (FF)   (b) TERS (NF)   (c) Topography   (d) Amorphization diagram
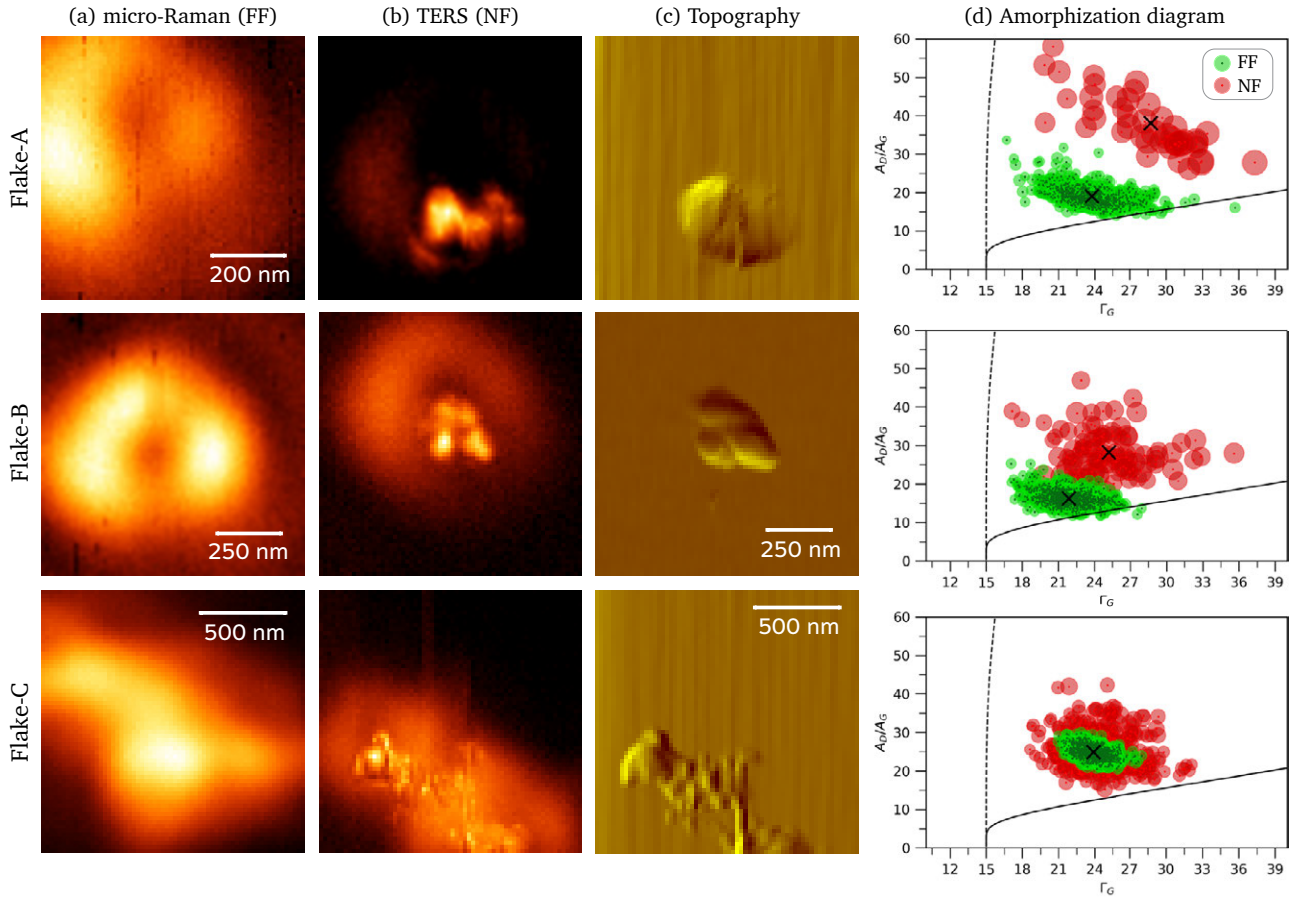
FIGURE 4.7: Image containing the three analyzed nanoflakes, one nanoflake per row. The first (a) and second (b) columns show images generated from the FF and NF HSI data, respectively, based on the intensity of the D band. The third column is the AFM topography image acquired during the TERS scan, thus simultaneously with the optical images shown in column (b). The fourth column (d) is the amorphization diagram $(A_D/A_G \times \Gamma_G)$, as proposed by [81], where the green circles correspond to the FF, while the red circles correspond to the NF.

graphene based structures provided that the type and amount of defects were previously known, and the properly characterized samples underwent a methodical micro-Raman spectroscopy characterization. Such approach is valid to the FF, but in the NF regime, as we have shown, the proposed protocol can no longer be utilized directly, being a correction factor needed in order to account for interference based effects, which are directly related to the enhancement factor [36].

There is a well defined dependency [35] between the (G+2D) spectral intensity and the (2D/G) ratio with f_e, as shown by Eq. (2.15) and Eq. (2.16). Based on these equations, considering that both D and 2D bands share the same vibrational modes and that α, γ and δ are constants, we have

$$D/G = A_0 f_e^2 \qquad (4.2)$$

$$D + G = A_1 f_e^4 + A_2 f_e^2 . \qquad (4.3)$$

The solution to this system results in the following dependency

$$D/G = \alpha + \beta(\sqrt{1 + \gamma(D+G)} - 1) , \qquad (4.4)$$

where $\alpha = A_0 A_2 / 2A_1$ and $\beta = 4A_1/A_2^2$. This equation is important as it provides a correction factor that applied to the A_D/A_G ratio
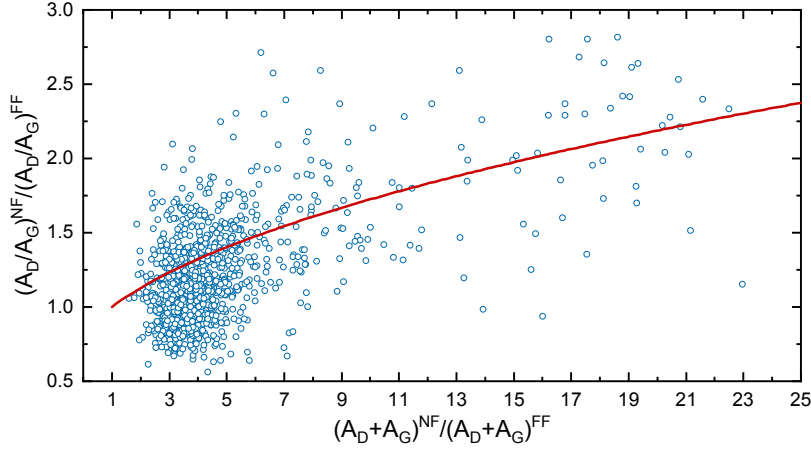
found in a NF measurement, for a given spectral enhancement $(A_{\mathrm{D}} + A_{\mathrm{G}})^{NF}/(A_{\mathrm{D}} + A_{\mathrm{G}})^{FF}$, the given NF acquired data can then be used to correctly characterize the existing defects based on the already well-established protocols for the FF.

Figure 4.8 shows a scatter plot of $A_{\mathrm{D}}/A_{\mathrm{G}}$ as a function of $A_{\mathrm{D}} + A_{\mathrm{G}}$, where the NF data was normalized by the FF values. Different from the experiment in Figure 4.5(f), where the enhancement of a given tip with $f_e = 4.5$ is changed by changing ΔZ, here ΔZ is fixed with $Z = Z_0$.

The solid red curve in Figure 4.8 is the fit result of Eq. (4.4), where the regression converged with the following values: $\alpha = 0.814, \beta = 0.254$ and $\gamma = 1.999$. It is important to notice that the theoretical curve follows a field enhancement trajectory, as larger values of $(A_{\mathrm{D}} + A_{\mathrm{G}})^{NF}/(A_{\mathrm{D}} + A_{\mathrm{G}})^{FF}$ or $(A_{\mathrm{D}}/A_{\mathrm{G}})^{NF}/(A_{\mathrm{D}}/A_{\mathrm{G}})^{FF}$ corresponds to larger enhancement factors f_e.

Such approach is able to provide a valid parameterization for the $(A_{\mathrm{D}}/A_{\mathrm{G}})^{NF}$, mapping it to a valid $(A_{\mathrm{D}}/A_{\mathrm{G}})^{FF}$ value, which covers the y-axis of the amorphization diagram.

4.4 TIP-ENHANCED RAMAN SPECTROSCOPY OF GRAIN BOUNDARIES IN GRAPHENE

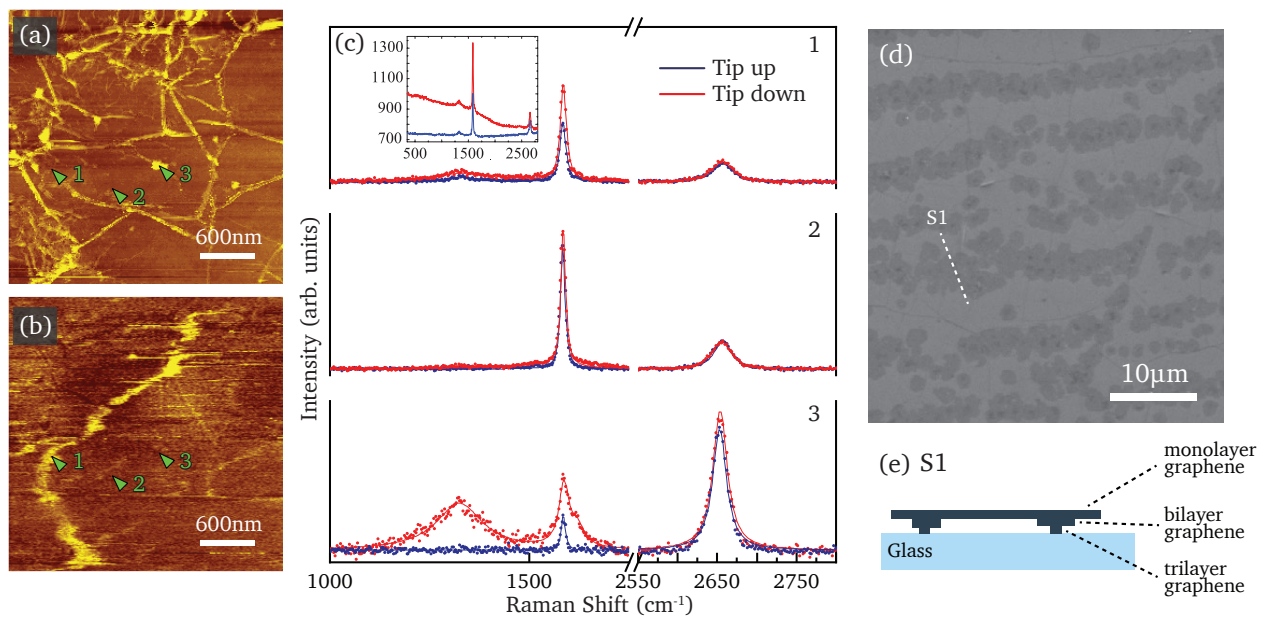FIGURE 4.9: Simultaneous STM (a) and TERS (b) images acquired from the CVD grown graphene sample. For the TERS imaging with the APD, a filter for the D band was used. (c) Raman spectra at 3 different locations marked in (a, b) by the numbers 1, 2, and 3, after background subtraction. The red spectra correspond to the NF acquired data, while the blue spectra corresponds to the FF. The inset in (c-1) shows the spectra from point #1 over a larger spectral range, without background subtraction. (d) SEM image from the CVD grown graphene sample showing showing the location of a hypothetical cross section.(e) Cross section sketch depicting how the graphene layers are stacked in relation to the glass coverslip (not in scale). (a–c) are adapted from [212]). SEM image in (d) was provided by our collaborators from Aalto University.

All results discussed up to this point where obtained with the TERS system working in the AFM mode. Here we report experimental results obtained with the STM-TERS system, as described in Section 3.1 and Section 3.2, on the sample described in Section 3.3.3.

The STM image shown (Figure 4.9(a)) reveals that the sample has a polycrystalline structure with a high number of domain boundaries [151], which is indicated by the bright yellow lines.

The TERS image from the G band (Figure 4.9(b)) shows features that indicate that near-field information was collected. To better illustrate the TERS enhancement, a total of three tip up/down spectra were taken on the positions marked on Figure 4.9(a, b). The results in Figure 4.9(c) show that there was tip-induced enhancement at points 1 and 3. Point 3 is of special interest, given that it appeared as a high intensity location in the STM image (Figure 4.9(a)) and the defect-induced Raman signature, as shown by the presence of the Raman D and D' bands, is only observed when the TERS tip is landed on top of this spot. Without the presence of the tip, the dominant Raman signal comes from the far-field, therefore originating from a much larger area in which the graphene sample is mostly pristine, thus the presence of defects is negligible. When the tip is landed on top of the defect, the defect-induced signal is locally enhanced and becomes dominant in the Raman spectrum, as shown in the tip up/down in

Figure 4.9(c-3). Through similar reasoning, one can conclude that point 1, due to the absence of defect-induced Raman signature, is not actually a graphene grain boundary, but originating from a strong photoluminescent background, which is clearly visible in the inset of Figure 4.9(c), where the original acquired Raman spectrum, without any baseline removal is shown. The STM topography images did not reveal any bilayer or higher number of layer in the samples, contrary to what was revealed through the Raman signal, indicating that those visible islands in Figure 4.9(d) are in fact under the single-layer graphene as depicted by the sketch in Figure 4.9(e).

The results obtained with the STM-TERS show that we are able to have spectroscopic information from grain boundaries in graphene, which is relevant to a diverse number of industries, such as metallurgy, coating and semiconductor applications.

4.5   RAMAN SPECTROSCOPY OF SUSPENDED GRAPHENE SUBMITTED TO TIP-INDUCED STRAIN
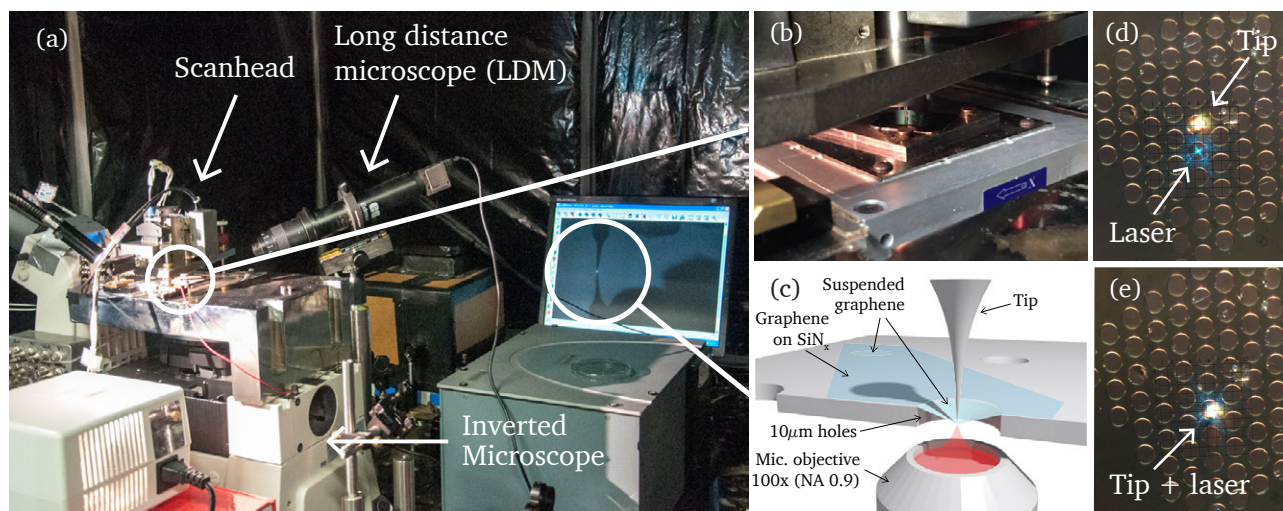

FIGURE 4.10: (a) The TERS system as configured to perform the experiments. (b) Sample as seen through the naked eye from the side. (c) Schematic view of the system. (d, e) Images of the sample as seen through the microscope eyepiece, showing the holes where the graphene sample is suspended. (d) Image showing the SPM tip (yellow) and laser spot (blue) misaligned and (e) after alignment.

Finally, the TERS probe can be utilized not only for local field enhancement, but for perturbing the sample locally in a controlled way. Here we report experimental results of using the TERS system to perform nanomanipulation experiments while acquiring Raman spectroscopy data from the sample simultaneously with the manipulation process. The objective was to characterize, through *in situ* Raman spectroscopy, the mechanical properties of suspended graphene subjected to tip-induced mechanical strain.

The sample, as described in Section 3.3.4, contains graphene layers suspended over micrometer sized holes. Due to the nature of the sample, we chose to use AFM as the SPM technique, where the AFM probe is used as a nanoindentation device capable to induce localized strain in the suspended graphene membranes. The microscope objective used was an air objective with NA= 0.95 and 100x magnification, given that, due to the presence of multiples openings in the substrate where the graphene membrane stays suspended, oil immersion was not an option.

For this experiment, SiO_x tips fabricated locally were mounted on the tuning fork. SiO_x tips were preferred not only due to the hardness of the material, but also due to the much cheaper fabrication cost and easiness of assembly when compared to a PTTP tip. The excitation came from a 488 nm wavelength laser. Figure 4.10(a) shows a picture of the setup with the scanhead on top of the nanopositiong stage and the long distance microscope used to locate the AFM probe on top of the sample. Figure 4.10(b) is a closer view of the scanhead

and the sample underneath. Figure 4.10(c) is a sketch of how the experiment is setup. Figure 4.10(d, e) show two steps in the tip/laser alignment process, with (d) showing the tip and laser misaligned and (e) aligned.

In Figure 4.11 we present the Raman spectra acquired from a bilayer suspended graphene in three moments: without tip-induced strain and submitted to two levels of tip-induced strain. The green spectrum was obtained without the presence of the tip (tip-up). As the tip pushes the suspended graphene membrane (tip-down and tip-down (harder)) we observe an increasing redshift of the G and 2D bands (blue and red spectra, respectively). As mentioned in Section 2.2, this G and 2D band frequency shift is a clear indication of strain and based on the shift amount, the magnitude of the strain can be derived [69]. The red spectrum shows the G band splitting in two sub-bands named G^+ and G^- [168].
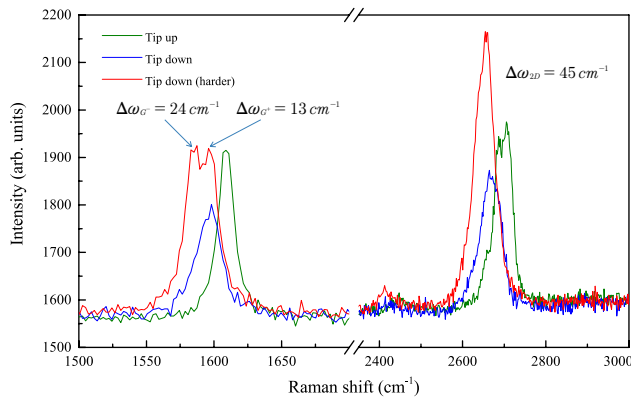
FIGURE 4.11: G and 2D band Raman spectra for three different applied strain in bilayer graphene. The changes in frequency for the red trace (higher strain) with respect to the green trace (no strain) are provided.

In order to assess wether the graphene would behave differently under a sequence of loading and unloading, a series of experiments were performed where we progressively increased (loading) and decreased (unloading) the nominal probe-strain applied (Figure 4.12(a,b,c)). A nominal probe-strain of zero represents the initial condition, where the probe, through the AFM control system, was lowered to the surface until it minimally interacted with the sample surface and was positioned approximately in center of the hole containing the suspended graphene under study, while the feedback system was operational and acting to keep the probe from crashing and consequently keeping it from pushing the graphene membrane. To guarantee the smallest interaction possible, Raman spectra were acquired and compared with and without the presence of the probe interacting with the sample surface. The results showed that there was no measurable band frequency shift when the probe was lowered to the sample with the feedback system turned on and using a setpoint of 1.1 Hz; higher setpoint values have not been tested.

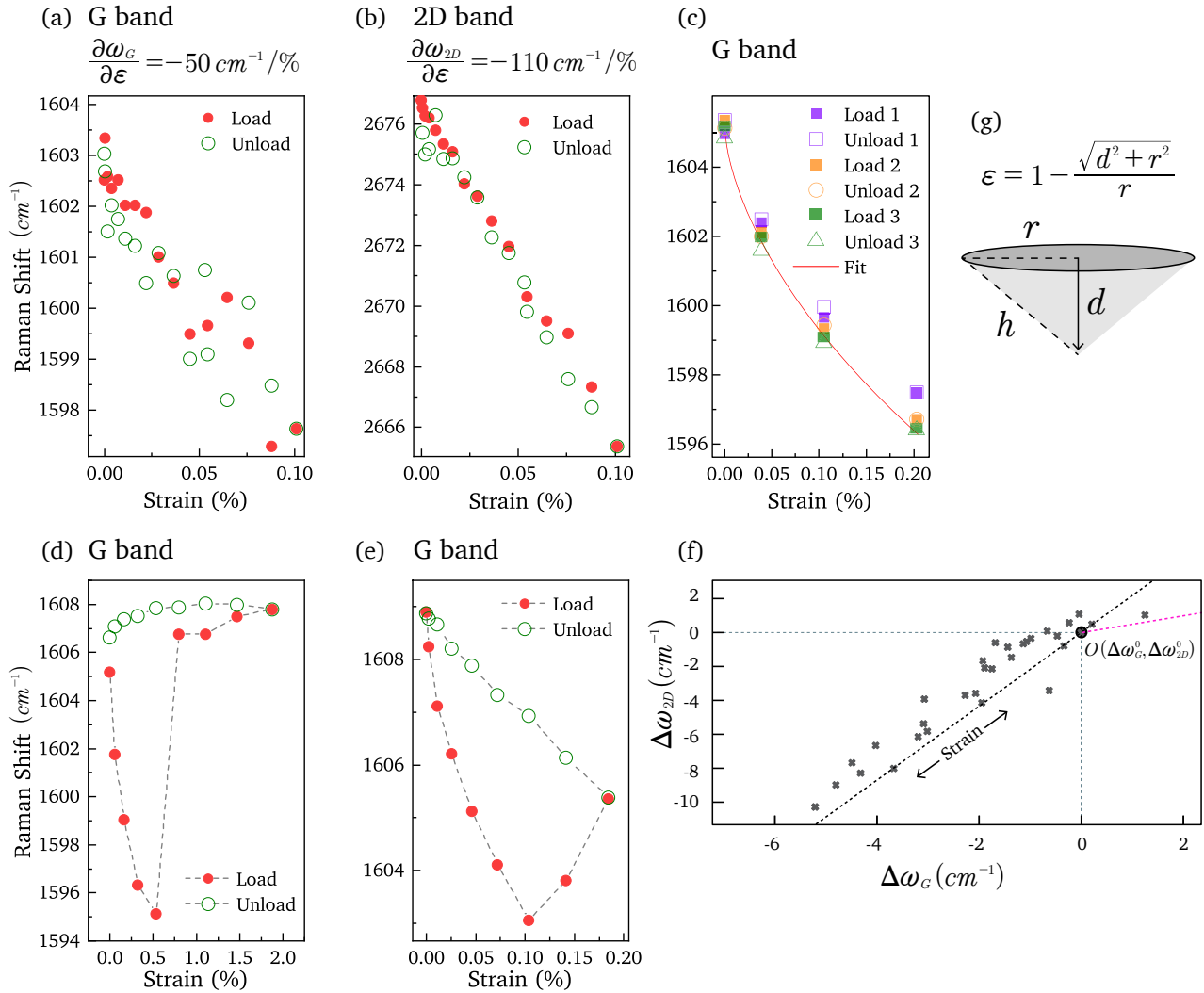FIGURE 4.12: Results obtained from a series of tip-induced strain experiments. The filled shapes represent strain loading, while the hollow shapes represent strain unloading. In (a) and (b) we show plots of the ω_G and ω_{2D} respectively, taken simultaneously from the same load/unload procedure on which a nominal strain of $\approx 0.1\%$ was applied. In (c) the ω_G results from three load/unload experiments in the same hole as (a,b), but this time reaching a nominal strain of $\approx 0.1\%$. In (d) we have a ω_G from the same hole, but this time with a strain up to $\approx 2.0\%$. It is clear that a slip occurred at $\approx 0.5\%$. In (e) we have yet another ω_G plot, but from a different hole and with an applied strain up to $\approx 0.2\%$. This time a slip occurred at $\approx 0.1\%$. (f) Lee *et al.* [69] like plot showing the correlation between the frequencies of the G and 2D Raman modes of graphene (ω_G, ω_{2D}). The black circle at (0,0) represents the initial point of the experiment, before any tip-induced strain was applied. The black dashed line represents the strain vector of (ω_G, ω_{2D}), considering the sample is charge-neutral, while the magenta dashed line represenetes the doping vector, considering the sample is strain-free. (g) the equation and geometrical representation of a radially applied strain. Plots (d, e) are adapted from [212].

Based on the geometry of the sample Figure 4.12(g), in order to calculate the percentage of applied strain, the following equation can be used

$$\varepsilon = 1 - \frac{\sqrt{d^2 + r^2}}{r} \ , \qquad (4.5)$$

where r corresponds to the radius of the hole (in our case $10\,\mu\text{m}$) and d corresponds to the vertical distance traveled by the probe (Figure 4.12(g)).

The tip-induced strain procedure goes as following: A reference Raman spectrum is taken without the presence of the probe. With

the probe retracted, but already aligned to the center of the graphene membrane, the AFM feedback is turned on and the probe is released. As the probe approaches and interacts with the sample surface, another reference Raman spectrum is taken. A series of load/unloading then takes place through an automated procedure that works similarly to a tip-approach, but in the opposite direction, where the probe presses the surface, instead of moving away from it, therefore straining the graphene membrane in a known and controlled manner. At each step a Raman spectrum is taken and stored for later processing. This is repeated until the desired travel distance is reached, from which a known amount of strain can be derived given Eq. (4.5). The procedure then runs in reverse mode, retracting the probe by the same distance at each interaction and acquiring a Raman spectrum each time, until it is back to its starting position.

Initially we performed the procedure limiting the applied nominal strain to $\approx 0.1\%$, , indicating a different graphene-substrate adhesion force. In Figure 4.12(a) and (b) we have the plots of ω_G and ω_{2D}, respectively, from this first load/unload routine, which comes to shows that the process was fully reversible and without perceivable changes in the mechanical properties of the graphene. After that, the procedure was repeated three more times on the same membrane covered hole, but this time applying a nominal strain up to 0.2% (Figure 4.12(c)). It is clear that the process was still fully reversible and without perceivable changes in the mechanical properties of the graphene.

Figure 4.12(d) presents a forth load/unload procedure performed on a different hole, but now reaching a nominal strain up to $\approx 2\%$. It is clearly noticeable an abrupt change in the spectral response above $\approx 0.6\%$, which can be understood as a slip of the graphene on the substrate, since an optical analysis showed that the graphene membrane didn't rupture. Figure 4.12(e) presents yet another load/unload experiment, on yet another hole in the sample. This time a partial slip process took place at $\approx 0.1\%$.

Finally, Figure 4.12(f) shows a $\Delta\omega_G \times \Delta\omega_{2D}$ plot as proposed from [69], where the same data points in Figure 4.12(a, b) have been used. "O($\Delta\omega_G^0, \Delta\omega_{2D}^0$)" represents the initial G and 2D band frequencies before straining. The black dashed line represents the strain vector, while the magenta dashed line represents the doping vector. As is clearly shown, the G and 2D bands followed the expected strain vector as proposed by [69].

It is important to note that in our tests single-layer graphene on top SiN$_x$ suffered from catastrophic failure, rupturing without warning upon tip-induced strain, meanwhile bi/few layer graphene usually slipped instead of rupturing. It was also observed that after the forced rupture of a graphene membrane, the tip gets contaminated, which is seen as the Raman spectral signature of amorphous carbon, therefore the tip must be replaced by a new one whenever this happens.

5

Summary

In this thesis we present a tip-enhanced Raman spectroscopy system capable of breaking the diffraction limit with high reproducibility and capable of performing a diverse number of experimental procedures, from ordinary APD based diffraction unlimited acquisition of a single Raman band, up to more demanding tasks, such as nanomanipulation, hyperspectral imaging and analysis.

We started by exploring the necessary advances in science that enabled us to get to this point, the curiosity that drove scientist to look to the small, the challenges they faced and, more importantly, where we stood on the work of others to progress. A TERS system is built upon other instruments who have entire science fields dedicated to them, when looked upon in isolation, such as optical microscopy and scanning probe microscopy, which are brought together here as a way to break the diffraction limit and, consequently, opening a new field for optical spectroscopy. We provided the details needed in order to understand each of these systems in isolation and how they can be assembled together in order to form an integrated system. Differently from ordinary SPM systems, TERS introduces the concept of an optical nanoantenna, which is the smallest tangible part of the whole system, but arguably the most fundamental. We described the progresses we have made in order to achieve a nanoantenna, or colloquially speaking, a tip, with tunable properties and which presents, consistently, an enhancement factor larger than one order of magnitude when compared to previously existing nanoantennas. Such technology provided the necessary enhancement to perform TERS in two-dimensional systems, where, from a geometrical point of view, the far-field contribution comes from an area $\approx 2 \times 10^8$ times larger than that from which the near-field signal is acquired, being, therefore, notoriously hard to compete.

Provided with such a highly-efficient nanoantenna, we show that breaking the diffraction limit not only allows characterization with higher spatial resolutions, but it also brings its own class of scientific problems, with significant impacts that must be accounted for when using nano-Raman spectroscopy to explore materials science. We showed that the characterization of defects in graphene based structures, which is a solid, well-established research field, has its own regime in the nanoscale, where interference related effects, due to coherence, affects the expected outcome of measurements, where the response from the material is not only dependent on its intrinsic characteristics, but also dependent on the measuring system as a whole. We continued by providing experimental examples of the impacts brought by interference in the characterization of graphene nanoflakes, and showed that a parametrization must be performed in order to apply existing and already validated protocols from the far-field to the near-field.

This work also demonstrates additional capabilities of the TERS system developed, such as its usefulness as a nanomanipulation tool, which, as shown, has been successfully applied to strain measurements in graphene, as well as its possible adaptations to other scanning probe techniques, such as scanning tunneling microscopy, as well as atomic force microscopy.

References

[1] Richard Feynman. *There's plenty of room at the bottom*. URL: http://www.zyvex.com/nanotech/feynman.html (visited on Oct. 23, 2019) (cit. on p. 1).

[2] NY The Trustees of the British Museum / Art Resource. *The Lycurgus Cup*. URL: https://www.britishmuseum.org/research/collection_online/collection_object_details.aspx?objectId=61219&partId=1 (visited on Oct. 8, 2018) (cit. on p. 1).

[3] Unesco. *Nanotechnology is a growing research priority*. URL: http://www.unesco.org/new/en/media-services/single-view/news/nanotechnology_is_a_growing_research_priority/ (visited on Nov. 3, 2019) (cit. on p. 1).

[4] Loredana Protesescu, Sergii Yakunin, Maryna I. Bodnarchuk, Franziska Krieg, Riccarda Caputo, Christopher H. Hendon, Ruo Xi Yang, Aron Walsh, and Maksym V. Kovalenko. "Nanocrystals of Cesium Lead Halide Perovskites (CsPbX 3 , X = Cl, Br, and I): Novel Optoelectronic Materials Showing Bright Emission with Wide Color Gamut". In: *Nano Letters* 15.6 (2015), pp. 3692–3696. ISSN: 1530-6984. DOI: 10.1021/nl5048779. URL: https://pubs.acs.org/doi/10.1021/nl5048779 (cit. on p. 1).

[5] DJ Barber and Ian C Freestone. "An investigation of the origin of the colour of the Lycurgus Cup by analytical transmission electron microscopy". In: *Archaeometry* 32.1 (1990), pp. 33–45 (cit. on p. 1).

[6] Davood Gharailou. *A review of market studies in different fields of nanotechnology*. URL: https://statnano.com/publications/4866 (visited on Oct. 23, 2019) (cit. on p. 2).

[7] "The 2017 Global Assessment Report – The Laboratory Analytical & Life Science Instrumentation Industry, 2015-2020". In: (2017) (cit. on p. 2).

[8] D.E. Newbury and D.B. Williams. "The electron microscope: the materials characterization tool of the millennium". In: *Acta Materialia* 48.1 (2000), pp. 323–346. ISSN: 13596454. DOI: 10.1016/S1359-6454(99)00302-X. URL: https://linkinghub.elsevier.com/retrieve/pii/S135964549900302X (cit. on p. 2).

[9] B. R. A. Neves, J. M. C. Vilela, and M. S. Andrade. "Microscopia de varredura por sonda mecânica: uma introdução". In: *Cerâmica* 44.290 (1998), pp. 212–219. ISSN: 0366-6913. DOI: 10.1590/S0366-69131998000600002 (cit. on p. 2).

[10] Matthieu Baudelet. *Laser Spectroscopy for Sensing: Fundamentals, Techniques and Applications*. Elsevier, 2014 (cit. on p. 2).

[11] Xiaohu Gao, Warren C. W. Chan, and Shuming Nie. "Quantum-dot nanocrystals for ultrasensitive biological labeling and multicolor optical encoding". In: *Journal of Biomedical Optics* 7.4 (2002), p. 532. ISSN: 10833668. DOI: 10.1117/1.1506706 (cit. on p. 2).

[12] MS Ladeira, VA Andrade, ERM Gomes, CJ Aguiar, ER Moraes, JS Soares, EE Silva, RG Lacerda, LO Ladeira, A Jorio, et al. "Highly efficient siRNA delivery system into human and murine cells using single-wall carbon nanotubes". In: *Nanotechnology* 21.38 (2010), p. 385101 (cit. on p. 2).

[13] Eduardo S. Chaves, Margaretha T.C. De Loos-Vollebregt, Adilson J. Curtius, and Frank Vanhaecke. "Determination of trace elements in biodiesel and vegetable oil by inductively coupled plasma optical emission spectrometry following alcohol dilution". In: *Spectrochimica Acta - Part B Atomic Spectroscopy* 66.9-10 (2011), pp. 733–739. ISSN: 05848547. DOI: 10.1016/j.sab.2011.09.006. URL: http://dx.doi.org/10.1016/j.sab.2011.09.006 (cit. on p. 2).

[14] Marcia Marie Maru, Marcia Maria Lucchese, Cristiano Legnani, Welber Gianini Quirino, Andrea Balbo, Isabele Bulhões Aranha, Lílian Terezinha Costa, Cecília Vilani, Lídia Ágata de Sena, Jailton Carreteiro Damasceno, et al. "Biodiesel compatibility with carbon steel and HDPE parts". In: *Fuel Processing Technology* 90.9 (2009), pp. 1175–1182 (cit. on p. 2).

[15] A Jorio, J Ribeiro-Soares, LG Cançado, NPS Falcao, HF Dos Santos, DL Baptista, EH Martins Ferreira, BS Archanjo, and CA Achete. "Microscopy and spectroscopy analysis of carbon nanostructures in highly fertile Amazonian anthrosoils". In: *Soil and Tillage Research* 122 (2012), pp. 61–66 (cit. on p. 2).

[16] J Ribeiro-Soares, LG Cancado, NPS Falcao, EH Martins Ferreira, CA Achete, and A Jorio. "The use of Raman spectroscopy to characterize the carbon materials found in Amazonian anthrosoils". In: *Journal of Raman Spectroscopy* 44.2 (2013), pp. 283–289 (cit. on p. 2).

[17]   Ado Jorio and Mildred S. Dresselhaus. "Nanometrology Links State-of-the-Art Academic Research and Ultimate Industry Needs for Technological Innovation". In: *MRS Bulletin* 32.12 (2007), pp. 988–993. ISSN: 0883-7694. DOI: 10.1557/mrs2007.201. URL: https://www.cambridge.org/core/product/identifier/S0883769400008654/type/journal{_}article (cit. on p. 2).

[18]   Ado Jorio and Mildred S. Dresselhaus. "Nanometrology Sees Progress in Synthesis, Optics, and Microscopy". In: *MRS Bulletin* 33.10 (2008), pp. 972–972. ISSN: 0883-7694. DOI: 10.1557/mrs2008.208. URL: https://www.cambridge.org/core/product/identifier/S0883769400006205/type/journal{_}article (cit. on p. 2).

[19]   Ado Jorio. "Raman Spectroscopy in Graphene-Based Systems: Prototypes for Nanoscience and Nanometrology". In: *ISRN Nanotechnology* 2012.2 (2012), pp. 1–16. ISSN: 2090-6072. DOI: 10.5402/2012/234216. URL: https://www.hindawi.com/archive/2012/234216/ (cit. on pp. 2, 14, 29).

[20]   BS Archanjo, APM Barboza, BRA Neves, LM Malard, EHM Ferreira, JC Brant, ES Alves, F Plentz, V Carozo, B Fragneaud, et al. "The use of a Ga+ focused ion beam to modify graphene for device applications". In: *Nanotechnology* 23.25 (2012), p. 255305 (cit. on p. 2).

[21]   B.S. Archanjo, I.O. Maciel, E.H. Martins Ferreira, S.B. Peripolli, J.C. Damasceno, C.A. Achete, and A. Jorio. "Ion beam nanopatterning and micro-Raman spectroscopy analysis on HOPG for testing FIB performances". In: *Ultramicroscopy* 111.8 (2011), pp. 1338–1342. ISSN: 03043991. DOI: 10.1016/j.ultramic.2011.04.007. URL: http://dx.doi.org/10.1016/j.ultramic.2011.04.007https://linkinghub.elsevier.com/retrieve/pii/S0304399111001574 (cit. on p. 2).

[22]   Norman Colthup. *Introduction to infrared and Raman spectroscopy*. Elsevier, 2012 (cit. on pp. 2, 9).

[23]   Ernst Abbe. "On the Estimation of Aperture in the Microscope." In: *Journal of the Royal Microscopical Society* 1.3 (1881), pp. 388–423 (cit. on p. 2).

[24]   ISO. *ISO/TS 80004-2: 2015 Nanotechnologies–Vocabulary–Part 2: Nano-objects*. 2015 (cit. on p. 3).

[25]   EdwardH Synge. "XXXVIII. A suggested method for extending microscopic resolution into the ultra-microscopic region". In: *The London, Edinburgh and Dublin Philosophical Mag. and Journal of Science* 6.35 (1928), pp. 356–362 (cit. on pp. 3, 8, 27).

[26]   AMAA Lewis, Michael Isaacson, Alec Harootunian, and A Muray. "Development of a 500 Å spatial resolution light microscope: I. light is efficiently transmitted through λ/16 diameter apertures". In: *Ultramicroscopy* 13.3 (1984), pp. 227–231 (cit. on pp. 3, 9).

[27]   Raoul M. Stöckle, Yung Doug Suh, Volker Deckert, and Renato Zenobi. "Nanoscale chemical analysis by tip-enhanced Raman spectroscopy". In: *Chemical Physics Letters* 318.1-3 (2000), pp. 131–136. ISSN: 00092614. DOI: 10.1016/S0009-2614(99)01451-7 (cit. on pp. 3, 9, 27).

[28]   Lukas Novotny. "The history of near-field optics". In: *Progress in optics* 50 (2007), p. 137 (cit. on pp. 3, 8).

[29]   Tanja Deckert-Gaudig, Atsushi Taguchi, Satoshi Kawata, and Volker Deckert. "Tip-enhanced Raman spectroscopy-from early developments to recent advances". In: *Chemical Society Reviews* 46.13 (2017), pp. 4077–4110. ISSN: 14604744. DOI: 10.1039/c7cs00209b. URL: http://dx.doi.org/10.1039/C7CS00209B (cit. on p. 3).

[30]   Achim Hartschuh, Erik J. Sánchez, X. Sunney Xie, and Lukas Novotny. "High-Resolution Near-Field Raman Microscopy of Single-Walled Carbon Nanotubes". In: *Physical Review Letters* 90.9 (2003), p. 4. ISSN: 10797114. DOI: 10.1103/PhysRevLett.90.095503 (cit. on pp. 3, 47).

[31]   Ado Jorio, Luiz Gustavo Cançado, Sebastian Heeg, Lukas Novotny, and Achim Hartschuh. "Tip-Enhanced Spectroscopy and Imaging of Carbon Nanomaterials". In: *Handbook of Carbon Nanomaterials*. World Scientific, 2019, pp. 175–221. DOI: 10.1142/9789813235465_0005. URL: https://doi.org/10.1142%2F9789813235465_0005 (cit. on p. 3).

[32]   Ryota Matsui, Prabhat Verma, Taro Ichimura, Yasushi Inouye, and Satoshi Kawata. "Nanoanalysis of crystalline properties of GaN thin film using tip-enhanced Raman spectroscopy". In: *Applied physics letters* 90.6 (2007), p. 061906 (cit. on p. 3).

[33]   Katrin F. Domke, Dai Zhang, and Bruno Pettinger. "Tip-enhanced raman spectra of picomole quantities of DNA nucleobases at Au(111)". In: *Journal of the American Chemical Society* 129.21 (2007), pp. 6708–6709. ISSN: 00027863. DOI: 10.1021/ja071107q (cit. on p. 3).

[34]   Thomas Schmid, Johannes Burkhard, Boon-Siang Yeo, Weihua Zhang, and Renato Zenobi. "Towards chemical analysis of nanostructures in biofilms I: imaging of biological nanostructures". In: *Analytical and bioanalytical chemistry* 391.5 (2008), pp. 1899–1905 (cit. on p. 3).

[35]   Luiz Gustavo Cançado, Ryan Beams, Ado Jorio, and Lukas Novotny. "Theory of Spatial Coherence in Near-Field Raman Scattering". In: *Physical Review X* 4.3 (2014), p. 031054. ISSN: 2160-3308. DOI: 10.1103/PhysRevX.4.031054. URL: https://link.aps.org/doi/10.1103/PhysRevX.4.031054 (cit. on pp. 3, 27, 38, 87–89, 92).

[36] Ryan Beams, Luiz Gustavo Cançado, Sang-Hyun Oh, Ado Jorio, and Lukas Novotny. "Spatial coherence in near-field Raman scattering". In: *Physical review letters* 113.18 (2014), p. 186101 (cit. on pp. 3, 36, 38, 87, 89, 92).

[37] Paulo Antonio Trindade Araujo. *Study of the Electrostatic Shielding and Enviromental Interactions in Carbon Nanotubes by Ressonance Raman Spectroscopy*. Departamento de Física, Universidade Federal de Minas Gerais, Brazil, 2010 (cit. on pp. 4, 41, 42, 53, 54, 117, 118).

[38] Thiago de Lourenço e Vasconcelos. *Desenvolvimento e estudo de sondas para microscopia óptica de campo próximo*. Departamento de Física, Universidade Federal de Minas Gerais, Brazil, 2015 (cit. on pp. 4, 70).

[39] Thiago L Vasconcelos, Bráulio S Archanjo, Benjamin Fragneaud, Bruno S Oliveira, Juha Riikonen, Changfeng Li, Douglas S Ribeiro, **Rabelo, Cassiano**, Wagner N Rodrigues, Ado Jorio, et al. "Tuning Localized Surface Plasmon Resonance in Scanning Near-Field Optical Microscopy Probes". In: *ACS nano* 9.6 (2015), pp. 6297–6304 (cit. on pp. 4, 70, 139).

[40] Thiago L. Vasconcelos, Bráulio S. Archanjo, Bruno S. Oliveira, Rogério Valaski, Rafael C. Cordeiro, Helton G. Medeiros, **Rabelo, Cassiano**, Aroldo Ribeiro, Peter Ercius, Carlos A. Achete, Ado Jorio, and Luiz Gustavo Cançado. "Plasmon-Tunable Tip Pyramids: Monopole Nanoantennas for Near-Field Scanning Optical Microscopy". In: *Advanced Optical Materials* 6.20 (2018), p. 1800528. ISSN: 21951071. DOI: 10.1002/adom.201800528. URL: http://doi.wiley.com/10.1002/adom.201800528 (cit. on pp. 4, 70, 71).

[41] T. L. e Vasconcelos, A. Jorio, B. S. Archanjo, L. G. O. L. Cancado, C. A. Achete, W. N. Rodrigues, B. Fragneaud, D. S. Ribeiro, B. S. Oliveira, and **Rabelo, Cassiano**. "Metallic device for scanning near-field optical microscopy and spectroscopy and method for manufacturing same". Pat. US Patent US10274514B2 - Priority to BR1020150103522. 2018 (cit. on pp. 4, 70).

[42] Vasconcelos Thiago E. De Lourenço, Oliveira Bruno Santos De, Carlos Alberto Achete, Braulio Soares Archanjo, Vasconcelos Ado Jorio De, Lopes Cancado Luiz Gustavo De Oliveira, Wagner Nunes Rodrigues, Silva Wetzstein Caroline Arantes Da, Rogerio Valaski, and **Rabelo, Cassiano**. "Metallic device for scanning probe microscopy and method for manufacturing same". Pat. US Patent US2018/0372777 - Priority to BR10201503120. 2018 (cit. on pp. 4, 70).

[43] Randy O. Wayne. *Light and Video Microscopy*. Academic Press, 2014. ISBN: 0124114849. URL: https://www.xarg.org/ref/a/0124114849/ (cit. on p. 5).

[44] S. Bradbury. *The Evolution of the Microscope*. Pergamon, 2014 (cit. on pp. 5, 6).

[45] G. L'E. Turner. "The History of Optical Instruments: A Brief Survey of Sources and Modern Studies". In: *History of Science* 8.1 (1969), pp. 53–93 (cit. on p. 5).

[46] William J Croft. *Under the Microscope:A Brief History of Microscopy (Series in Popular Science Book 5)*. WSPC, 2006. ISBN: 9814338044 (cit. on p. 5).

[47] Lukas Novotny and Stephan J. Stranick. "Near-Field Optical Microscopy and Spectroscopy With Pointed Probes". In: *Annual Review of Physical Chemistry* 57.1 (2006), pp. 303–331. ISSN: 0066-426X. DOI: 10.1146/annurev.physchem.56.092503.141236 (cit. on pp. 6, 26).

[48] E Abbe. "Contributions to the theory of the microscope and microscopic detection (translated from German)". In: *Arch Mikroskop Anat* 9 (1873), pp. 413–468 (cit. on p. 6).

[49] Rayleigh. "XXXI. Investigations in optics, with special reference to the spectroscope". In: *The London, Edinburgh, and Dublin Philosophical Magazine and Journal of Science* 8.49 (1879), pp. 261–274. ISSN: 1941-5982. DOI: 10.1080/14786447908639684. URL: https://www.tandfonline.com/doi/full/10.1080/14786447908639684 (cit. on p. 6).

[50] Lukas Novotny and Bert Hecht. *Principles of nano-optics*. Cambridge university press, 2012 (cit. on pp. 7–9, 25, 47, 52).

[51] Masahiko Daimon and Akira Masumura. "Measurement of the refractive index of distilled water from the near-infrared region to the ultraviolet region". In: *Applied optics* 46.18 (2007), pp. 3811–3820 (cit. on p. 7).

[52] Marvin Minsky. "Microscopy apparatus". Pat. US Patent App. US3013467A. 1957 (cit. on p. 7).

[53] G. Binnig, H. Rohrer, Ch. Gerber, and E. Weibel. "Surface Studies by Scanning Tunneling Microscopy". In: *Physical Review Letters* 49.1 (1982), pp. 57–61. ISSN: 0031-9007. DOI: 10.1103/PhysRevLett.49.57 (cit. on pp. 8, 20).

[54] Christian Girard, Christian Joachim, and Sébastien Gauthier. *The physics of the near-field*. 2000. DOI: 10.1088/0034-4885/63/6/202. URL: http://stacks.iop.org/0034-4885/63/i=6/a=202?key=crossref.16c67ce96f399ecfd838d017e4a311f0 (cit. on p. 9).

[55] Prabhat Verma. *Tip-Enhanced Raman Spectroscopy: Technique and Recent Advances*. 2017. DOI: 10.1021/acs.chemrev.6b00821 (cit. on pp. 9, 36).

[56]   Markus B. Raschke and Christoph Lienau. "Apertureless near-field optical microscopy: Tip-sample coupling in elastic light scattering". In: *Applied Physics Letters* 83.24 (2003), pp. 5089–5091. ISSN: 00036951. DOI: 10.1063/1.1632023 (cit. on p. 9).

[57]   Catalin C. Neacsu, Jens Dreyer, Nicolas Behr, and Markus B. Raschke. "Scanning-probe Raman spectroscopy with single-molecule sensitivity". In: *Physical Review B - Condensed Matter and Materials Physics* 73.19 (2006), pp. 1–4. ISSN: 10980121. DOI: 10.1103/PhysRevB.73.193406 (cit. on p. 9).

[58]   Bruno Pettinger, Katrin F. Domke, Dai Zhang, Rolf Schuster, and Gerhard Ertl. "Direct monitoring of plasmon resonances in a tip-surface gap of varying width". In: *Physical Review B - Condensed Matter and Materials Physics* 76.11 (2007), pp. 1–4. ISSN: 10980121. DOI: 10.1103/PhysRevB.76.113409 (cit. on p. 9).

[59]   D. W. Pohl, W. Denk, and M. Lanz. "Optical stethoscopy: Image recording with resolution $\lambda/20$". In: *Applied Physics Letters* 44.7 (1984), pp. 651–653. ISSN: 00036951 (cit. on p. 9).

[60]   U. Ch Fischer. "OPTICAL CHARACTERISTICS OF 0. 1 mu m CIRCULAR APERTURES IN A METAL FILM AS LIGHT SOURCES FOR SCANNING ULTRAMICROSCOPY." In: *Journal of Vacuum Science & Technology B: Microelectronics Processing and Phenomena* 386.1985 (1984), pp. 386–390. ISSN: 0734211X. DOI: 10.1116/1.583269 (cit. on p. 9).

[61]   E. Betzig, M. Isaacson, and A. Lewis. "Collection mode near-field scanning optical microscopy". In: *Applied Physics Letters* 51.25 (1987), pp. 2088–2090. ISSN: 00036951. DOI: 10.1063/1.98956 (cit. on p. 9).

[62]   Eric Betzig and Robert J. Chichester. "Single molecules observed by near-field scanning optical microscopy". In: *Science* 262.5138 (1993), pp. 1422–1425. ISSN: 00368075. DOI: 10.1126/science.262.5138.1422 (cit. on p. 9).

[63]   M. H.P. Moers, W. H.J. Kalle, A. G.T. Ruiter, J. C.A.G. Wiegant, A. K. Raap, J. Greve, B. G. De Grooth, and N. F. Van Hulst. "Fluorescence in situ hybridization on human metaphase chromosomes detected by near-field scanning optical microscopy". In: *Journal of Microscopy* 182.1 (1996), pp. 40–45. ISSN: 00222720. DOI: 10.1111/j.1365-2818.1996.tb04795.x (cit. on p. 9).

[64]   Mark S. Anderson. "Locally enhanced Raman spectroscopy with an atomic force microscope". In: *Applied Physics Letters* 76.21 (2000), pp. 3130–3132. ISSN: 00036951. DOI: 10.1063/1.126546 (cit. on pp. 9, 27).

[65]   Norihiko Hayazawa, Yasushi Inouye, Zouheir Sekkat, and Satoshi Kawata. "Metallized tip amplification of near-field Raman scattering". In: *Optics Communications* 183.1 (2000), pp. 333–336. ISSN: 00304018. DOI: 10.1016/S0030-4018(00)00894-4 (cit. on pp. 9, 27).

[66]   C. V. RAMAN and K. S. KRISHNAN. "A New Type of Secondary Radiation". In: *Nature* 121.3048 (1928), pp. 501–502. ISSN: 0028-0836. DOI: 10.1038/121501c0 (cit. on p. 9).

[67]   Chen Si, Zhimei Sun, and Feng Liu. "Strain engineering of graphene: a review". In: *Nanoscale* 8.6 (2016), pp. 3207–3217. ISSN: 2050-7488. DOI: 10.1039/C5NR07755A. URL: http://pubs.rsc.org/en/Content/ArticleLanding/2016/NR/C5NR07755A (cit. on pp. 9, 31).

[68]   Ryan Beams, Luiz Gustavo Cançado, and Lukas Novotny. "Raman characterization of defects and dopants in graphene". In: *Journal of Physics Condensed Matter* 27.8 (2015). ISSN: 1361648X. DOI: 10.1088/0953-8984/27/8/083002 (cit. on p. 9).

[69]   Ji Eun Lee, Gwanghyun Ahn, Jihye Shim, Young Sik Lee, and Sunmin Ryu. "Optical separation of mechanical strain from charge doping in graphene". In: *Nature Communications* 3.May (2012), p. 1024. ISSN: 2041-1723. DOI: 10.1038/ncomms2022. URL: http://dx.doi.org/10.1038/ncomms2022 (cit. on pp. 9, 31, 33, 34, 79, 85, 86, 97–99).

[70]   Wenjing Jie, Yeung Yu Hui, Yang Zhang, Shu Ping Lau, and Jianhua Hao. "Effects of controllable biaxial strain on the Raman spectra of monolayer graphene prepared by chemical vapor deposition". In: *Applied Physics Letters* 102.22 (2013), pp. 1–5. ISSN: 00036951. DOI: 10.1063/1.4809922 (cit. on pp. 9, 31).

[71]   Kyoung Duck Park, Omar Khatib, Vasily Kravtsov, Genevieve Clark, Xiaodong Xu, and Markus B. Raschke. "Hybrid Tip-Enhanced Nanospectroscopy and Nanoimaging of Monolayer WSe2 with Local Strain Control". In: *Nano Letters* 16.4 (2016), pp. 2621–2627. ISSN: 15306992. DOI: 10.1021/acs.nanolett.6b00238 (cit. on p. 9).

[72]   Heinz Schmid, Mikael T. Björk, Joachim Knoch, Siegfried Karg, Heike Riel, and Walter Riess. "Doping limits of grown in situ doped silicon nanowires using phosphine". In: *Nano Letters* 9.1 (2009), pp. 173–177. ISSN: 15306984. DOI: 10.1021/nl802739v (cit. on p. 9).

[73]   M. W. Iqbal, Arun Kumar Singh, M. Z. Iqbal, and Jonghwa Eom. "Raman fingerprint of doping due to metal adsorbates on graphene". In: *Journal of Physics Condensed Matter* 24.33 (2012). ISSN: 09538984. DOI: 10.1088/0953-8984/24/33/335301 (cit. on p. 9).

[74] Martin Kalbac, Alfonso Reina-Cecco, Hootan Farhat, Jing Kong, Ladislav Kavan, and Mildred S Dresselhaus. "The Influence of Strong Electron and Hole Doping on the Raman Intensity of Chemical Vapor-Deposition Graphene". In: *ACS Nano* 4.10 (2010), pp. 6055–6063. ISSN: 1936-0851. DOI: 10.1021/nn1010914. URL: https://pubs.acs.org/doi/10.1021/nn1010914 (cit. on pp. 9, 31).

[75] J. L. Bahr, J. Yang, D. V. Kosynkin, M. J. Bronikowski, R. E. Smalley, and J. M. Tour. "Functionalization of carbon nanotubes by electrochemical reduction of aryl diazonium salts: A bucky paper electrode". In: *Journal of the American Chemical Society* 123.27 (2001), pp. 6536–6542. ISSN: 00027863. DOI: 10.1021/ja010462s (cit. on p. 9).

[76] Zhuang Liu, Corrine Davis, Weibo Cai, Lina He, Xiaoyuan Chen, and Hongjie Dai. "Circulation and long-term fate of functionalized, biocompatible single-walled carbon nanotubes in mice probed by Raman spectroscopy". In: *Proceedings of the National Academy of Sciences of the United States of America* 105.5 (2008), pp. 1410–1415. ISSN: 00278424. DOI: 10.1073/pnas.0707654105 (cit. on p. 9).

[77] Ming Fang, Kaigang Wang, Hongbin Lu, Yuliang Yang, and Steven Nutt. "Covalent polymer functionalization of graphene nanosheets and mechanical properties of composites". In: *Journal of Materials Chemistry* 19.38 (2009), pp. 7098–7105. ISSN: 09599428. DOI: 10.1039/b908220d (cit. on p. 9).

[78] Indhira O. MacIel, Neil Anderson, Marcos A. Pimenta, Achim Hartschuh, Huihong Qian, Mauricio Terrones, Humberto Terrones, Jessica Campos-Delgado, Apparao M. Rao, Lukas Novotny, and Ado Jorio. "Electron and phonon renormalization near charged defects in carbon nanotubes". In: *Nature Materials* 7.11 (2008), pp. 878–883. ISSN: 14764660. DOI: 10.1038/nmat2296 (cit. on pp. 9, 25).

[79] Florian Banhart, Jani Kotakoski, and Arkady V. Krasheninnikov. "Structural defects in graphene". In: *ACS Nano* 5.1 (2011), pp. 26–41. ISSN: 19360851. DOI: 10.1021/nn102598m (cit. on p. 9).

[80] L. G. Cançado, A. Jorio, E. H.Martins Ferreira, F. Stavale, C. A. Achete, R. B. Capaz, M. V.O. Moutinho, A. Lombardo, T. S. Kulmala, and A. C. Ferrari. "Quantifying defects in graphene via Raman spectroscopy at different excitation energies". In: *Nano Letters* 11.8 (2011), pp. 3190–3196. ISSN: 15306984. DOI: 10.1021/nl201432g. URL: http://pubs.acs.org/doi/abs/10.1021/nl201432g (cit. on p. 9).

[81] Luiz Gustavo Cançado, Mateus Gomes da Silva, Erlon H Martins Ferreira, Ferdinand Hof, Katerina Kampioti, Kai Huang, Alain Pénicaud, Carlos Alberto Achete, Rodrigo B Capaz, and Ado Jorio. "Disentangling contributions of point and line defects in the Raman spectra of graphene-related materials". In: *2D Materials* 4.2 (2017), p. 025039. ISSN: 2053-1583. DOI: 10.1088/2053-1583/aa5e77. URL: http://stacks.iop.org/2053-1583/4/i=2/a=025039?key=crossref.376f8e0c03840738868cf8e19cbc341a (cit. on pp. 9, 14, 31, 34, 35, 79, 83, 91, 92).

[82] M.M. Lucchese, F. Stavale, E.H. Martins Ferreira, C. Vilani, M.V.O. Moutinho, Rodrigo B. Capaz, C.A. Achete, and A. Jorio. "Quantifying ion-induced defects and Raman relaxation length in graphene". In: *Carbon* 48.5 (2010), pp. 1592–1597. ISSN: 00086223. DOI: 10.1016/j.carbon.2009.12.057. URL: https://linkinghub.elsevier.com/retrieve/pii/S0008622310000138 (cit. on pp. 9, 13, 31).

[83] Chanwoo Lee, Byeong Geun Jeong, Seok Joon Yun, Young Hee Lee, Seung Mi Lee, and Mun Seok Jeong. "Unveiling Defect-Related Raman Mode of Monolayer WS2 via Tip-Enhanced Resonance Raman Scattering". In: *ACS Nano* 12.10 (2018), pp. 9982–9990. ISSN: 1936086X. DOI: 10.1021/acsnano.8b04265 (cit. on p. 9).

[84] Aleksander Jablonski. "Efficiency of anti-Stokes fluorescence in dyes". In: *Nature* 131.3319 (1933), p. 839 (cit. on p. 10).

[85] Richard L. McCreery. *Raman Spectroscopy for Chemical Analysis*. Wiley-Interscience, 2000. ISBN: 0471252875 (cit. on p. 10).

[86] Derek A Long. *The Raman Effect: A Unified Treatment of the Theory of Raman Scattering by Molecules*. John Wiley & Sons, Ltd, 2002 (cit. on p. 10).

[87] Ian R. Lewis. *Handbook of Raman Spectroscopy: From the Research Laboratory to the Process Line (Practical Spectroscopy)*. CRC Press, 2001. ISBN: 0824705572 (cit. on p. 10).

[88] *Introductory Raman Spectroscopy*. Elsevier, 2003. ISBN: 9780122541056. DOI: 10.1016/B978-0-12-254105-6.X5000-8. URL: https://linkinghub.elsevier.com/retrieve/pii/B9780122541056X50008 (cit. on p. 11).

[89] Bert J. Kip and Robert J. Meier. "Determination of the Local Temperature at a Sample during Raman Experiments Using Stokes and Anti-Stokes Raman Bands". In: *Appl. Spectrosc.* 44.4 (1990), pp. 707–711. URL: http://as.osa.org/abstract.cfm?URI=as-44-4-707 (cit. on p. 12).

[90] J. Ribeiro-Soares, M. E. Oliveros, C. Garin, M. V. David, L. G.P. Martins, C. A. Almeida, E. H. Martins-Ferreira, K. Takai, T. Enoki, R. Magalhães-Paniago, A. Malachias, A. Jorio, B. S. Archanjo, C. A. Achete, and L. G. Cançado. "Structural analysis of polycrystalline graphene systems by Raman spectroscopy". In: *Carbon* 95 (2015), pp. 646–652. ISSN: 00086223. DOI: 10.1016/j.carbon.2015.08.020. arXiv: 1511.06659 (cit. on p. 13).

[91]   Andrea C Ferrari, JC Meyer, V Scardaci, C Casiraghi, Michele Lazzeri, Francesco Mauri, S Piscanec, Da Jiang, KS Novoselov, S Roth, et al. "Raman spectrum of graphene and graphene layers". In: *Physical review letters* 97.18 (2006), p. 187401 (cit. on pp. 13, 31, 33, 78).

[92]   Ado Jorio, Riichiro Saito, Gene Dresselhaus, and Mildred S. Dresselhaus. *Raman Spectroscopy in Graphene Related Systems*. Weinheim, Germany: Wiley-VCH Verlag GmbH & Co. KGaA, 2011. ISBN: 9783527632695. DOI: 10.1002/9783527632695. URL: http://doi.wiley.com/10.1002/9783527632695 (cit. on pp. 14, 30–33, 78).

[93]   Ado Jorio, Gene Dresselhaus, and Mildred S Dresselhaus. *Carbon nanotubes: advanced topics in the synthesis, structure, properties and applications*. Vol. 111. Springer Science & Business Media, 2007 (cit. on p. 14).

[94]   FeuRenard. *Diagram of a Czerny–Turner monochromator*. URL: https://en.wikipedia.org/wiki/Monochromator#/media/File:Czerny-Turner_Monochromator.svg (visited on July 5, 2019) (cit. on p. 16).

[95]   Erwin G. Loewen and Evgeny Popov. *Diffraction Gratings and Applications (Optical Science and Engineering)*. CRC Press, 1997. ISBN: 0824799232 (cit. on p. 16).

[96]   Yuriy K Sirenko and S Strom. *Modern Theory of Gratings: Resonant Scattering: Analysis Techniques and Phenomena (Springer Series in Optical Sciences Book 153)*. Springer, 2010. ISBN: 978-1-4419-1199-5 (cit. on p. 16).

[97]   Mark Kasperczyk, Filomeno S de Aguiar Júnior, **Rabelo, Cassiano**, Andre Saraiva, Marcelo F Santos, Lukas Novotny, and Ado Jorio. "Temporal quantum correlations in inelastic light scattering from water". In: *Physical review letters* 117.24 (2016), p. 243603 (cit. on p. 17).

[98]   Bert Voigtländer. *Scanning Probe Microscopy*. NanoScience and Technology. Berlin, Heidelberg: Springer Berlin Heidelberg, 2015. ISBN: 978-3-662-45239-4. DOI: 10.1007/978-3-662-45240-0. URL: http://link.springer.com/10.1007/978-3-662-45240-0 (cit. on pp. 18, 22, 23).

[99]   Ernst Meyer. *Scanning Probe Microscopy: The Lab on a Tip (Advanced Texts in Physics)*. Springer, 2011. ISBN: 3642077374. URL: https://www.xarg.org/ref/a/3642077374/ (cit. on pp. 18, 20, 21).

[100] Dalia G Yablon. *Scanning probe microscopy for industrial applications: nanomechanical characterization*. John Wiley & Sons, 2013 (cit. on p. 18).

[101] David Nečas, Petr Klapetek, Volker Neu, Marek Havlíček, Robert Puttock, Olga Kazakova, Xiukun Hu, and Lenka Zajíčková. "Determination of tip transfer function for quantitative MFM using frequency domain filtering and least squares method". In: *Scientific Reports* 9.1 (2019), pp. 1–15. ISSN: 20452322. DOI: 10.1038/s41598-019-40477-x (cit. on p. 18).

[102] Nizhniy Novgorod. "Fundamentals of scanning probe microscopy". In: *The Russian Academy of Sciences* (2004), p. 97 (cit. on pp. 19, 20).

[103] Oleg V Yazyev and Steven G Louie. "Topological defects in graphene: Dislocations and grain boundaries". In: *Physical Review B* 81.19 (2010), p. 195420 (cit. on p. 21).

[104] TR Albrecht, HA Mizes, J Nogami, Sang-il Park, and CF Quate. "Observation of tilt boundaries in graphite by scanning tunneling microscopy and associated multiple tip effects". In: *Applied physics letters* 52.5 (1988), pp. 362–364 (cit. on p. 21).

[105] Gerd Binnig, Calvin F Quate, and Ch Gerber. "Atomic force microscope". In: *Physical Review Letters* 56.9 (1986), p. 930 (cit. on p. 22).

[106] AIST-NT. *AFM Cantilevers - model fpN01HR*. URL: http://nanoprobes.aist-nt.com/index.php?main_page=product_info&products_id=231 (visited on July 9, 2019) (cit. on p. 23).

[107] Nanonis GmbH. "Piezoelectric Quartz Tuning Forks for Scanning Probe Microscopy". In: 2005 (cit. on p. 24).

[108] Palash Bharadwaj, Bradley Deutsch, and Lukas Novotny. "Optical Antennas". In: *Adv. Opt. Photon.* 1.3 (2009), pp. 438–483. DOI: 10.1364/AOP.1.000438 (cit. on p. 25).

[109] Joonhee Lee, Kevin T Crampton, Nicholas Tallarida, and V Ara Apkarian. "Visualizing vibrational normal modes of a single molecule with atomically confined light". In: *Nature* 568.7750 (2019), p. 78 (cit. on p. 26).

[110] Sayantan Mahapatra, Yingying Ning, Jeremy F. Schultz, Linfei Li, Jun Long Zhang, and Nan Jiang. "Angstrom Scale Chemical Analysis of Metal Supported Trans- and Cis-Regioisomers by Ultrahigh Vacuum Tip-Enhanced Raman Mapping". In: *Nano Letters* 19.5 (2019), pp. 3267–3272. ISSN: 15306992. DOI: 10.1021/acs.nanolett.9b00826 (cit. on p. 26).

[111] M. Fleischmann, P. J. Hendra, and A. J. McQuillan. "Raman spectra of pyridine adsorbed at a silver electrode". In: *Chemical Physics Letters* 26.2 (1974), pp. 163–166. ISSN: 00092614. DOI: 10.1016/0009-2614(74)85388-1 (cit. on p. 26).

[112] M. Grant Albrecht and J. Alan Creighton. "Anomalously Intense Raman Spectra of Pyridine at a Silver Electrode". In: *Journal of the American Chemical Society* 99.15 (1977), pp. 5215–5217. ISSN: 15205126. DOI: 10.1021/ja00457a071 (cit. on p. 26).

[113] Evan J. Blackie, Eric C. Le Ru, and Pablo G. Etchegoin. "Single-Molecule Surface-Enhanced Raman Spectroscopy of Nonresonant Molecules". In: *Journal of the American Chemical Society* 131.40 (2009), pp. 14466–14472. ISSN: 0002-7863. DOI: 10.1021/ja905319w. URL: https://pubs.acs.org/doi/10.1021/ja905319w (cit. on p. 26).

[114] Dong-Kwon Lim, Ki-Seok Jeon, Hyung Min Kim, Jwa-Min Nam, and Yung Doug Suh. "Nanogap-engineerable Raman-active nanodumbbells for single-molecule detection". In: *Nature Materials* 9.1 (2010), pp. 60–67. ISSN: 1476-1122. DOI: 10.1038/nmat2596. URL: http://www.nature.com/articles/nmat2596 (cit. on p. 26).

[115] Satoshi Kawata, Yasushi Inouye, and Prabhat Verma. "Plasmonics for near-field nano-imaging and superlensing". In: *Nature Photonics* 3.7 (2009), pp. 388–394. ISSN: 17494885. DOI: 10.1038/nphoton.2009.111. URL: http://dx.doi.org/10.1038/nphoton.2009.111 (cit. on p. 26).

[116] John Wessel. "Surface-enhanced optical microscopy". In: *Journal of the Optical Society of America B* 2.9 (1985), p. 1538. ISSN: 0740-3224. DOI: 10.1364/josab.2.001538 (cit. on p. 27).

[117] Bruno Pettinger, Gennaro Picardi, Rolf Schuster, and Gerhard Ertl. "Surface Enhanced Raman Spectroscopy: Towards Single Molecule Spectroscopy". In: *Electrochemistry* 68.12 (2000), pp. 942–949. ISSN: 1344-3542. DOI: 10.5796/electrochemistry.68.942 (cit. on p. 27).

[118] LG Cançado, Ado Jorio, A Ismach, E Joselevich, Achim Hartschuh, and Lukas Novotny. "Mechanism of near-field Raman enhancement in one-dimensional systems". In: *Physical Review Letters* 103.18 (2009), p. 186101 (cit. on p. 27).

[119] Rodolfo V. Maximiano, Ryan Beams, Lukas Novotny, Ado Jorio, and Luiz Gustavo Cançado. "Mechanism of near-field Raman enhancement in two-dimensional systems". In: *Physical Review B* 85.23 (2012), p. 235434. ISSN: 1098-0121. DOI: 10.1103/PhysRevB.85.235434. URL: https://link.aps.org/doi/10.1103/PhysRevB.85.235434 (cit. on pp. 27, 37).

[120] Thomas Schmid, Boon Siang Yeo, Grace Leong, Johannes Stadler, and Renato Zenobi. "Performing tip-enhanced Raman spectroscopy in liquids". In: *Journal of Raman Spectroscopy* 40.10 (2009), pp. 1392–1399. ISSN: 03770486. DOI: 10.1002/jrs.2387 (cit. on p. 27).

[121] V Deckert and John Wiley. "Tip-Enhanced Raman Spectroscopy". In: July (2009), pp. 1336–1337. DOI: 10.1002/jrs.2452 (cit. on p. 27).

[122] Katrin F. Domke and Bruno Pettinger. "Studying surface chemistry beyond the diffraction limit: 10 years of TERS". In: *ChemPhysChem* 11.7 (2010), pp. 1365–1373. ISSN: 14394235. DOI: 10.1002/cphc.200900975 (cit. on p. 27).

[123] Thomas Schmid, Lothar Opilik, Carolin Blum, and Renato Zenobi. "Nanoscale chemical imaging using tip-enhanced raman spectroscopy: A critical review". In: *Angewandte Chemie - International Edition* 52.23 (2013), pp. 5940–5954. ISSN: 14337851. DOI: 10.1002/anie.201203849 (cit. on p. 27).

[124] Matthew D. Sonntag, Eric A. Pozzi, Nan Jiang, Mark C. Hersam, and Richard P. Van Duyne. "Recent advances in tip-enhanced raman spectroscopy". In: *Journal of Physical Chemistry Letters* 5.18 (2014), pp. 3125–3130. ISSN: 19487185. DOI: 10.1021/jz5015746 (cit. on p. 27).

[125] Lucas Langelüddecke, Prabha Singh, and Volker Deckert. "Exploring the Nanoscale: Fifteen Years of Tip-Enhanced Raman Spectroscopy". In: *Applied Spectroscopy* 69.12 (2015), pp. 1357–1371. ISSN: 0003-7028. DOI: 10.1366/15-08014 (cit. on p. 27).

[126] S. S. Kharintsev, G. G. Hoffmann, P. S. Dorozhkin, G. De With, and J. Loos. "Atomic force and shear force based tip-enhanced Raman spectroscopy and imaging". In: *Nanotechnology* 18.31 (2007). ISSN: 09574484. DOI: 10.1088/0957-4484/18/31/315502 (cit. on p. 27).

[127] Neil Anderson, Achim Hartschuh, Steve Cronin, and Lukas Novotny. "Nanoscale vibrational analysis of single-walled carbon nanotubes". In: *Journal of the American Chemical Society* 127.8 (2005), pp. 2533–2537. ISSN: 00027863. DOI: 10.1021/ja045190i (cit. on p. 27).

[128] L. E. Hennemann, A. J. Meixner, and D. Zhang. "Surface- and tip-enhanced Raman spectroscopy of DNA". In: *Spectroscopy* 24.1-2 (2010), pp. 119–124. ISSN: 07124813. DOI: 10.3233/SPE-2010-0416 (cit. on p. 27).

[129] D. Zhang, X. Wang, Kai Braun, Hans Joachim Egelhaaf, Monika Fleischer, Laura Hennemann, Holger Hintz, Catrinel Stanciu, Christoph J. Brabec, Dieter P. Kern, and Alfred J. Meixner. "Parabolic mirror-assisted tip-enhanced spectroscopic imaging for non-transparent materials". In: *Journal of Raman Spectroscopy* 40.10 (2009), pp. 1371–1376. ISSN: 03770486. DOI: 10.1002/jrs.2411 (cit. on p. 27).

[130] Jordan M. Klingsporn, Nan Jiang, Eric A. Pozzi, Matthew D. Sonntag, Dhabih Chulhai, Tamar Seideman, Lasse Jensen, Mark C. Hersam, and Richard P. Van Duyne. "Intramolecular insight into adsorbate-substrate interactions via low-temperature, ultrahigh-vacuum tip-enhanced Raman spectroscopy". In: *Journal of the American Chemical Society* 136.10 (2014), pp. 3881–3887. ISSN: 15205126. DOI: 10.1021/ja411899k (cit. on p. 27).

[131]   Weihua Zhang, Boon Siang Yeo, Thomas Schmid, and Renato Zenobi. "Single molecule tip-enhanced Raman spectroscopy with silver tips". In: *Journal of Physical Chemistry C* 111.4 (2007), pp. 1733–1738. ISSN: 19327447. DOI: 10.1021/jp064740r (cit. on p. 27).

[132]   Bruno Pettinger, Katrin F. Domke, Dai Zhang, Gennaro Picardi, and Rolf Schuster. "Tip-enhanced Raman scattering: Influence of the tip-surface geometry on optical resonance and enhancement". In: *Surface Science* 603.10-12 (2009), pp. 1335–1341. ISSN: 00396028. DOI: 10.1016/j.susc.2008.08.033. URL: http://dx.doi.org/10.1016/j.susc.2008.08.033 (cit. on p. 27).

[133]   Jens Steidtner and Bruno Pettinger. "High-resolution microscope for tip-enhanced optical processes in ultrahigh vacuum". In: *Review of Scientific Instruments* 78.10 (2007). ISSN: 00346748. DOI: 10.1063/1.2794227 (cit. on p. 27).

[134]   J. C. Charlier, P. C. Eklund, J. Zhu, and A. C. Ferrari. "Electron and phonon properties of graphene: Their relationship with carbon nanotubes". In: *Topics in Applied Physics* 111.2008 (2008), pp. 673–709. ISSN: 03034216. DOI: 10.1007/978-3-540-72865-8_21 (cit. on p. 29).

[135]   Nobelprize.org. Nobel Media. *Nobel Prize in Physics 2010 - Graphene – the perfect atomic lattice*. 2010. URL: https://www.nobelprize.org/prizes/physics/2010/illustrated-information/ (visited on Oct. 16, 2019) (cit. on pp. 29, 30).

[136]   M.S. Dresselhaus, G. Dresselhaus, A. Jorio, A.G. Souza Filho, and R. Saito. "Raman spectroscopy on isolated single wall carbon nanotubes". In: *Carbon* 40.12 (2002), pp. 2043–2061. ISSN: 00086223. DOI: 10.1016/S0008-6223(02)00066-0. URL: https://linkinghub.elsevier.com/retrieve/pii/S0008622302000660 (cit. on p. 29).

[137]   M.S. Dresselhaus, G. Dresselhaus, R. Saito, and A. Jorio. "Raman spectroscopy of carbon nanotubes". In: *Physics Reports* 409.2 (2005), pp. 47–99. ISSN: 03701573. DOI: 10.1016/j.physrep.2004.10.006. URL: https://linkinghub.elsevier.com/retrieve/pii/S0370157304004570 (cit. on p. 29).

[138]   Mildred S. Dresselhaus, Ado Jorio, Mario Hofmann, Gene Dresselhaus, and Riichiro Saito. "Perspectives on carbon nanotubes and graphene Raman spectroscopy". In: *Nano Letters* 10.3 (2010), pp. 751–758. ISSN: 15306984. DOI: 10.1021/nl904286r (cit. on pp. 29, 31).

[139]   M S Dresselhaus. *Science of Fullerenes and Carbon Nanotubes: Their Properties and Applications*. Academic Press, 1996. ISBN: 0122218205. URL: https://www.xarg.org/ref/a/0122218205/ (cit. on p. 29).

[140]   L. M. Malard, M. A. Pimenta, G. Dresselhaus, and M. S. Dresselhaus. "Raman spectroscopy in graphene". In: *Physics Reports* 473.5-6 (2009), pp. 51–87. ISSN: 03701573. DOI: 10.1016/j.physrep.2009.02.003. URL: http://dx.doi.org/10.1016/j.physrep.2009.02.003 (cit. on pp. 29, 31).

[141]   Kostya S Novoselov, Andre K Geim, Sergei V Morozov, D Jiang, Y_ Zhang, Sergey V Dubonos, Irina V Grigorieva, and Alexandr A Firsov. "Electric field effect in atomically thin carbon films". In: *science* 306.5696 (2004), pp. 666–669 (cit. on p. 30).

[142]   ZH Ni, HM Wang, J Kasim, HM Fan, T Yu, YH Wu, YP Feng, and ZX Shen. "Graphene thickness determination using reflection and contrast spectroscopy". In: *Nano letters* 7.9 (2007), pp. 2758–2763 (cit. on p. 30).

[143]   Rahul Raveendran Nair, Peter Blake, Alexander N Grigorenko, Konstantin S Novoselov, Tim J Booth, Tobias Stauber, Nuno MR Peres, and Andre K Geim. "Fine structure constant defines visual transparency of graphene". In: *Science* 320.5881 (2008), pp. 1308–1308 (cit. on p. 30).

[144]   Kirill I Bolotin, KJ Sikes, Zd Jiang, M Klima, G Fudenberg, J Hone, Ph Kim, and HL Stormer. "Ultrahigh electron mobility in suspended graphene". In: *Solid State Communications* 146.9 (2008), pp. 351–355 (cit. on p. 30).

[145]   Alexander A Balandin, Suchismita Ghosh, Wenzhong Bao, Irene Calizo, Desalegne Teweldebrhan, Feng Miao, and Chun Ning Lau. "Superior thermal conductivity of single-layer graphene". In: *Nano letters* 8.3 (2008), pp. 902–907 (cit. on p. 30).

[146]   Changgu Lee, Xiaoding Wei, Jeffrey W Kysar, and James Hone. "Measurement of the elastic properties and intrinsic strength of monolayer graphene". In: *science* 321.5887 (2008), pp. 385–388 (cit. on p. 30).

[147]   Joel Moser, Amelia Barreiro, and Adrian Bachtold. "Current-induced cleaning of graphene". In: *Applied Physics Letters* 91.16 (2007), p. 163513 (cit. on p. 30).

[148]   K S Novoselov and A H Castro Neto. "Two-dimensional crystals-based heterostructures: materials with tailored properties". In: *Physica Scripta* T146 (2012), p. 014006. DOI: 10.1088/0031-8949/2012/t146/014006. URL: https://doi.org/10.1088%2F0031-8949%2F2012%2Ft146%2F014006 (cit. on p. 31).

[149]   Alfonso Reina, Xiaoting Jia, John Ho, Daniel Nezich, Hyungbin Son, Vladimir Bulovic, Mildred S Dresselhaus, and Jing Kong. "Large area, few-layer graphene films on arbitrary substrates by chemical vapor deposition". In: *Nano letters* 9.1 (2008), pp. 30–35 (cit. on p. 31).

[150] Stephan Hofmann, Philipp Braeuninger-Weimer, and Robert S Weatherup. "CVD-enabled graphene manufacture and technology". In: *The journal of physical chemistry letters* 6.14 (2015), pp. 2714–2721 (cit. on p. 31).

[151] Pinshane Y Huang, Carlos S Ruiz-Vargas, Arend M Van Der Zande, William S Whitney, Mark P Levendorf, Joshua W Kevek, Shivank Garg, Jonathan S Alden, Caleb J Hustedt, Ye Zhu, et al. "Grains and grain boundaries in single-layer graphene atomic patchwork quilts". In: *Nature* 469.7330 (2011), p. 389 (cit. on pp. 31, 94).

[152] Adam W Tsen, Lola Brown, Mark P Levendorf, Fereshte Ghahari, Pinshane Y Huang, Robin W Havener, Carlos S Ruiz-Vargas, David A Muller, Philip Kim, and Jiwoong Park. "Tailoring electrical transport across grain boundaries in polycrystalline graphene". In: *Science* 336.6085 (2012), pp. 1143–1146 (cit. on p. 31).

[153] Zhigong Song, Vasilii I Artyukhov, Boris I Yakobson, and Zhiping Xu. "Pseudo Hall–Petch strength reduction in polycrystalline graphene". In: *Nano letters* 13.4 (2013), pp. 1829–1833 (cit. on p. 31).

[154] Péter Nemes-Incze, Péter Vancsó, Zoltán Osváth, Géza I Márk, Xiaozhan Jin, Yong-Sung Kim, Chanyong Hwang, Philippe Lambin, Claude Chapelier, and Laszlo PeterBiro. "Electronic states of disordered grain boundaries in graphene prepared by chemical vapor deposition". In: *Carbon* 64 (2013), pp. 178–186 (cit. on p. 31).

[155] F. Tuinstra and J. L. Koenig. "Raman Spectrum of Graphite". In: *The Journal of Chemical Physics* 53.3 (1970), pp. 1126–1130. ISSN: 0021-9606. DOI: 10.1063/1.1674108 (cit. on p. 31).

[156] Andrea C. Ferrari and Denis M. Basko. "Raman spectroscopy as a versatile tool for studying the properties of graphene". In: *Nature Nanotechnology* 8.4 (2013), pp. 235–246. DOI: 10.1038/nnano.2013.46. URL: https://doi.org/10.1038%2Fnnano.2013.46 (cit. on p. 31).

[157] M.S. Dresselhaus, A. Jorio, and R. Saito. "Characterizing Graphene, Graphite, and Carbon Nanotubes by Raman Spectroscopy". In: *Annual Review of Condensed Matter Physics* 1.1 (2010), pp. 89–108. ISSN: 1947-5454. DOI: 10.1146/annurev-conmatphys-070909-103919 (cit. on p. 31).

[158] R Saito, M Hofmann, G Dresselhaus, A Jorio, and MS Dresselhaus. "Raman spectroscopy of graphene and carbon nanotubes". In: *Advances in Physics* 60.3 (2011), pp. 413–550 (cit. on pp. 31, 32).

[159] Ado Jorio and Luiz Gustavo Cançado. "Perspectives on Raman spectroscopy of graphene-based systems: From the perfect two-dimensional surface to charcoal". In: *Physical Chemistry Chemical Physics* 14.44 (2012), pp. 15246–15256. ISSN: 14639076. DOI: 10.1039/c2cp42621h (cit. on p. 31).

[160] Ado Jorio and Antonio G. Souza Filho. "Raman Studies of Carbon Nanostructures". In: *Annual Review of Materials Research* 46.1 (2016), pp. 357–382. ISSN: 1531-7331. DOI: 10.1146/annurev-matsci-070115-032140 (cit. on p. 31).

[161] A. Gupta, G. Chen, P. Joshi, S. Tadigadapa, and P. C. Eklund. "Raman scattering from high-frequency phonons in supported n-graphene layer films". In: *Nano Letters* 6.12 (2006), pp. 2667–2673. ISSN: 15306984. DOI: 10.1021/nl061420a (cit. on p. 31).

[162] A. C. Ferrari and J. Robertson. "Interpretation of Raman spectra of disordered and amorphous carbon". In: *Physical Review B* 61.20 (2000), pp. 14095–14107. ISSN: 0163-1829. DOI: 10.1103/PhysRevB.61.14095. URL: https://link.aps.org/doi/10.1103/PhysRevB.61.14095 (cit. on p. 31).

[163] L. G. Cançado, M. A. Pimenta, B. R.A. Neves, M. S.S. Dantas, and A. Jorio. "Influence of the atomic structure on the Raman spectra of graphite edges". In: *Physical Review Letters* 93.24 (2004), pp. 5–8. ISSN: 00319007. DOI: 10.1103/PhysRevLett.93.247401 (cit. on p. 31).

[164] L. G. Cançado, K. Takai, T. Enoki, M. Endo, Y. A. Kim, H. Mizusaki, A. Jorio, L. N. Coelho, R. Magalhães-Paniago, and M. A. Pimenta. "General equation for the determination of the crystallite size La of nanographite by Raman spectroscopy". In: *Applied Physics Letters* 88.16 (2006), p. 163106. ISSN: 0003-6951. DOI: 10.1063/1.2196057. URL: http://aip.scitation.org/doi/10.1063/1.2196057 (cit. on p. 31).

[165] M. A. Pimenta, G. Dresselhaus, M. S. Dresselhaus, L. G. Cançado, A. Jorio, and R. Saito. "Studying disorder in graphite-based systems by Raman spectroscopy". In: *Phys. Chem. Chem. Phys.* 9.11 (2007), pp. 1276–1290. ISSN: 1463-9076. DOI: 10.1039/B613962K. URL: http://xlink.rsc.org/?DOI=B613962K (cit. on p. 31).

[166] Ado Jorio and Luiz Gustavo Cançado. "Disorder and Defects in Two-Dimensional Materials Probed by Raman Spectroscopy". In: *Springer Series in Materials Science*. Vol. 276. 2019, pp. 99–110. ISBN: 9789811318283. DOI: 10.1007/978-981-13-1828-3_5. URL: http://link.springer.com/10.1007/978-981-13-1828-3{_}5 (cit. on p. 31).

[167] Zhen Hua Ni, Ting Yu, Yun Hao Lu, Ying Ying Wang, Yuan Ping Feng, and Ze Xiang Shen. "Uniaxial strain on graphene: Raman spectroscopy study and band-gap opening". In: *ACS Nano* 2.11 (2008), pp. 2301–2305. ISSN: 19360851. DOI: 10.1021/nn800459e. arXiv: 0810.3476 (cit. on p. 31).

[168] TMG Mohiuddin, Antonio Lombardo, RR Nair, A Bonetti, G Savini, R Jalil, Nicola Bonini, DM Basko, C Galiotis, Nicola Marzari, et al. "Uniaxial strain in graphene by Raman spectroscopy: G peak splitting, Grüneisen parameters, and sample orientation". In: *Physical Review B* 79.20 (2009), p. 205433 (cit. on pp. 31, 97).

[169] Duhee Yoon, Young Woo Son, and Hyeonsik Cheong. "Strain-dependent splitting of the double-resonance raman scattering band in graphene". In: *Physical Review Letters* 106.15 (2011), pp. 1–4. ISSN: 00319007. DOI: 10.1103/PhysRevLett.106.155502. arXiv: 1103.3147 (cit. on p. 31).

[170] Ting Yu, Zhenhua Ni, Chaoling Du, Yumeng You, Yingying Wang, and Zexiang Shen. "Raman mapping investigation of graphene on transparent flexible substrate: The strain effect". In: *Journal of Physical Chemistry C* 112.33 (2008), pp. 12602–12605. ISSN: 19327447. DOI: 10.1021/jp806045u (cit. on p. 31).

[171] Andrea C. Ferrari. "Raman spectroscopy of graphene and graphite: Disorder, electron-phonon coupling, doping and nonadiabatic effects". In: *Solid State Communications* 143.1-2 (2007), pp. 47–57. ISSN: 00381098. DOI: 10.1016/j.ssc.2007.03.052 (cit. on p. 31).

[172] L. M. Malard, J. Nilsson, D. C. Elias, J. C. Brant, F. Plentz, E. S. Alves, A. H. Castro Neto, and M. A. Pimenta. "Probing the electronic structure of bilayer graphene by Raman scattering". In: *Physical Review B - Condensed Matter and Materials Physics* 76.20 (2007), pp. 1–4. ISSN: 10980121. DOI: 10.1103/PhysRevB.76.201401. arXiv: 0708.1345 (cit. on p. 31).

[173] A. Das, S. Pisana, B. Chakraborty, S. Piscanec, S. K. Saha, U. V. Waghmare, K. S. Novoselov, H. R. Krishnamurthy, A. K. Geim, A. C. Ferrari, and A. K. Sood. "Monitoring dopants by Raman scattering in an electrochemically top-gated graphene transistor". In: *Nature Nanotechnology* 3.4 (2008), pp. 210–215. ISSN: 17483395. DOI: 10.1038/nnano.2008.67. arXiv: 0709.1174 (cit. on p. 31).

[174] R. Saito, A. Jorio, A. G. Souza Filho, M. S. Dresselhaus, G. Dresselhaus, and M. A. Pimenta. "Probing Phonon Dispersion Relations of Graphite by Double Resonance Raman Scattering". In: *Physical Review Letters* 88.2 (2002), p. 4. ISSN: 10797114. DOI: 10.1103/PhysRevLett.88.027401 (cit. on p. 33).

[175] Ado Jorio Mildred S. Dresselhaus Gene Dresselhaus. *Group Theory*. Springer, 2019. ISBN: 3540821619. URL: https://www.xarg.org/ref/a/3540821619/ (cit. on p. 33).

[176] Nicola Ferralis. "Probing mechanical properties of graphene with Raman spectroscopy". In: *Journal of materials science* 45.19 (2010), pp. 5135–5149 (cit. on p. 33).

[177] Costas Galiotis, Otakar Frank, Emmanuel N Koukaras, and Dimitris Sfyris. "Graphene mechanics: current status and perspectives". In: *Annual review of chemical and biomolecular engineering* 6 (2015), pp. 121–140 (cit. on p. 33).

[178] William Hayes. *Scattering of Light by Crystals (Dover Science Books)*. Dover Publications, 1978. ISBN: 048643866X. URL: https://www.xarg.org/ref/a/048643866X/ (cit. on p. 36).

[179] M. Cardona. *Light Scattering in Solids II: Basic Concepts and Instrumentation (Topics in Applied Physics)*. Springer, 1982. ISBN: 3662311739. URL: https://www.xarg.org/ref/a/3662311739/ (cit. on p. 36).

[180] Bruno Pettinger, Philip Schambach, Carlos J. Villagómez, and Nicola Scott. "Tip-Enhanced Raman Spectroscopy: Near-Fields Acting on a Few Molecules". In: *Annual Review of Physical Chemistry* 63.1 (2012), pp. 379–399. ISSN: 0066-426X. DOI: 10.1146/annurev-physchem-032511-143807. URL: http://www.annualreviews.org/doi/10.1146/annurev-physchem-032511-143807 (cit. on p. 36).

[181] Naresh Kumar, Alasdair Rae, and Debdulal Roy. "Accurate measurement of enhancement factor in tip-enhanced Raman spectroscopy through elimination of far-field artefacts". In: *Applied Physics Letters* 104.12 (2014). ISSN: 00036951. DOI: 10.1063/1.4869184 (cit. on p. 36).

[182] Aroldo Ribeiro Neto, **Rabelo, Cassiano**, Luiz Gustavo Cancado, Michael Engel, Mathias Steiner, and Ado Jorio. "Protocol and reference material for measuring the nanoantenna enhancement factor in Tip-enhanced Raman Spectroscopy". In: *2019 4th International Symposium on Instrumentation Systems, Circuits and Transducers (INSCIT)*. 3. IEEE, 2019, pp. 1–6. ISBN: 978-1-7281-2109-3. DOI: 10.1109/INSCIT.2019.8868468. URL: https://ieeexplore.ieee.org/document/8868468/ (cit. on p. 37).

[183] R. S. Alencar, **Rabelo, Cassiano**, Hudson L. S. Miranda, Thiago L. Vasconcelos, Bruno S. Oliveira, Aroldo Ribeiro, Bruno C. Públio, Jenaina Ribeiro-Soares, A. G. Souza Filho, Luiz Gustavo Cançado, and Ado Jorio. "Probing Spatial Phonon Correlation Length in Post-Transition Metal Monochalcogenide GaS Using Tip-Enhanced Raman Spectroscopy". In: *Nano Letters* (2019). ISSN: 1530-6984. DOI: 10.1021/acs.nanolett.9b02974 (cit. on pp. 39, 89).

[184] Thorlabs. *Achromatic doublet antireflective coating graph*. URL: https://www.thorlabs.com/newgrouppage9.cfm?objectgroup_id=2696 (visited on Aug. 15, 2019) (cit. on p. 43).

[185] Lukas Novotny, Erik J. Sánchez, and X. Sunney Xie. "Near-field optical imaging using metal tips illuminated by higher-order Hermite–Gaussian beams". In: *Ultramicroscopy* 71.1-4 (1998), pp. 21–29. ISSN: 03043991. DOI: 10.1016/S0304-3991(97)00077-6. URL: https://linkinghub.elsevier.com/retrieve/pii/S0304399197000776 (cit. on pp. 47, 52).

[186] Thorlabs. *HeNe Laser mounted in C1512 Clamps on P6 Posts*. URL: https://www.thorlabs.com/newgrouppage9.cfm?objectgroup_id=1516 (visited on Nov. 2018) (cit. on p. 48).

[187] ARCoptix. *ARCoptix Polarization Converter*. URL: http://www.arcoptix.com/radial_polarization_converter.htm (visited on Nov. 2018) (cit. on p. 48).

[188] Merck Sigma Aldrich. *Nile Blue A perchlorate*. URL: https://www.sigmaaldrich.com/catalog/product/aldrich/370088 (visited on Feb. 20, 2019) (cit. on p. 52).

[189] Pascal Anger, Palash Bharadwaj, and Lukas Novotny. "Enhancement and quenching of single-molecule fluorescence". In: *Physical Review Letters* 96.11 (2006), pp. 3–6. ISSN: 00319007. DOI: 10.1103/PhysRevLett.96.113002 (cit. on p. 52).

[190] Hudson Miranda, **Rabelo, Cassiano**, Thiago L. Vasconcelos, Luiz Gustavo Cancado, and Ado Jorio. "Study of the interaction between light and nanoantennas in Tip-Enhanced Raman Spectroscopy". In: *2019 4th International Symposium on Instrumentation Systems, Circuits and Transducers (INSCIT)*. IEEE, 2019, pp. 1–5. ISBN: 978-1-7281-2109-3. DOI: 10.1109/INSCIT.2019.8868513. URL: https://ieeexplore.ieee.org/document/8868513/ (cit. on p. 53).

[191] Analog Devices. *Analog Devices AD549 Ultralow Input–Bias Current Operational Amplifier*. URL: https://www.analog.com/en/products/ad549.html (visited on May 2019) (cit. on p. 55).

[192] *Projeto MGgrafeno*. URL: https://www.mggrafeno.com.br/ (visited on Dec. 3, 2019) (cit. on p. 59).

[193] CamGraph. *Cambridge Nanosystems. CamGraph®G1*. URL: https://cambridgenanosystems.com/product/camgraph-g1 (visited on Jan. 2018) (cit. on p. 59).

[194] **Rabelo, Cassiano**, Hudson Miranda, Thiago L. Vasconcelos, Luiz Gustavo Cancado, and Ado Jorio. "Tip-enhanced Raman Spectroscopy of Graphene". In: *2019 4th International Symposium on Instrumentation Systems, Circuits and Transducers (INSCIT)*. IEEE, 2019, pp. 1–6. ISBN: 978-1-7281-2109-3. DOI: 10.1109/INSCIT.2019.8868627. URL: https://ieeexplore.ieee.org/document/8868627/ (cit. on pp. 64, 72).

[195] Ado Jorio and Luiz Gustavo Cançado. "Raman spectroscopy of twisted bilayer graphene". In: *Solid State Communications* 175-176 (2013), pp. 3–12. ISSN: 00381098. DOI: 10.1016/j.ssc.2013.08.008. URL: http://dx.doi.org/10.1016/j.ssc.2013.08.008https://linkinghub.elsevier.com/retrieve/pii/S0038109813003700 (cit. on p. 67).

[196] Ado Jorio, Mark Kasperczyk, Nick Clark, Elke Neu, Patrick Maletinsky, Aravind Vijayaraghavan, and Lukas Novotny. "Optical-phonon resonances with saddle-point excitons in twisted-bilayer graphene". In: *Nano letters* 14.10 (2014), pp. 5687–5692 (cit. on p. 68).

[197] Antenna Standards Committee of the IEEE Antennas and Propagation Society. *IEEE standard definitions of terms for antennas*. IEEE Std 145-1993, 1993 (cit. on p. 69).

[198] K Lance Kelly, Eduardo Coronado, Lin Lin Zhao, and George C Schatz. *The optical properties of metal nanoparticles: the influence of size, shape, and dielectric environment*. 2003 (cit. on p. 69).

[199] Stefan Alexander Maier. *Plasmonics: fundamentals and applications*. Springer Science & Business Media, 2007 (cit. on p. 69).

[200] Joel Henzie, Eun-Soo Kwak, and Teri W Odom. "Mesoscale metallic pyramids with nanoscale tips". In: *Nano letters* 5.7 (2005), pp. 1199–1202 (cit. on p. 70).

[201] Chein-I Chang. *Hyperspectral Data Processing*. 2013. ISBN: 9781118269787. DOI: 10.1002/9781118269787. URL: http://doi.wiley.com/10.1002/9781118269787 (cit. on p. 72).

[202] Ado Jorio, **Rabelo, Cassiano**, and J. L. Elias Campos. "Metallic device for scanning near-field optical microscopy and spectroscopy and method for manufacturing same". Pat. Patent Application. INPI, Brazil, Registration: BR512017000397-1. 2017 (cit. on p. 75).

[203] Nirmal Keshava. "A Survey of Spectral Unmixing Algorithms". In: *Lincoln Laboratory Journal* 14.1 (2003), pp. 55–78. ISSN: 0896-4130. DOI: 10.1109/LGRS.2014.2326555 (cit. on p. 75).

[204] Jie Yu, Dongmei Chen, Yi Lin, and Su Ye. "Comparison of linear and nonlinear spectral unmixing approaches: a case study with multispectral TM imagery". In: *International Journal of Remote Sensing* 38.3 (2017), pp. 773–795. ISSN: 13665901. DOI: 10.1080/01431161.2016.1271475 (cit. on p. 75).

[205] Laurens Van Der Maaten, Eric Postma, and Jaap Van den Herik. "Dimensionality reduction: a comparative". In: *J Mach Learn Res* 10.66-71 (2009), p. 13 (cit. on p. 75).

[206] Chein I. Chang, Chao Cheng Wu, and Ching Tsorng Tsai. "Random N-finder (N-FINDR) endmember extraction algorithms for hyperspectral imagery". In: *IEEE Transactions on Image Processing* 20.3 (2011), pp. 641–656. ISSN: 10577149. DOI: 10.1109/TIP.2010.2071310 (cit. on pp. 75, 77).

[207] D. Heinz, C.-I. Chang, and M.L.G. Althouse. "Fully constrained least-squares based linear unmixing". In: *IEEE 1999 International Geoscience and Remote Sensing Symposium. IGARSS'99 (Cat. No.99CH36293)* 2 (1999), pp. 0–2. DOI: 10.1109/IGARSS.1999.774644 (cit. on p. 77).

[208] Christian Therien. *PySptools - Hyperspectral algorithms for Python*. https://sourceforge.net/projects/pysptools/. 2013. URL: https://sourceforge.net/projects/pysptools/ (visited on Feb. 5, 2018) (cit. on p. 77).

[209] *Peak-o-Mat*. URL: https://sourceforge.net/projects/lorentz/ (visited on Dec. 19, 2017) (cit. on p. 78).

[210] L. Zhang, N. F. Heinig, S. Bazargan, M. Abd-Ellah, N. Moghimi, and K. T. Leung. "Direct-write three-dimensional nanofabrication of nanopyramids and nanocones on Si by nanotumefaction using a helium ion microscope". In: *Nanotechnology* 26.25 (2015). ISSN: 13616528. DOI: 10.1088/0957-4484/26/25/255303 (cit. on p. 82).

[211] Ado Jorio, Marcia M. Lucchese, Fernando Stavale, Erlon H.Martins Ferreira, Marcus V.O. Moutinho, Rodrigo B. Capaz, and Carlos A. Achete. "Raman study of ion-induced defects in N -layer graphene". In: *Journal of Physics Condensed Matter* 22.33 (2010). ISSN: 09538984. DOI: 10.1088/0953-8984/22/33/334204 (cit. on p. 83).

[212] João Luiz Elias Campos, Hudson Miranda, **Rabelo, Cassiano**, Emil Sandoz-Rosado, Sugandha Pandey, Juha Riikonen, Abraham G. Cano-Marquez, and Ado Jorio. "Applications of Raman spectroscopy in graphene-related materials and the development of parameterized PCA for large-scale data analysis". In: *Journal of Raman Spectroscopy* 49.1 (2018), pp. 54–65. ISSN: 03770486. DOI: 10.1002/jrs.5225. URL: http://doi.wiley.com/10.1002/jrs.5225 (cit. on pp. 94, 98).

[213] RHK Technology. *RHK R9 SPM Controller*. URL: https://www.rhk-tech.com (visited on Nov. 15, 2018) (cit. on p. 123).

[214] Vishal Panchal, Cristina E Giusca, Arseniy Lartsev, Nicholas A Martin, Nathan Cassidy, Rachael L Myers-Ward, D Kurt Gaskill, and Olga Kazakova. "Atmospheric doping effects in epitaxial graphene: correlation of local and global electrical studies". In: *2D Materials* 3.1 (2016), p. 015006. DOI: 10.1088/2053-1583/3/1/015006 (cit. on p. 131).

[215] Fran Cverna et al. *ASM ready reference: thermal properties of metals*. ASM International, 2002 (cit. on p. 132).

[216] Ben Fry and Casey Reas. *Processing Software*. URL: https://processing.org/ (visited on Oct. 15, 2019) (cit. on p. 135).

[217] M Klein and G Schwitzgebel. "An improved lamellae drop-off technique for sharp tip preparation in scanning tunneling microscopy". In: *Review of scientific instruments* 68.8 (1997), pp. 3099–3103 (cit. on p. 139).

TECHNICAL APPENDICES

A

The SPM Controller - RHK R9

Here we show how the TERS system is connected to the SPM controller RHK R9. Additional details on how each item listed here works is provided by [37].

The TERS system, as described in Section 3.1, consists of a SPM system integrated with an optical microscopy system. A central component of this system is the SPM controller, whose function is to coordinate the communication of all electronic devices which are connected to it, reading the data generated by the various sensors and calculating and acting upon the received data, mostly in real time. Such unity is also responsible for providing electrical power no only to most low voltage components, such as preamplifiers, but also the high voltage needed to control the piezoelectric elements located in the scanhead (X, Y and Z piezoelectric elements), which act to position the tip. Among its functionalities, it is deserved to highlight: the movement of the scanning stage, count the transitor-transistor logic (TTL) pulses sent by the APD, operate the feedback loop needed for the atomic force microscope, which is done with its integrated phase-locked loop (PLL) system, as well as manage the bias voltage and act upon the voltage readings provided by the preamplifier when operating in STM mode, in addition to providing basic integration with the spectrometer in order to perform the acquisition of hyperspectral images.

RHK R9 / TERS SCANHEAD: CONNECTION DIAGRAM

DIGITAL I/O 25-PIN CONNECTOR (I/O #1)

6 TTL OUT (Handshake)
To "ext. trigger" in the spectrometer

20 TTL IN (Handshake)
To "fire" in the spectrometer

7 Picomotor (inchworm)
Clock (laranja)

8 Picomotor (inchworm)
Direction (vermelho)

● PINs 1, 2, 3, 13, 14, 15, 25
GND (picomotor: fio marrom)

SPECTROMETER

PICOMOTOR

LOW VOLTAGE OUTPUTS 15-PIN CONNECTOR

8 X STAGE
7 Y STAGE

● PINs 2, 4, 10, 12, 13, 14, 15
GND

MCL STAGE

DC POWER OUTPUT 9-PIN CONENECTOR

1 5 V
Power to first amplification stage

4 +15 V
Power to second amplification stage

5 -15 V
Power to second amplification stage

● PINs 3, 6, 7, 8, 9
GND

SCANHEAD

REAR PANEL CHANNEL 2 BNCs

CH2

INPUT   PREAMP

DRIVE   MOD.

● INPUT (10 V Hi Z)
From SCANHEAD
(Amplified tuning-fork signal)

● DRIVE
To SCANHEAD DITHER

SCANHEAD

Laboratório de NANO.ESPECTROSCOPIA

REAR PANEL PULSE COUNTING

PULSE COUNTING

A APD 01
B APD 02

APD

HIGH VOLTAGE OUTPUT 10-PIN CONNECTOR

B +X OFFSET   **F** +Y OFFSET
D - X OFFSET   **G** -Y OFFSET
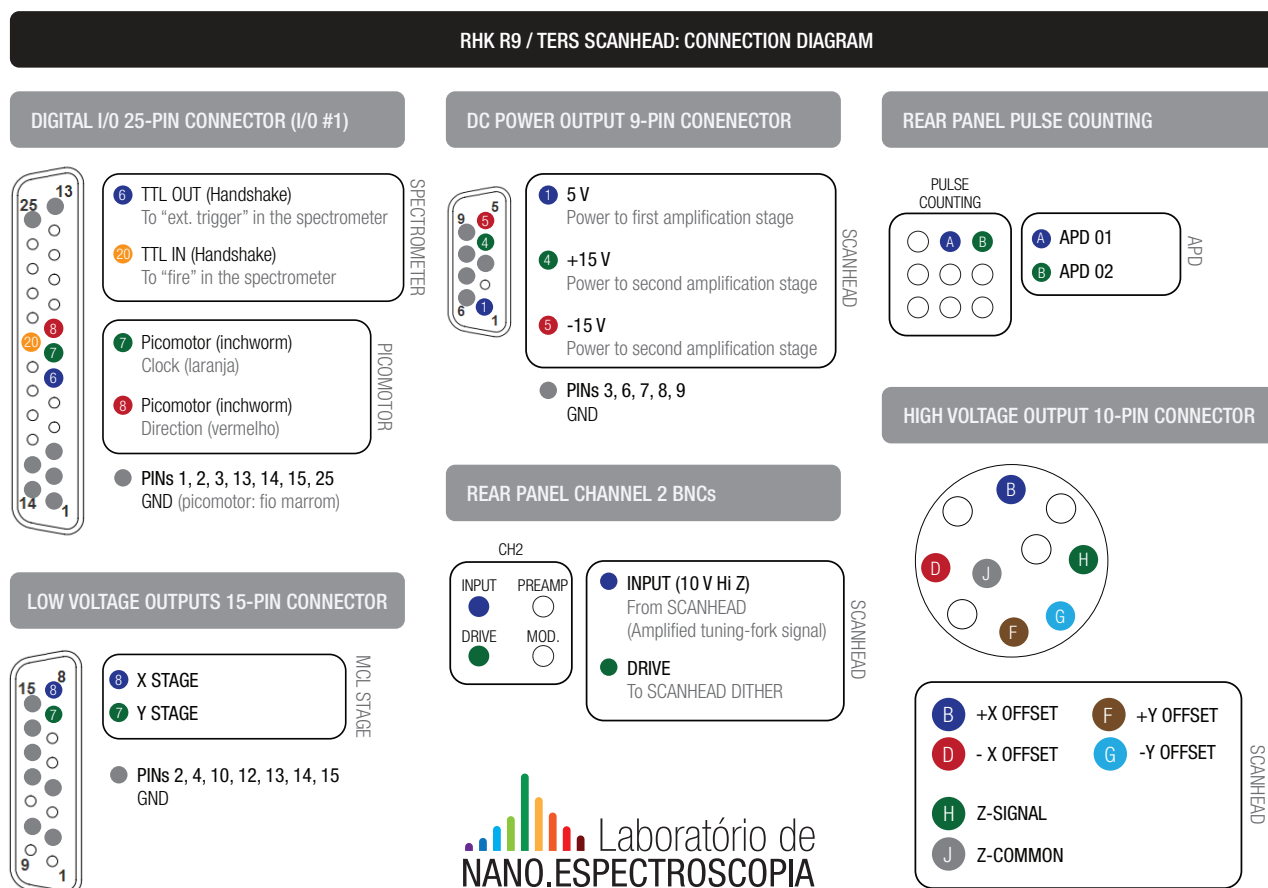
H Z-SIGNAL
J Z-COMMON

SCANHEAD

FIGURE A.1: Schematic diagram showing all the inputs/outputs needed to fully operate the TERS system in AFM-TERS mode.

Figure A.1 shows a schematic representation of the inputs/outputs (I/Os) provided at the back panel of the R9 controller that are used by our TERS system, as well as to which hardware item they are connected.

The previous system, describe throughly in [37], used a RHK Technology's SPM1000 controller. Built on analog technology and developed in the 1990s, this controller had limited configuration options, no internal PLL and lock-in systems, was no longer manufactured and had its hardware and software support disrupted. Therefore it was decided that the acquisition of a new controller was necessary. It was opted for the acquisition of the R9 Controller, also from RHK, which had as advantages over competitors the fact of integrating voltage sources, amplifiers, PLLs, lock-ins, pulse counters, among other features, in a single all-digital unit. The disadvantage is that this unit needed to be fully adapted and programmed for use with LabNS's homebuilt TERS system.
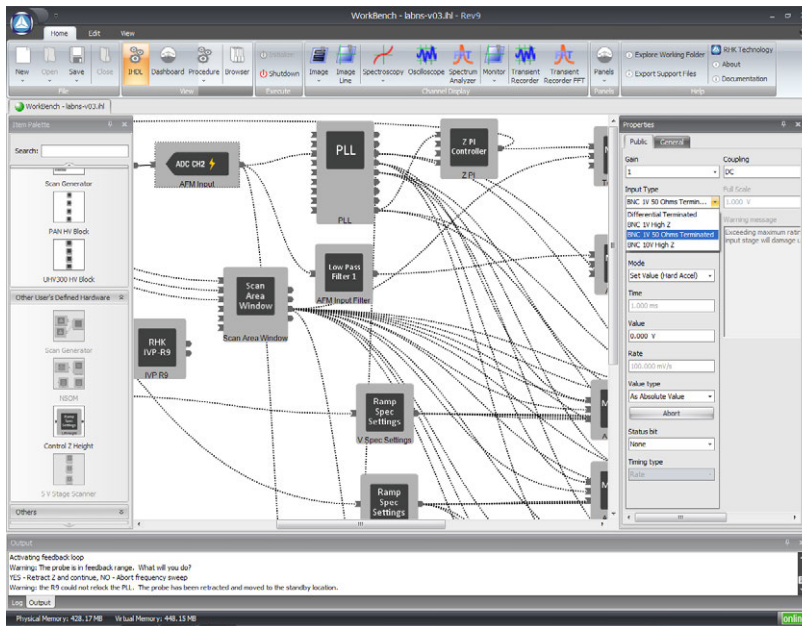
FIGURE A.2: R9 control software interface displaying a portion of the IHDL programmed.

The R9 is completely software configurable. It provides a programming module as an integral part of the software accompanying the system. Its graphical interface adopts a drag-and-drop paradigm with icons representing the hardware elements that make up the system. Named IHDL – Iconic Hardware Description Language – this language allows the configuration of virtually all aspects of the controller, such as: which outputs to use; voltage levels provided; how to act on received data on certain input. Most of the configuration is done graphically, with little textual programming needed. Figure A.2 shows the screen shot from the IHDL used to control the TERS system.

FIGURE A.3: Illustration showing the connections responsible for the mechanical excitation of the scanhead, needed for the AFM, and the SPM controller. A dither, made from a piece of a piezoelectric element, is excited by a sinusoidal signal oscillating at the same frequency as the tuning fork resonant frequency. The signal from the 1st amplification stage (V_{out}) is connected to a 2nd amplification stage, which is finally connected to channel 2 input of the RHK R9 SPM controller (3D model of the scanhead was provided by Vitor Monken).
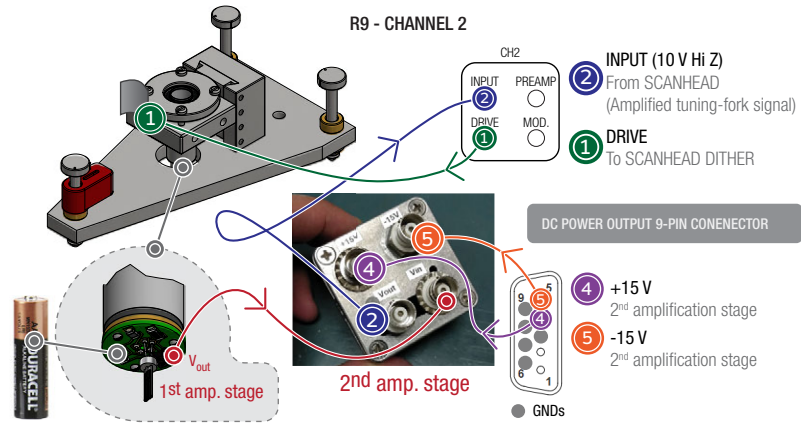
The R9 is provided with an internal PLL system. The PLL sends a driving sinusoidal signal (pin 1 on the CH2 panel) to drive the dither piezo and collects the TF signal through an input port (pin 2 on the CH2 panel). Before the TF signal can be fed back to the R9 it must be amplified due to its very low amplitude. This is done by two amplifying stages. The first stage contains the tip and requires a voltage supply, which is provided by a AA battery. The output of the first stage is sent directly to a second stage, outside the scanhead, which demands symmetric voltage supply (pins 4 and 5 from the DC power output panel). The final output from the amplifying stages then goes back to the CH2 panel on pin 2, reserved for the AFM input to the controller.

FIGURE A.4: Diagram of high voltage connections that drive the piezoelectric elements responsible for moving the probe along X, Y and Z. The positioning system consists of two piezo tubes which are manually soldered with enameled wires. The upper tube is responsible for moving the probe along the X/Y plane and the lower one is responsible solely for Z axis moving.
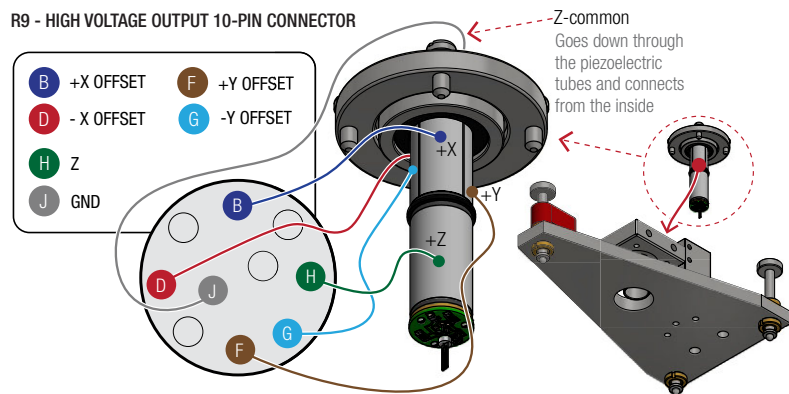
The piezo stack, constituted of two piezo tubes: one for movement along the XY plane and another dedicated for the Z axis. The B-D and F-G connection pairs generate symmetric voltages that expand and contract opposite faces in the tube to bend the whole construct in order to produce the desired movements in the X/Y plane. The Z signal transmitted by the H pin expands and contracts the Z tube entirely, generating position displacement along the said axis. All these connections are made with enameled wires soldered directly to the piezo faces.
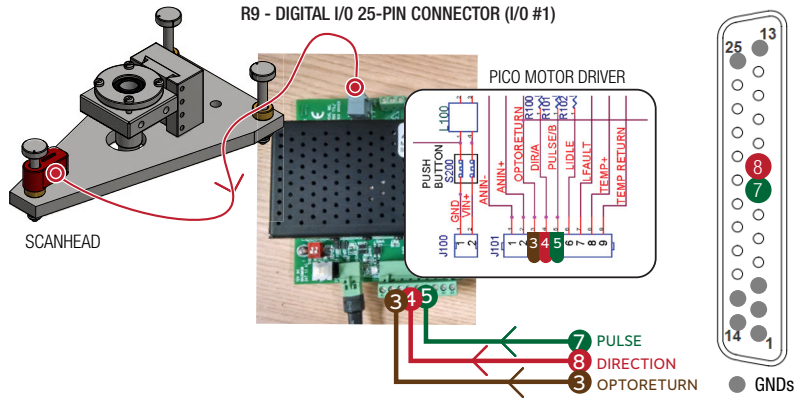
FIGURE A.5: Connection schematic for the picomotor driving system. The R9's digital I/O is used to interface with a proprietary driver which actually controls the picomotor.

The picomotor is also controlled by the R9 via its digital I/O. Pins 8 and 7 generate digital pulses which are interpreted by the picomotor's proprietary driver. This unit converts these digital commands to the proper high voltage pulses necessary to produce rotation. The picomotor employed in the system behaves similarly to a stepper motor and, for each pulse sent through pin 7, it performs a step, with the direction of said step being determined by pin 8.
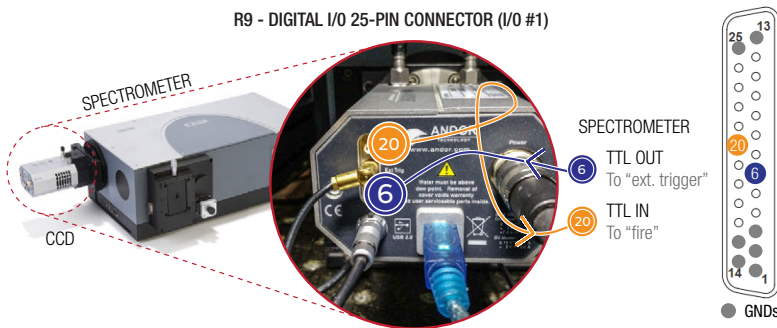
FIGURE A.6: The spectrometer's CCD camera can be synced with movements of the scan table or the probe. This synchronization is handled by two TTL signals: TTL OUT which triggers a CCD acquisition and a TTL IN which is enabled by the CCD when it is ready for an acquisition.

For procedures such as hyperspectral image scanning and tip approach curves, it is necessary to have the spectrometer in sync with the controller. The connections for this functionality are also present on the R9's digital I/O panel. The TTL OUT (pin 6 in the digital I/O panel) is sent by the controller to the CCD in order to trigger the acquisition of a single spectrum. The TTL IN (pin 20 in the digital I/O panel) is sent by the CCD to the controller in order to communicate that it is ready to acquire a new spectrum.

FIGURE A.7: The APD is connected to a digital pulse counting input in the R9's panel. The frequency of the generated pulses is related to the optical signal intensity reaching the sensor's surface.
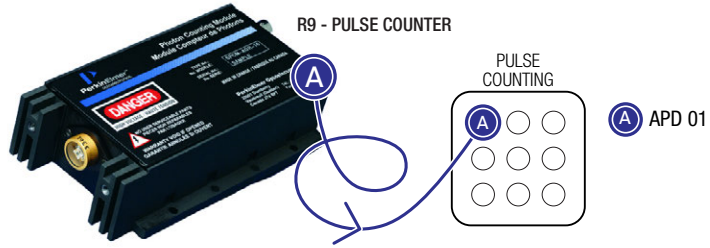
The APD is connected through its "Signal Out" BNC to the "Pulse Counting A" of R9. As already explained, at each detected photon, the APD emits a TTL pulse. Such pulses are read, counted and used by the controller for line and image generation.

FIGURE A.8: The scan table position is controlled by two low voltage signals, one for each axis, that are sent by the R9 controller to a proprietary driver.
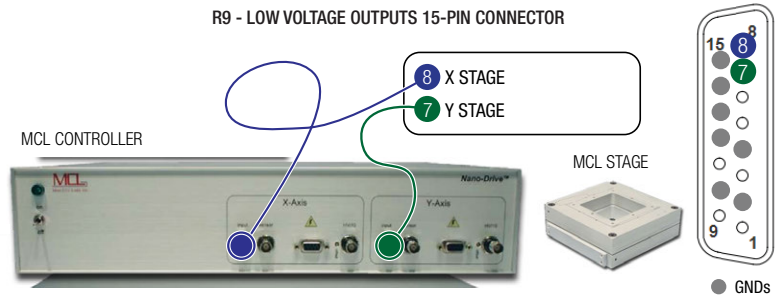
The nanopositioning stage is driven by a proprietary driver which receives low voltage signals (± 5 V) that are directly mapped to position displacement by the driver unit. The stages's X and Y position are controlled by pins 8 and 7 from the low voltage output panel. These signals ranging from -5 to $+5$ V are then converted to positions in the range of -25 to $+25$ µm.
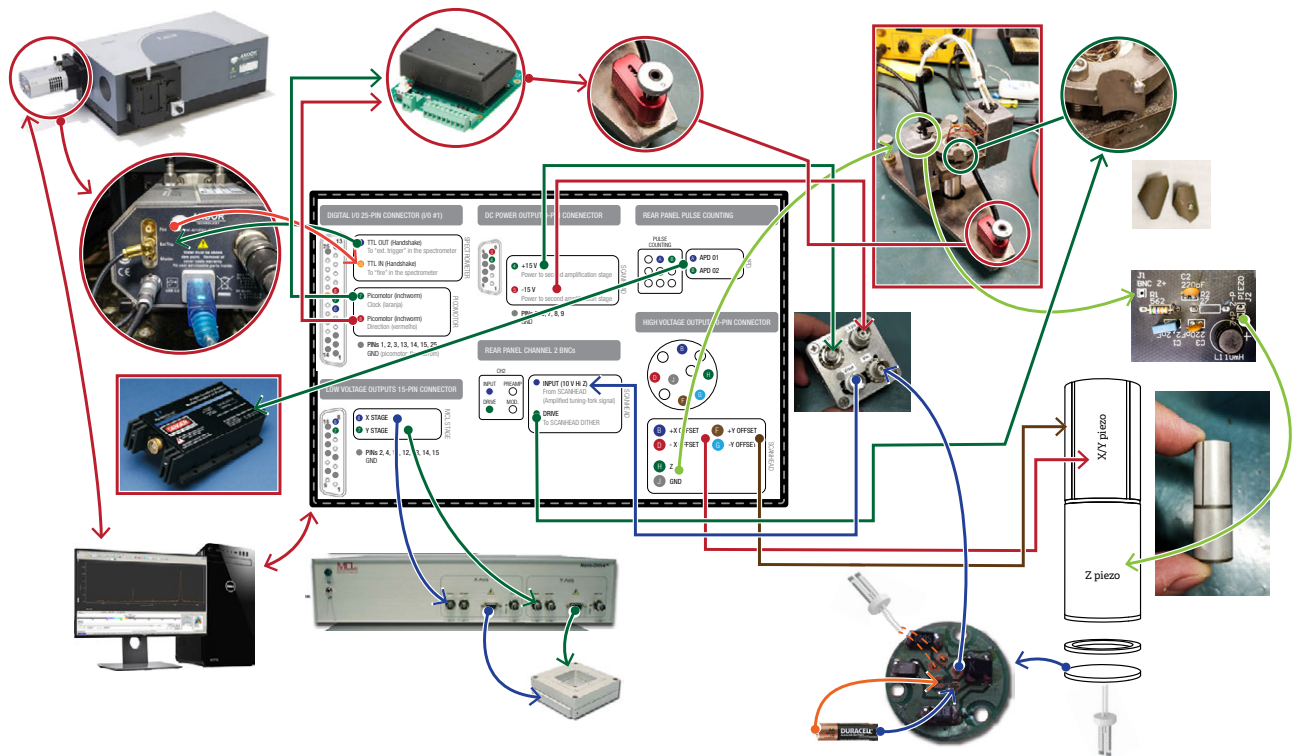
Finally, Figure A.9 showcases all the electric connections that are required for the system to function properly. This enables the general purpose R9 SPM controller to perform experiments comprehending: confocal microscopy, AFM and SNOM. Additional information regarding the R9 SPM controller can be found in [213].

FIGURE A.9: Overview showing all the elements connected to the SPM controller and necessary in order to have a fully working TERS system.

B

Optical and Optomechanical Elements

Following are five tables with all the optical and optomechanical components used in the assembly, one for each optical path according to Section 3.1.1, one for the optomechanicals items used to hold and align the optical related elements, such as lenses, mirror, etc. and one last table listing the cameras and attached optics used in the tip/sample visualization.

TABLE B.1

OPTICAL COMPONENTS USED IN THE "LASER TO MICROSCOPE" PATH

ITEM	ITEM #/CODE	MAKER	LABEL (Figure 3.1)
Laser HeNe 632.8 (21 mW)	HNL210L	Thorlabs	LASER
632.8 nm laser clean-up filter (laser line)	LL01-633-12.5	Semrock	F1
Achromatic doublet lens (f = 30 mm)	AC254-030-A-ML	Thorlabs	L1
Achromatic doublet lens (f = 250 mm)	AC254-250-A-ML	Thorlabs	L2
Arcoptix Radial Polarization Converter	RPC	Arcoptix	O1
Achromatic doublet lens (f = 40 mm)	AC254-040-A-ML	Thorlabs	L3
Pinhole (25 μm)	P25D	Thorlabs	P1
Achromatic doublet lens (f = 60 mm)	AC254-060-A-ML	Thorlabs	L4
Dielectric mirror	BB1-E02	Thorlabs	-
Neutral density filters (ND = 0.6, ND=1, ND=2, ND= 3, ND=4)	NEXXXB series: 506, 510, 520, 530, 540	Thorlabs	ND
Berek's Variable Wave Plate	5540M	Newport	O2
Nikon Eclipse Ti-U inverted microscope	-	Nikon	-
632.8 nm RazorEdge Dichroic laser beam-splitter	LPD02-633RU	Semrock	F2
			Continue...

ITEM	ITEM #/CODE	MAKER	LABEL (Figure 3.1)
Nikon Plan Apochromat VC Objective, 60x, 1.4 NA, Oil (Figure B.1(a))	-	Nikon	OBJ
Microscopy oil Cargill #16242 or #16482 (Figure B.1(b))	-	Cargill	-
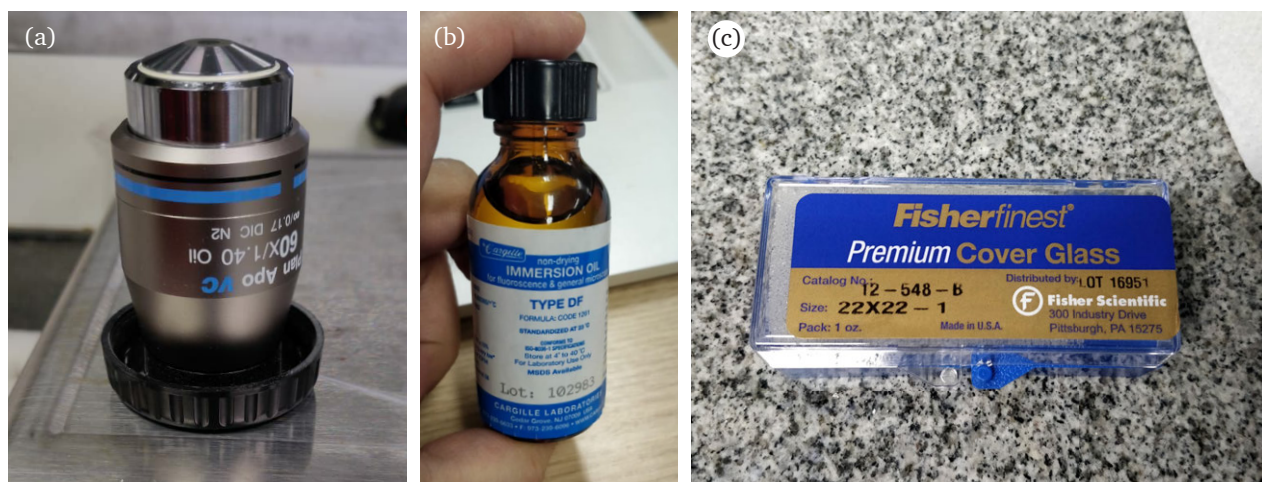
FIGURE B.1: (a) The microscope objective used in the system is a Nikon Plan Apochromat VC Objective, 60x, 1.4 NA, Oil. (b) The immersion oil used is a cargill #16242 or #16482. (c) The microscopy coverslips are from Fisherfinest Premium cover glass model #12-548B, measuring 22×22 mm and with an approximate thickness of 0.13 to 0.17 mm.

TABLE B.2

OPTICAL COMPONENTS USED IN THE "MICROSCOPE TO SPECTROMETER" PATH

ITEM	ITEM #/CODE	MAKER	LABEL (Figure 3.1)
Pinhole (75μm)	P75D	Thorlabs	P2
Achromatic Doublet ($f = 150$ mm)	AC254-150-B-ML	Thorlabs	L6
633 nm long-pass filter	LP02-633RU-25	Semrock	F3
Achromatic Doublet ($f = 30$ mm)	AC254-030-B-ML	Thorlabs	L7
Andor Shamrock Spectrometer	SR-303i	Andor	ESP...
CCD for spectrography	iDus DU401A-BR-DD	Andor	-

TABLE B.3

OPTICAL COMPONENTS USED IN THE "MICROSCOPE TO APD" PATH

ITEM	ITEM #/CODE	MAKER	LABEL (Figure 3.1)
Pinhole (75 μm)	P75D	Thorlabs	P3
Achromatic Doublet ($f = 200\,\text{mm}$)	AC254-200-B-ML	Thorlabs	L9
633 nm long-pass filter	LP02-633RU-25	Semrock	F3
Achromatic Doublet ($f = 100\,\text{mm}$)	AC254-100-B-ML	Thorlabs	L10
Bandpass filters	Assorted from various vendors	-	F4
APD	SPCM-AQRH-14	Excelitas	APD

TABLE B.4

OPTOMECHANICAL COMPONENTS USED IN THE SYSTEM

ITEM	ITEM #/CODE	MAKER
pneumatic vibration isolators	Series I-2000	Newport
Post V-Clamp Mount	C1512	Thorlabs
Ø1.5" Mounting Post	P6	Thorlabs
Studded Pedestal Base Adapter	PB4	Thorlabs
Clamping Fork Ø1.5"	PF175	Thorlabs
Clamping Fork, 1.24"	CF125	Thorlabs
Ø1.25" Studded Pedestal Base Adapter	BE1	Thorlabs
Mounting Base	BA1 & BA2	Thorlabs
Table Clamp, L-Shape	CL5	Thorlabs
Ø1/2" Post Holder	PH2	Thorlabs
Kinematic Mirror Mount Ø1"	KM100	Thorlabs
Translating Lens Mount Ø1"	LM1XY	Thorlabs
1" XYZ Translation Stage	PT3	Thorlabs
Lens Mount with Retaining Ring Ø1"	LM1XY	Thorlabs
Lens Mount with Retaining Ring Ø1"	LMR1	Thorlabs

ITEM	ITEM #/CODE	MAKER
High-Performance Low-Profile Ball Bearing Linear Stage	M-423	Newport
Spatial Filter System	KT310	Thorlabs
30 mm Cage Filter Wheel Six Ø1" Filters	CFW6	Thorlabs
Ø1.5" Mounting Post	P12	Thorlabs
Complete Periscope Assembly	RS99	Thorlabs
Tip/Tilt Rotation Beam Steering Assembly	RS99T	Thorlabs
Microscopy Cube Assembly Nikon	TLV-TE2000	Thorlabs
Articulating Base Ball Stage	SL20	Thorlabs
Flip Mount Adapter	FM90	Thorlabs
Nano-H50 nanopositioning stage	Nano-H50	Mad City Labs
2-channel Nano-Drive	Nano-Drive Series	Mad City Labs

TABLE B.5

COMPONENTS FOR IMAGE ACQUISITION

ITEM	ITEM #/CODE	MAKER
USB 2.0 CMOS Camera	DCC1645C	Thorlabs
C-Mount Adapter for 6.5x and 12x Zoom Lens Extension Tubes	MVLCMC	Thorlabs
2.00x Extension Tube for 6.5x and 12x Zoom Lenses	MVL20A	Thorlabs
12x Zoom Lens with 12 mm Fine Focus	MVL12X12Z	Thorlabs

C

Environmental Improvements & System Automation

Any precision optical system, as well as SPM systems, should be installed in a quiet, vibrationless ambient with controlled lighting, temperature and humidity. Here we describe improvements implemented not only to the system itself, but also to the environment where the system is located.

FIGURE C.1: (a) Photograph of the TERS system where can be seen the inverted microscope(1), the monitor with a view from the long distance microscope (2) and the sliding metal door in its open position (3). In (b) the metal box is closed (3) and the system is ready for measurement. The room has an air-conditioning unity (4) and a dehumidifier (5). Under the metal housing one of the five pneumatic feet can be seen (6). The optical elements placed outside the metal housing are covered by an optical plastic cover from Thorlabs (7). These optical elements are shown uncovered in Figure 3.3.

C.1 VIBRATION ATTENUATION

An environment free of external vibrations is essential for most optical and SPM applications. When working in the micro and nanoscale, even small vibrations in the micrometer range can be hampering to system utilization. An optical setup, which usually consists of a diverse number of individual optomechanical elements with a precise alignment in relation to each other, where even the smallest positional deviations add up to an unusable misaligned system, are specially prone to vibrational movement and therefore must be fixed in an ambient as stable as possible. For this reason the entire TERS

system is assembled over an optical table made from a solid granite slab and elevated by five pneumatic vibration isolators. Measuring $280 \times 150 \times 20$ cm (L x W x H) and with an estimated weight of ≈ 2300 kg this optical table was custom made in a time where importing a commercially available optical table to Brazil was too expensive. Despite the apparent advantage from an unusual mass when compared to most commercially available products,[1] this optical table presents a large number of surface irregularities, making it difficult to align the optical elements, although it does not impair its vibration attenuation capabilities, which is the main factor after all. However, commercially available optical tables with enough surface area to fit all the elements needed, would serve the purpose as well.

The pneumatic vibration isolators used are designed to reduce high-frequency vibrations coming from the ground and are supplied by a continuous flow of compressed air that must be able to provide a minimum of 10 and maximum of 85 PSI, which guarantees a vertical resonance frequency of less than 1.1 Hz and a horizontal resonance frequency of less than 1.5 Hz at 80 PSI, according to the manufacturer. It is important to note that while some commercially available Raman/SPM systems recommend or require the installation over optical tables in order to work properly, others ship with different solutions, such as active vibration isolation, which are electronically controlled.

In order to further isolate the system from external interference, a metal housing with dimensions equal to $130 \times 175 \times 175$ cm (L x W x H), built from extruded aluminum profiles and covered by aluminum sliding doors, was assembled around part of the optical table. It is paramount to make sure that this metal housing does not touch the optical table surface, in order not to transfer any vibrations from the ground to the table. Although not completely sealed from the outside, this metal housing is able to attenuate light that might be coming from the outside,[2] as well as acoustic vibrations and electromagnetic interference due to its grounded metallic surface, although it does not work as a proper Faraday cage.

[1]Most commercially available optical tables with approximately the same dimensions weight around 700 to 900 kg.

[2]The entire system, including the metallic enclosure can be kept completely isolated from external light, since it is located on a room surrounded by proper curtains.

C.2   Temperature and humidity control

The room where the system was previously installed had air-conditioning available, however the single existing unit was shared by more then one optical table and the movement of people in and out of the room disturbed the airflow, as well as temperature and lighting conditions. A change in the layout was proposed where, through the use of curtains, each optical table in the lab, including the one dedicated to the TERS system, could be separated from the rest of the lab. Individual split-system air conditioning units, each with 12 000 BTU[3], were installed at each curtain delimited areas. Although the curtains do not provide relevant noise attenuation, they act as an excellent light and airflow barrier. Another source of problem was the excessive ambient humidity, which was, as measured, on average above 60 %RH. Albeit ambient humidity usually does not pose a problem for ultra-high vacuum (UHV) systems, our system operates in ambient conditions, where humidity variations during an experiment could affect the results. Graphene, for example, has some of its properties directly affected by atmospheric conditions [214]. Excessive humidity is also harmful to optical components, specially the thin film coatings present in most lenses and therefore should be avoided, as per manufacturer recommendations. In order to provide a satisfactory humidity control, a dehumidifier unit with a 12 L/d at 30 °C and 80 %RH capacity, according to the manufacturer, was installed inside the curtain delimited area.

[3]BTU: British Thermal Unit.

With those physical improvements in place, it was implemented a temperature and humidity monitoring and logging system. For that we used the module DHT22, a capacitive-type relative humidity and temperature sensor module. The sensing element is connected to a 8-bit single-chip microcontroller temperature compensated and factory calibrated, provided with a sensing period of only 2 s and resolution of 0.1 %RH and 0.1 °C, according to the manufacturer datasheet. The DHT22 is wired to an Arduino Nano microcontroller responsible for reading the sensor's data and transferring the data to the computer (see Appendix C.4). The sensor is located in a strategic position on top of the casted metal base on the microscope(Figure C.2(c)), close to sample and to the scanhead and away from any external source of heat.

Temperature variation poses a problem in two fronts: (1) thermal expansion of mechanical parts and (2) variations in the operation of electronic components and systems. Regarding (1), the atoms

forming any material present a temperature based distance variation. Most materials present a volume expansion under a temperature increase and this variation can be quantified based on the material's Coefficient of thermal expansion (CTE). Given the CTE, the material's linear expansion can be calculated by

$$\Delta L = L \times \alpha \times \Delta T \ , \tag{C.1}$$

where ΔL is the variation in the object's length, L is the object's original length, α is the CTE and ΔT is the temperature variation. As an example, let's consider stainless steel, the material utilized in the manufacturing of our SPM scanhead; stainless steel has an $\alpha \approx 10 \times 10^{-6}\,°\mathrm{C}^{-1}$ (CTE) [215]. Considering that the scanhead longitudinal length $L = 180\,\mathrm{mm}$, a ΔT variation of only $1\,°\mathrm{C}$, results in a $\Delta L \approx 1.8\,\mathrm{\mu m}$. Considering that a TERS nanoantenna has an apex diameter of approximately $10 \times 10^{-3}\,\mathrm{\mu m}$, a $2\,\mathrm{\mu m}$ variation in only $1\,°\mathrm{C}$ is very representative, which justifies the environmental control measures taken. Electronic components are also impacted by temperature variation. If we take for example the AD549 opamp used in the design of the STM current preamplifier (see Section 3.2.1), according to its datasheet the "*bias current increases by a factor of* 2.3 *for every 10ºC rise in temperature*", considering a initial temperature of $25\,°\mathrm{C}$). The increase factor is significant and cannot be overlooked, specially considering the high gain (10^9) of the preamp, which further justifies the environmental measures taken.
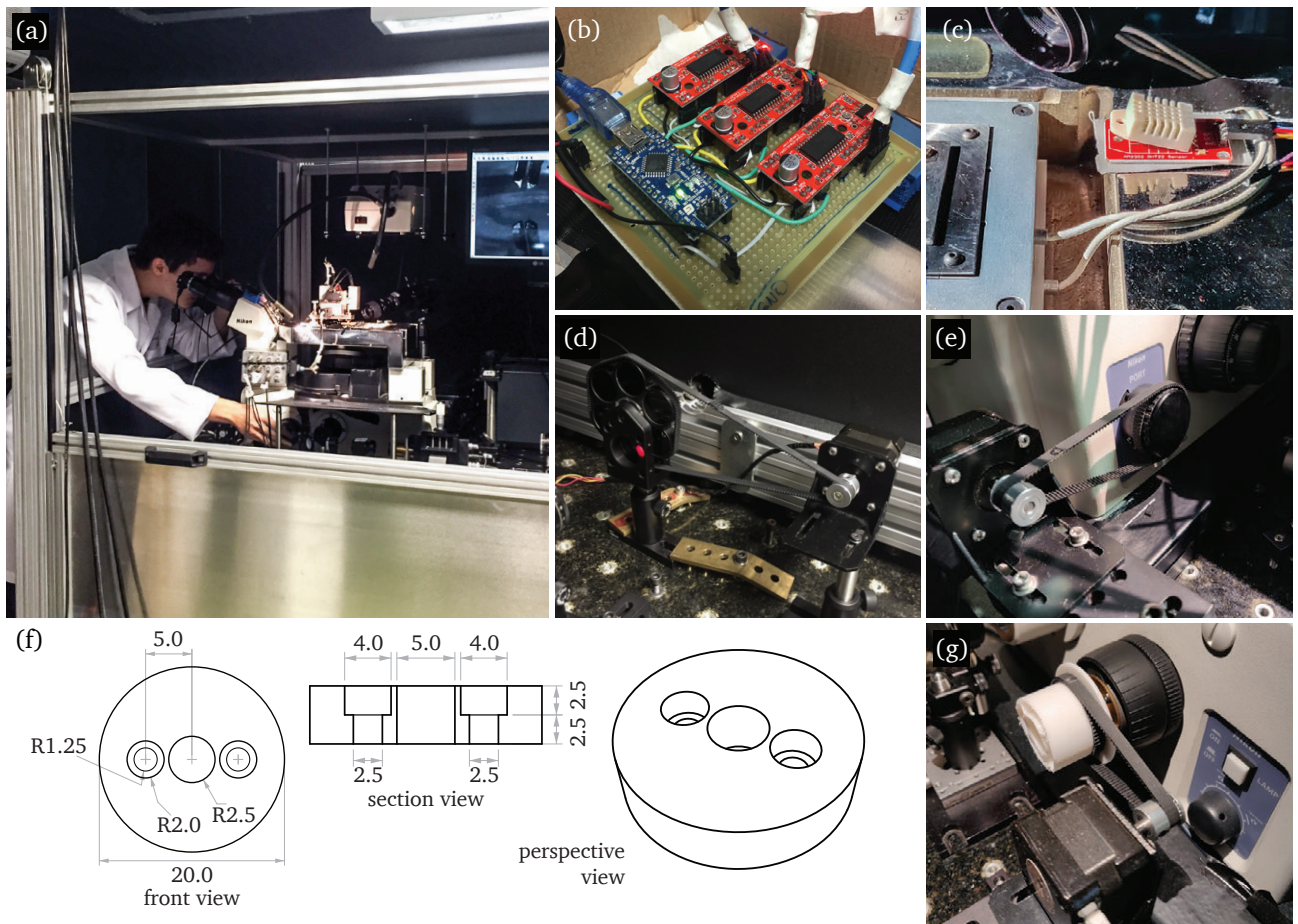
C.3 MICROSCOPE AUTOMATION

FIGURE C.2: (a) Operator using the microscope before motorization. (b) Arduino Nano and the three stepper motor drivers. (c) DHT22 temperature and humidity sensor on top of the microscope "anvil". (d) filter wheel, (e) optical path selector knob and (g) fine focus wheel, all coupled to stepper motors. (f) technical drawing of brass piece designed to couple the stepper to the fine focus.

The TERS system has several elements that need frequent adjustments at any given moment. For example, while conducting an experiment, it is necessary to manually manipulate not only the microscope focus wheel, which is responsible for translating the microscope objective, but also the optical path selector knob, as well as the filter wheel, where an assortment of neutral density filters are used to adjust the laser power incident on the sample. As described in Section 3.1, the inverted microscope with the SPM scanhead, as well as the photon detectors (i. e. APD and spectrometer) are located inside a metal housing with sliding doors. During the measurements, it is of paramount importance to keep the doors shut to mitigate, as previously explained, external disturbances such as drafts, undesired ambient lighting and to attenuate external noise. The handling of any of the adjustable elements requires opening one or more of the sliding doors, which may endanger the integrity of the nanoantenna and the sample. In addition, due to the need for frequent adjustments, the operator must remain in the same environment as the TERS system,
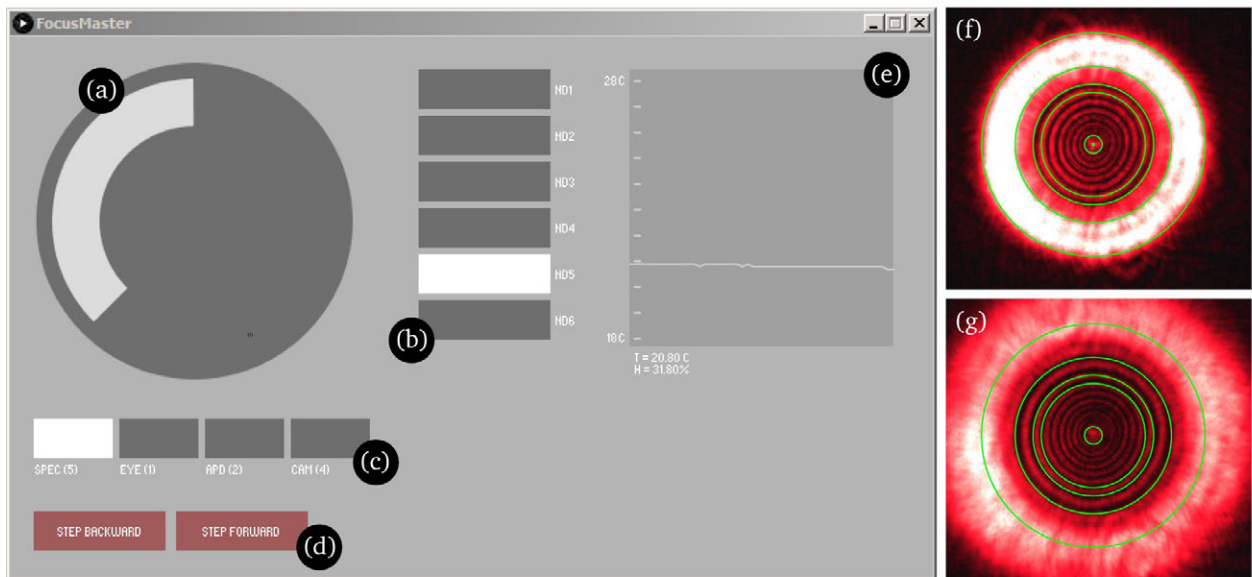
inside the closed curtains, with minimal amount of light, where any oversight is enough to put the experiment to waste. The human presence also imposes a thermal load and humidity rise that should be avoided. It is not uncommon for the user to work with a peer, in the aims of discussing experiment related matters and for decision making, where the mere act of speaking close to the experiment can have adverse effects.

In order to minimize system interference during an experiment and also to improve system usability, we implemented the automation of the following elements: filter wheel (Figure C.2(d)), microscope optical path selector knob (Figure C.2(e)) and microscope focus wheel (Figure C.2(g)). Three stepper motors (a. k. a. steppers) were used, one at each element. The stepper's shaft were fitted with a 20-tooth pulley (model GT2-2M) to drive a matching timing belt. In each element the timing belt was coupled differently. At the optical path selector knob, a piece of timing bell with the same size as the circumference of the dial was cut and glued to it[4], with the teeth facing outwards. The same principle was applied to couple the filter wheel to the another stepper. The focus wheel of the Nikon inverted microscope has two focus knobs, an internal one for course focusing and an external one for fine focusing. Here we tried to couple the stepper to the fine focusing knob, however due to its beveled design, the timing belt would slip out. In order to solve that, the cover of the fine focusing knob was removed and a coupler was designed to match the screw pattern of the cover and machined in brass at the local metal workshop (Figure C.2(f)). The coupler diameter was chosen to match the center hole of an empty spool, where the timing belt was finally glued (Figure C.2(g)). Another advantage of using this empty spool is the fact that, due to its radius being 4× larger than the 20-tooth pulley coupled to the stepper[5], it works as a reduction system, increasing the the angular precision provided by the stepper. Given that the stepper used has a 1.8° per step travel range, per manufacturer specification, its travel precision was minimized to $\approx 0.45°$ per step, therefore providing a much finer focus adjustment. Control wise, each stepper is connected to a stepper driver circuit board designed around the A3967 integrated circuit. The three stepper driver boards are connected to the same Arduino microcontroller used for temperature and humidity monitoring (Figure C.2(b)).

[4]with a rapid drying acrylate adhesive

[5]The empty spool has an external radius of 40 mm, while the GT2-2M pulley has a working radius of 9.6 mm

C.4   MONITORING AND AUTOMATION SOFTWARE

FIGURE C.3: Screen grab of the graphical user interface of the automation software. (a) Fine focus adjustment dial. (b) Neutral density filter selector. (c) Optical path selector, which provides the user the control over through which port the beam with pass. (d) These controls are provided to move the stepper coupled to the optical path selector knob one single step in either direction, due to the fact that sometimes the microscope mechanism does not lock into place. (e) Graph that rolls from right to left showing, in total, the last 30 minutes of temperature readings. (f) Laser spot as seen from the eyepiece camera when the laser is correctly focused. The green circles are used as fiducial markers indicating where the correct focus should be. (g) Same as (f), however this time the laser is not correctly focused.

In order to interface with the Arduino microcontroller (see Appendix C.3), a software has been developed through which it is possible to control all the stepper motors. Named FocusMaster (Figure C.3), the software was created in Java, using the open-source development environment Processing [216], and features a graphical user interface (GUI) with all the required elements to properly interact with the system.

Figure C.3(a) shows a rotating dial for focus adjustment. By scrolling the mouse wheel or by clicking and dragging on the light-gray arc, the stepper coupled to the focus mechanism rotates accordingly in very fine increments. This automation allows for a more precise focus compared to what could be achieved manually. Another advantage is the fact that, due to the CCD camera attached to the eyepiece of the microscope, the user is able to adjust the focus while looking the image from this camera. Depending on the sample, specially those smaller than the diffraction limit, therefore invisible even in the micrometer scale, a set of concentric circles overlaid on the image acquired from the eyepiece camera, are used as a fiducial marker. By moving the focus up and down through the focus, when the focus pattern matches the fiducial markers, one can be sure that the laser is correctly focused (Figure C.3(f,g)). The fiducial markers are also a safe way to assert that the system alignment is preserved. If for some reason an optical component accidentally changed its position, the user could easily spot the change due to the mismatch between

the fiducial markers and the focus image as seen from the eyepiece camera.

Figure C.3(b) shows six pushbuttons which act on the filter wheel rotating the desired filter position into place. Before this automation, the user had to slide open one of the metal housing doors, use an attenuated light source and manually rotate the filter wheel, making sure that it locked into the correct slot. As a safe measure, the user should also take note of the current filter position, otherwise, if forgotten, the user had to open the door once again to double check. Through the software, by selecting the desired filter position, the stepper motor gently rotates the filter wheel a predefined number of steps necessary to perfectly align the desired filter to the laser path. The software also provides the added advantage that, by simply glancing at the software interface, one is able to see which is the current filter in use.

Figure C.3(c) shows four pushbuttons responsible for acting on the optical path selector knob, used for directing the beam to the desired optical path based on the measuring instrument the user wants to work with (i.e. eyepiece, APD or spectrometer). As with the filter wheel, before the automation, the user had to slide open the door to manually rotate the knob. As with the filter wheel, there is the added advantage of having the current optical path port always visible on the software interface.

The software also provides the current ambient temperature and humidity readings with a 6 s interval between measurements, as well as a dynamic rolling graph that displays the last sixty temperature readings with a 30 s delay between each graphical data point, providing a visual history from the last 30 min (Figure C.3(e)). The temperature and humidity readings, together with the date/time the data was acquired, are also saved to disk, every 6 seconds, in a comma-separated values (CSV) text file format, in case the user whats to analyze the readings from a longer timespan.
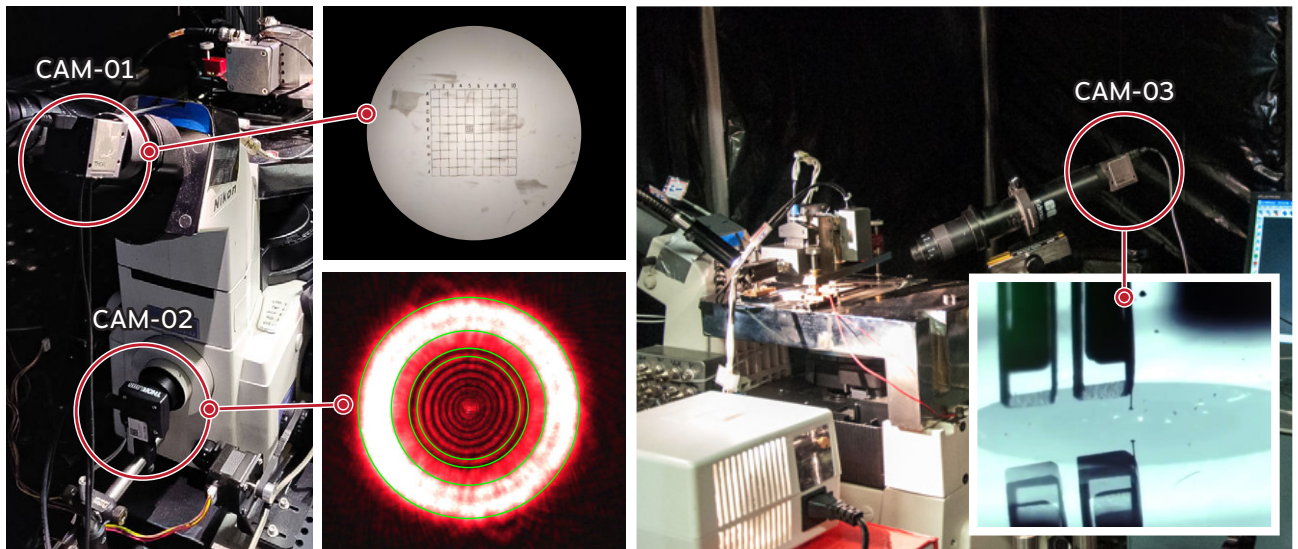
Additional monitoring is done by three CMOS cameras connected to the system, as shown in Figure C.4, one in the eyepiece of the microscope (Figure C.4(CAM-01)), one in the output port opposite to the entrance of the microscope (Figure C.4(CAM-02)) and one attached to the long distance microscope (Figure C.4(CAM-03)), which provides a zoomed in view of the tip in order to facilitate the initial laser/tip alignment.

FIGURE C.4: Location of the three cameras, CAM-01, CAM-02 and CAM-03, used in the TERS system. CAM-01 is locate in the right ocular of the eyepiece, CAM-02 is attached to the output port parallel to the body of the microscope and CAM-03 is attached to a long distance microscope, whose image is used to assist in the tip-approach process.

C.5 AUTOMATION — LIST OF COMPONENTS

Following is a table listing the elements utilized for automation and monitoring.

TABLE C.1

COMPONENTS FOR AUTOMATION & MONITORING

| ITEM	ITEM #/CODE	MAKER
Arduino	Nano	Arduino
Temperature & humidity sensor	DHT22	Aosong Electronics
Stepper motor driver	EasyDriver V44 A3967	Sparkfun
Stepper motor, NEMA-17, 1.8°/200 steps, 12VDC	SM1-8-A1734C	Action Technology
LIST OF FASTENING ELEMENTS		
L-shaped mounting bracket for NEMA17	-	Various vendors
20-tooth pulley	GT2-2M compatible	Various vendors
Timing Belt	GT2-2M compatible	Various vendors
Ø1.25" Studded Pedestal Base Adapter	BE1	Thorlabs
Ø1/2" Post Holder	PH2	Thorlabs
Ø1/2" Optical Post	TR2	Thorlabs
Clamping Fork, 1.24" Counterbored Slot	CF125C	Thorlabs

D

STM Tip Assembly
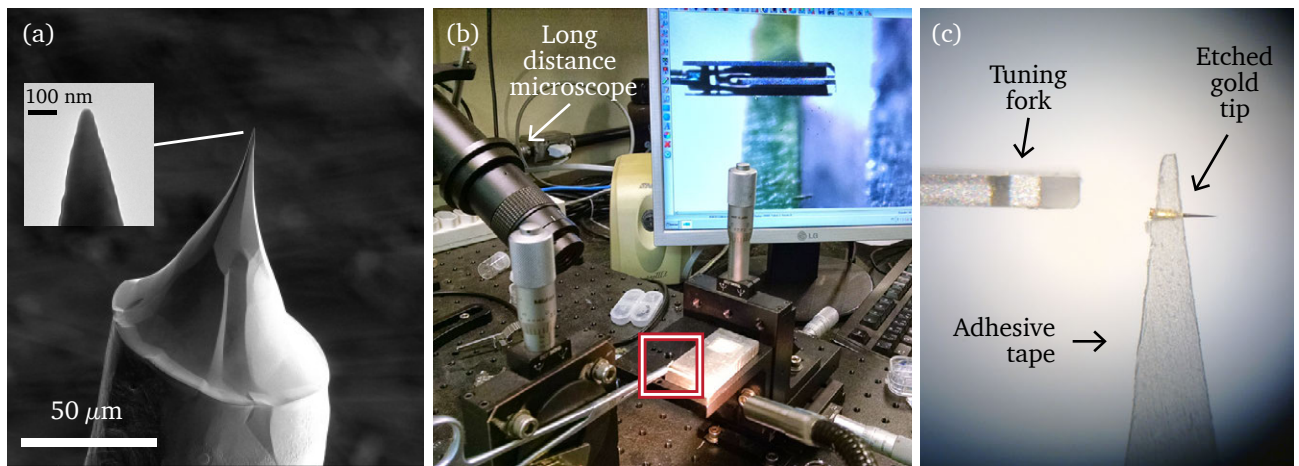
FIGURE D.1: (a) Etched gold wire as seen through a scanning electron microscope (adapted from [39]). (b) Photograph of the setup used to assemble the etched tips to the tuning forks, with the long distance microscope, micromanipulators and in the red highlight a tuning fork held by a tweezer and ready to receive the etched gold tip. The computer monitor is displaying the tuning fork as seen from the long distance microscope. (c) Photograph showing an etched gold tip attached to an adhesive tape as seen from one of the eyepieces of a stereoscope. A prong of the tuning fork is visible on the left of the image (picture provided by Prof. Alexandre Paschoal).

The STM tips were produced by the lamella-dropoff electrochemical etching method [217] from 100 μm thick gold wire with 99.995 % purity. After etching the gold wire, the tip is taken to a scanning electron microscope for inspection in order to determine the apex diameter (Figure D.1(a)). If it is >50 nm it is usually discarded. In order to glue the etched gold wire containing the tip at one end, we attach it to a piece of scotch tape and we manually cut it down to ≈ 2 mm using a scalpel. With the help of micromanipulators and a stereoscope (Figure D.1(b,c)), a small droplet of cyanoacrylate adhesive (i. e. *5-second bond* or *Super Glue*) is carefully spread onto a small region on one of the tuning fork's prong and the tip, still glued to the tape, is lowered through the use of the micromanipulators until it gently touches the glue. After a few minutes the glue is completely dry and the tape can be manually removed with ease. Once the gold tip is cemented in place, we use silver paint[1] to create an electrical

[1] SPI Flash-Dry Silver Colloidal Suspension. Item #: 04998-AB

connection between the nanoantenna and the tuning fork electrode. The silver paint can be applied with the help of small needle taken from a syringe or with any other sharp object. With the STM probe fully assembled, the tunning fork is soldered to the circuit board of the AFM's 1st amplification stage. It is important to note that for the STM the circuit board is left completely blank of electronic components, serving only as a mean to hold the tuning fork in place and to make the necessary electrical connection from the tip to the STM's current preamplifier (see Section 3.2.1).

[1] Edward R Tufte. *Beautiful evidence*. Vol. 1. Graphics Press Cheshire, CT, 2006

[2] https://ctan.org/pkg/memoir

[3] https://github.com/pfasante/phd_thesis